Analysis of the three-dimensional flow field in the carotid artery bifurcation

DOI:
10.6100/IR307997

Document status and date:
Published: 01/01/1989

Document Version:
Publisher's PDF, also known as Version of Record (includes final page, issue and volume numbers)

ANALYSIS
OF THE THREE–DIMENSIONAL FLOW FIELD
IN THE CAROTID ARTERY BIFURCATION

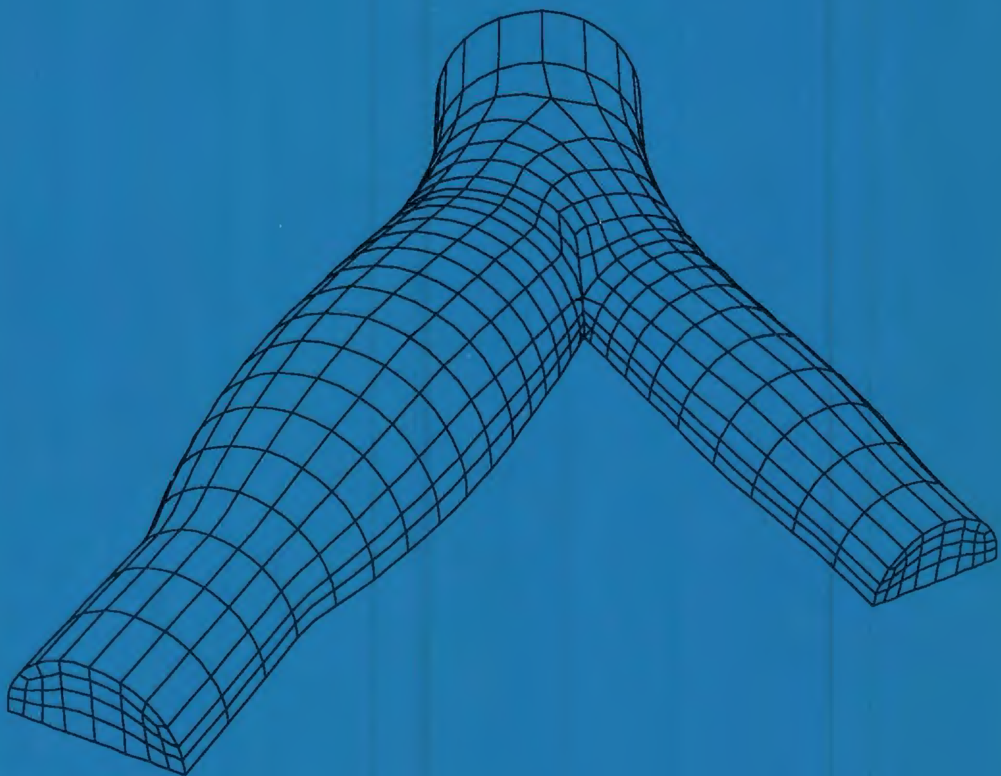

Camilo Rindt

CIP–GEGEVENS KONINKLIJKE BIBLIOTHEEK, DEN HAAG

Rindt, Camilo Christiaan Maria

Analysis of the three–dimensional flow field in the
carotid artery bifurcation / Camilo Christiaan Maria
Rindt. – [S.l. : s.n.]. – Ill.
Proefschrift Eindhoven. – Met lit. opg. – Met samenvatting
in het Nederlands
ISBN 90–9002836–6
SISO 605.12 UDC 612.1(043.3)
Trefw.: eindige elementen methode ; bloedstroming ;
halsslagadervertakking

Druk: Febodruk, Enschede

ANALYSIS
OF THE THREE-DIMENSIONAL FLOW FIELD
IN THE CAROTID ARTERY BIFURCATION

PROEFSCHRIFT

ter verkrijging van de graad van doctor
aan de Technische Universiteit Eindhoven,
op gezag van de rector magnificus, prof.ir. M. Tels,
voor een commissie aangewezen door het college van decanen
in het openbaar te verdedigen
op vrijdag 26 mei 1989 om 16.00 uur

door

CAMILO CHRISTIAAN MARIA RINDT

geboren te

Zevenbergschen-Hoek

Dit proefschrift is goedgekeurd door de promotoren

Prof.dr.ir. J.D. Janssen
Prof.dr. R.S. Reneman

Co–promotor

Dr.ir. A.A. van Steenhoven

Het verschijnen van dit proefschrift werd mede mogelijk gemaakt door de steun van de Nederlandse Hartstichting.

Financial support by the Netherlands Heart Foundation for publication of this thesis is gratefully acknowledged.

Voor Yollie

Contents

Summary

In the development of non–invasive detection methods of atherosclerotic lesions in the carotid artery bifurcation at an early stage of the disease, insight into the complicated flow field in this bifurcation is indispensable. Beside experimental research, also numerical simulations contribute to a better understanding of the flow phenomena occurring in the carotid artery bifurcation.

For a description of the geometry of the carotid artery bifurcation, data available in literature is used. Besides, a cast study is performed using 7 postmortem specimen. From this study it is concluded that large inter–individual variabilities occur in the geometry of the carotid artery bifurcation. Therefore, studies dealing with the influence of geometry variations on the total flow field are indispensable. For discretization of the governing fluid equations Galerkin's finite element method is used, in which blood is presumed to behave like an incompressible and Newtonian fluid and the vessel walls are supposed to be rigid. Because three–dimensional analysis results in large systems of equations, super and minisupercomputers are used, which can be 10 to 1000 times as fast as conventional systems. To decrease the computing times needed even more, a special purpose mesh generator is developed, enabling division of the carotid artery bifurcation into a relatively small number of elements, and a special renumbering procedure is employed. Non–contact laser Doppler velocity measurements are performed in rigid–walled three–dimensional models for experimental validation of the numerical results.

Because curvature effects highly influence the flow phenomena occurring in symmetrical bifurcations and due to its rather simple geometry, steady and unsteady flow in a 90–degree curved tube are analyzed under physiological flow conditions. From this study it appears that axial flow is highly determined by secondary flow, which on its turn is induced by centrifugal forces. Besides, the influence of the frequency parameter, the flow wave form and the steady flow component on axial and secondary flow is investigated.

From a detailed analysis of steady flow in the carotid artery bifurcation it is concluded that curvature effects indeed play an important role in the daughter branches of this bifurcation. However, also the proximal widening and distal tapering of the carotid sinus, highly affect axial and secondary flow. From a parameter study on the influence of the Reynolds number, the flow division ratio and the bifurcation angle, it is observed that this influence on the flow phenomena

occurring is relatively small.

From the present study it is concluded that the finite element method in combination with supercomputers can be used for detailed analysis of fluid flow in complex three–dimensional geometries. Incorporation of non–Newtonian behavior of blood and flexibility of the arterial wall in the numerical model will complete such an analysis.

Symbols

a	radius of a tube
A	surface of a region with boundary S
C	center of a tube
C	common carotid artery
D	divider wall
E	external carotid artery
I	inner wall
I	internal carotid artery
L	characteristic length
O	outer wall
R	curvature radius of a tube
Re	Reynolds number (UL/ν)
R_s	Reynolds number of secondary flow $(\delta U^2/(\nu\omega))$
S	side wall
S	boundary of a region with surface A
Sr	Strouhal number $(\omega L/U)$
t	time
T	period time
U	characteristic velocity
u_{ax}	axial velocity
U_{max}	maximum of axial velocity
U_{mn}	time–averaged mean axial velocity
u_{tg}	tangential velocity
$\langle X/a \rangle$	first moment of axial flow
α	Womersley parameter $(a(\omega/\nu)^{1/2})$
δ	curvature ratio (a/R)
κ	Dean number $(Re\delta^{1/2})$
ν	kinematic viscosity
ω	characteristic angular frequency
θ	position angle of a cross–sectional plane
ξ_c	axial vorticity of the central core
ξ_m	maximum of axial vorticity
ξ_s	axial vorticity at r=4/5a

1 Introduction

1.1 Atherosclerotic disease of the carotid artery bifurcation

Atherosclerosis is a complicated process associated with such processes as intimal thickening, accumulation of lipids and calcium in the extracellular matrix, and smooth muscle cell proliferation. These changes often lead to intraluminal processes narrowing the diseased artery and eventually leading to total occlusion of the vessel. At an early stage of the disease atherosclerotic plaque formation may induce thrombus formation, i.e. fragments of the thrombus break off and obstruct smaller arteries downstream.

A variety of theories has been proposed regarding the cause of atherosclerosis. In some of these theories hemodynamic factors play an important role. A possible role of hemodynamics in the process of atherosclerosis is suggested by its predilection to bends and bifurcations, since flow phenomena exhibit unique characteristics in these areas. For many years it was thought that endothelial injury caused by high shear stresses was responsible for atherogenesis (Fry, 1969; Lutz et al., 1977). However, more recent studies confirm Caro's observations (Caro et al., 1971) that atherosclerotic lesions develop more frequent in regions with low shear stresses and with recirculation than in regions with high shear stresses and unidirectional flow (Zarins et al., 1983; Ku et al., 1985). Therefore, detailed insight into the flow phenomena occurring in bends and bifurcations possibly contributes to a better understanding of the role of hemodynamics in the process of atherosclerosis.

For years in the clinic atherosclerotic disease has been diagnosed with the use of contrast angiography, an invasive approach. Because this method has a low but definite risk, it cannot be used for screening of asymptomatic patients (Mani and Eisenberg, 1978; Spencer and Reid, 1979) or to follow–up patients, for example, during medical treatment or after surgery. Therefore, more recently non–invasive detection methods have been developed. Generally, these methods are based upon the detection of flow disturbances, as induced by these lesions, using continuous wave or pulsed Doppler (van Merode et al., 1988). However, due to the complicated flow fields in bends and bifurcations, the preferential sites of atherosclerosis, it is often difficult to distinguish these flow disturbances from the flow phenomena normally occurring at these sites (Reneman et al., 1985). More detailed insight into these complicated flow fields and the influence of geometrical variations and low grade lesions on the flow patterns, is important in the development of methods to diagnose atherosclerotic lesions at an early stage of the disease.

A bifurcation often affected by atherosclerotic plaque formation is the carotid artery bifurcation. Atherosclerosis in this region is the major cause of transient ischemic attacks. Such attacks may result from a reduction in the blood flow due to narrowing of the arterial lumen, but are generally caused by emboli originating from ulcerating or high grade lesions. Bharadvaj et al. (1982) performed an experimental study on steady flow in the carotid artery bifurcation and found complex axial and secondary flow patterns. Olson (1971) concluded that the flow phenomena occurring in the daughter branches of a symmetrical bifurcation mainly originate from curvature effects. Therefore, insight into the flow phenomena occurring in curved tubes may contribute to a better understanding of the complex flow field in the carotid artery bifurcation. In this study a detailed numerical analysis is performed of steady and unsteady flow in a 90–degree curved tube and of steady flow in a three–dimensional model of the carotid artery bifurcation.

1.2 Model simplifications

The geometry of the carotid artery bifurcation is very complicated. Besides, its geometry is hard to define due to its predilection for atherosclerotic lesions, resulting in filling in of certain segments of the bifurcation at older age. The geometry used in the present study is based upon data of Balasubramanian (1979), who determined a standard geometry from over 100 angiograms (Balasubramanian later changed his name into Bharadvaj). To reduce the complexity of the in vivo situation, he modeled the main branch and both daughter branches as straight tubes with circular cross–sections and all branches were supposed to lie in one plane. All diameter values were averaged in a straight forward manner, except the dimensions of the carotid sinus for which only selective data were used. To evaluate the relevance of the simplifications performed by Balasubramanian (1979) and to validate his results for the bifurcation angle, the diameter of the main branch and the geometry of the carotid sinus, a cast study was carried out on the geometry of 7 postmortem specimen.

In vivo flow rate measurements reveal that the Reynolds number and the flow division ratio over the daughter branches of the carotid artery bifurcation vary considerably during a flow cycle. The flow rate at peak systole can be 3 to 4 times larger than the flow rate in the diastolic phase. According to Ku et al. (1985) a Reynolds number of 800 at peak systole and a mean Reynolds number of 300 are typical conditions for a normal adult human carotid. The flow division ratio can vary between 55/45 (55% through the internal carotid artery) at peak flow rate and 75/25 at minimal flow rate. In the present study only steady flow is dealt with. However, to gain some insight into the influence of these varying conditions during a flow cycle on the flow phenomena occurring, velocity calculations are performed at various Reynolds numbers and flow division ratios.

At high shear rates blood is assumed to behave like a homogeneous Newtonian fluid. However, blood consists of red blood cells, white blood cells, platelets, proteins and chylomicrons suspended in a fluid called plasma. As a consequence, non–Newtonian behavior may be expected due to aligning of the blood cells in the flow direction at high shear rates and rouleaux formation at low shear rates. Liepsch and Moravec (1984) studied the difference in flow behavior of Newtonian and non–Newtonian fluids and observed larger velocity gradients in case Newtonian fluids were used. In the present study only pure Newtonian fluids are considered which might be debatable, especially in flow regions with low shear rates. However, at this moment numerical modeling of unsteady non–Newtonian fluid flow is very difficult to achieve.

Liepsch and Moravec (1984) also studied the influence of flexible walls on the flow phenomena occurring. At high wall flexibility no reversed axial flow was observed. In spite of the fact that the wall of the carotid artery bifurcation has to be regarded as (visco–) elastic, this effect will be neglected in the present study because, due to the occurring wave phenomena, velocity measurements and velocity calculations in distensible models are still very difficult to perform.

It is well understood that the above simplifications may lead to flow patterns differing from those in the <u>in vivo</u> situation. However, a study performed by Ku et al. (1985) revealed a good agreement between <u>in vivo</u> and <u>in vitro</u> velocity data of blood flow in the normal human carotid bifurcation. Therefore, it is believed that the results from this study supply more insight into the complicated flow field occurring in the carotid artery bifurcation. Besides, incorporation of flexible walls and non–Newtonian behavior of blood flow in the numerical model is only meaningful if the numerical results from a simplificated analysis are validated with experimental results.

<u>1.3 Methods used</u>

In the Atherosclerosis–project at the Eindhoven University of Technology, flow patterns occurring in 2D– and 3D–models are studied using finite element and laser Doppler techniques. In an experimental and numerical study by van de Vosse et al. (1985) steady and pulsating flow over a two–dimensional step was analyzed. Rindt et al. (1987) and van de Vosse (1987) performed steady and unsteady velocity measurements and calculations of flow in a two–dimensional model of the carotid artery bifurcation. Three–dimensional calculations were performed by van de Vosse et al. (1989), who studied steady entrance flow in a 90–degree curved tube. These results were also validated with experimental data. A study by van de Vosse et al. (1987) and Rindt et al. (1988) indicated that three–dimensional analysis of the flow field in the carotid artery bifurcation is necessary to better understand the <u>in vivo</u> flow situation. Especially in the region with reversed axial flow, large differences were observed between the axial velocities in a 2D–model and those in the plane of symmetry of a 3D–model. These differences are mainly caused by secondary flow, which is absent in the two–dimensional situation. Also axial velocity plateaus downstream in the carotid sinus near the non–divider wall, as found in the experiments of Bharadvaj et al. (1982) and Rindt et al. (1988), are absent in a 2D–model. Therefore, in the present study a finite element approximation of steady flow in a rigid 3D–model of the carotid artery bifurcation is presented. The numerical results are compared with those obtained from laser Doppler velocity measurements. For better understanding of the secondary flow patterns and due to its geometrical simplicity, first fluid flow in a 90–degree bend is studied.

For the construction of an approximate solution several numerical methods are available, of which the finite difference method (Roache, 1972; Peyret and Taylor, 1982) and the finite element method (Girault and Raviart, 1979; Cuvelier et al., 1986; van de Vosse et al., 1986) are the most important ones. An advantage of the finite element method over the finite difference method is its flexibility with regard to mesh refinement and geometry description. Therefore, application of the finite element method to flow problems in complex 3D–geometries with high velocity gradients is assumed to be more appropriate for the space discretization than the finite difference method. Due to the large system of equations resulting from a three–dimensional analysis, special attention has to be paid to the problem of solving large systems of equations efficiently.

To validate the numerical results accurate measurements of both axial and secondary flow are required. To achieve this goal, non–contact measuring techniques are preferred over contact measuring techniques, like hot–wire anemometry. For <u>in vivo</u> measurements of blood flow velocities multi–gate pulsed

Doppler systems can be used (Reneman et al., 1985 and 1986). In this method traversing of the measuring volume occurs electronically. A disadvantage of this method is its limited resolution because of the relatively large measuring volume. A measuring technique which does not have this disadvantage is laser Doppler anemometry (Drain, 1981). Detailed information of the flow field can be achieved due to the small measuring volume, which can be 1000 times smaller as for pulsed Doppler systems. In this method, however, accurate positioning techniques are required for traversing of the measuring volume (Corver et al., 1985; Bovendeerd et al., 1987).

1.4 Outline of the study

In chapter 2 a survey is given of the data reported in literature concerning the geometry of the carotid artery bifurcation. Also the results of a cast study performed on the geometry of 7 postmortem specimen are presented, and the results of this study are compared with the dimensions obtained by other investigators.

In chapter 3 a short description is given of the numerical method employed for the analysis of the fluid flow problems presented in this study. Galerkin's finite element method is used for the spatial discretization of the momentum and continuity equations. After substitution of the constitutive relation for Newtonian fluids this results in a non–linear set of equations, which is linearized by a Newton–Raphson iteration scheme. Application of the penalty function approach results in a set of equations with only unknowns for the velocity. For the temporal discretization of the local time derivative in the momentum equation, a finite difference time integration scheme is used. For division of the carotid artery bifurcation into 3D–elements, a special purpose mesh generator was developed. Also a short description is given of the finite element package used. Finally, at the end of this chapter, some test calculations are presented.

As mentioned before, Olson (1971) concluded that the flow phenomena occurring in the daughter branches of a symmetrical bifurcation mainly originate from curvature effects. In chapter 4 the experimental method, which was used for the steady and unsteady velocity measurements in a 90–degree curved tube and for the steady flow experiments in a 3D–model of the carotid artery bifurcation, is described. The laser Doppler measuring technique, the experimental set–up and the measuring fluids used are briefly described. Also, the error sources are dealt with and error estimates are given for the axial and secondary velocity components.

Chapter 5 is dealing with the results of velocity measurements and calculations in the case of steady and unsteady flow through a 90–degree curved tube. First, the numerical results for steady flow at a physiological Reynolds number are shown and compared with the experimental results of Bovendeerd et al. (1987). Next, the same comparison between experimental and numerical results is made for a sinusoidally varying flow rate. Finally, the influences of the frequency parameter, the steady flow component and the wave form on the axial and secondary velocity fields are described.

In chapter 6 steady flow in a 3D–model of the carotid artery bifurcation is discussed. The results of a finite element calculation are validated with data obtained from laser Doppler velocity measurements, carried out at a physiological Reynolds number and flow division ratio. Also the influences of a varying Reynolds number and flow division ratio and of a smaller bifurcation angle on the axial and secondary velocity fields are presented.

Finally, in chapter 7 some conclusions are given and topics for later research are discussed.

2 Geometry of the carotid artery bifurcation

2.1 Introduction

Several investigators have studied the geometry of the carotid artery bifurcation, but normal data of healthy subjects are difficult to obtain because this bifurcation is the site of preference of atherosclerotic lesions. The most detailed study has been carried out by Balasubramanian (1979), who determined angiographically a mean geometry of the carotid artery bifurcation. Because of some disagreements between his data and those obtained by other investigators, using the same or different techniques, a cast study on the geometry of this bifurcation was performed. In section 2.2 a survey is given of the results reported in literature, and a comparison is made between the data obtained by Balasubramanian (1979) and other investigators. In section 2.3 the results of the cast study are presented and compared with the data available in literature.

2.2 Survey of the literature

The carotid artery bifurcation consists of a main branch, the common carotid artery, which asymmetrically divides into two daughter branches, the internal and external carotid artery. The internal carotid artery is characterized by a widening in its most proximal part, the carotid sinus or bulb. Normally, the common carotid artery is almost straight and has a constant diameter over its total length of about 10 cm. In most cases the common carotid artery has no bifurcating branches. The left common carotid artery branches off directly from the aortic arch, whereas the right one originates from the anonymous artery, also a side branch of the aortic arch. Most of the internal carotid arteries are almost straight, some of them are slightly curved and a few show highly curved segments 2–8 cm after their origin. The external carotid artery has many bifurcating branches the first one of which, the superior thyroid artery, originates after 0.5–2 cm. The internal carotid artery supplies the brains with blood and the external carotid artery the extracranial facial structures.

In literature several techniques have been presented to measure characteristic dimensions of the carotid artery bifurcation. Arndt et al. (1968) and Olson (1974) used pulsed echo techniques to measure diastolic and systolic diameters of the common carotid artery. Keller et al. (1976) used a multi–gate pulsed Doppler system to determine the diameter of the main branch, whereas Reneman et al. (1985) used this technique to measure the geometry of the bulb and the relative diameter changes of the arteries during the cardiac cycle in young and old presumed healthy subjects. In the latter study also the angle between the internal and common carotid artery was measured with the use of a B–mode imager. Zbornikova and Lassvik (1986) used an ultrasonic duplex scanning technique to measure the diameter of the common carotid artery, the internal carotid artery distal to the bulb and the external carotid artery as a function of age. A second commonly used method makes use of angiograms. Balasubramanian (1979) studied in this way 57 angio's and his results will later be discussed in more detail. Brown and Johnston (1982) analyzed angiograms of 28 presumed healthy carotid artery bifurcations to determine the anteroposterior and lateral diameters of the common and the internal carotid artery. Harrison and Marshall (1983) used this technique to determine the bifurcation angle between the internal and common carotid artery and between the external and common carotid artery. Greenfield et al. (1964) measured diastolic and systolic diameters with a calibrated clamp during surgery. Of the 13 patients 11 received general anesthesia whereas 2 patients were only locally anesthetized.

In vitro techniques have also been used to determine the geometry of the carotid artery bifurcation. For example, Peterson et al. (1960) excised 123 bifurcations and, before the tissues hardened, the lumen contours were assessed by filling the segment with warm paraffin. They measured the cross–sectional area of the lumen proximal in the internal and external carotid arteries and just before the bifurcation. The bifurcation angle was also determined. In a study by Zarins et al. (1983) and Motomiya and Karino (1984) the tissues were fixed soon after removal from the body. From these postmortem specimen the diameter and the bifurcation angle were detected.

The above studies indicate that a variety of techniques has been used to study the geometry of the carotid artery bifurcation. However, the results of these studies must be interpreted with care. From the study of Arndt et al. (1968) it is not clear whether internal or external diameters were measured. Greenfield et al. (1964) measured external diameters. In other studies the measuring positions are not always exactly given and definitions of bifurcation angles are sometimes vague or totally missing. Besides, Altura and Altura (1975) showed that the properties of the tissue change under influence of anesthetics which might affect the geometry of the artery. Gow and Hadfield (1979) studied the elasticity of pre– and postmortem specimen and observed that the diameter of the femoral artery of dogs increased with 10% after removal from the body. These findings indicate that one in principal has to rely on in vivo measurements. However, the information obtained under these circumstances is limited and more detailed information is required for adequate description of the geometry of the carotid artery bifurcation. Therefore, in vitro measurements cannot be avoided.

In table 2.1 the results are summarized. If the dimensions reported in literature are given as a function of age, the results presented refer to subjects with an age of about 50 years because most of the data available in literature is derived from subjects in this age category. If diastolic and systolic diameters are given, the diastolic diameters are presented. The positions indicated in the table do not always coincide with the real measuring positions but the differences are presumed to be small. The dimensions are relative to the diameter of the common carotid artery with the exception of this diameter itself which is given in mm. The symbols C, I and E refer to common, internal and external carotid artery, respectively. The figures refer to the distances of the levels to the flow divider and are given in diameters of the main branch. The bifurcation angle is presented by AIE and the angle between the common carotid artery and both daughter branches by AI and AE, respectively. Also the number of subjects N and the mean age of the subjects, if reported, are presented.

	C	I0	I0.5	I1	I1.5	I2	I3	I4	E0	E1	E2	AI	AE	AIE	N	Age
Reneman et al.	6.4	1.08			1.11			0.97				12.6			9	54
Zbornikova et al.	7.5				0.76					0.63					92	49
Brown et al.	6.7		1.07					0.64							28	
Harrison et al.	7.6							0.67				23.0		36.4	102	
Peterson et al.	5.8			0.78						0.62				39.0	42	50
Zarins et al.	6.1	0.98		1.02				0.57			0.66			46.0	12	
Motomiya et al.	5.9		0.88						0.64					30.0	1	
Arndt et al.	7.6														9	28
Olson	7.6														2	
Keller et al.	5.9														1	
Greenfield et al.	8.6														13	47
Balasubramanian	8.0	1.04		1.11		0.72		0.69	0.69	0.69	0.58	25.3	25.1			
conf.int.		0.21		0.14		0.12		0.10	0.17	0.13	0.10	10.4	11.0			

Table 2.1: Dimensions of the carotid artery bifurcation. The dimensions are relative to the diameter of the common carotid artery with the exception of this diameter itself which is given in mm.

As mentioned before, the most detailed study of the geometry of the carotid artery bifurcation was carried out by Balasubramanian (1979). He determined angiographically a mean geometry of the carotid artery bifurcation. To reduce the complexity of the in vivo situation he modeled the main branch and both daughter branches as straight tubes with circular cross–sections which are all positioned in one plane. Balasubramanian studied 57 angio's of 22 adults between the age of 34 and 77. Some of the carotid artery bifurcations were already affected by atherosclerotic lesions. The angio's were divided into one group with and one group without a clearly visible bulb, a definition of which is missing. Because Balasubramanian was interested in the geometry of the carotid artery bifurcation of young healthy adults and because it appeared from the same study that 92% of the children between the age of 11 and 18 years had a clearly visible bulb, for determination of the geometry of the carotid sinus only the angio's of the adults were used with such a clearly visible bulb. For all other dimensions the entire series of angiograms was used. According to Balasubramanian it was difficult to locate an exact centerline of each vessel because of curvatures of the arteries. These centerlines, however, are needed for the determination of the angles between the main branch and the daughter branches. Besides, for correct determination of these angles two angiograms are needed, of which the X–ray directions are perpendicular to each other. In practice this can be very difficult to achieve. Because of scaling problems all the dimensions are given relative to the diameter of the common carotid artery. This diameter was estimated on the basis of data derived from literature (Greenfield et al., 1964; Angell–James and Lumley, 1974; Arndt et al., 1968; Olson, 1974). In table 2.1 his results are summarized at positions close to the real measuring positions. The number of samples varied between 11 and 53 and the age of the subjects between 34 and 77 years. Also the confidence intervals of the data obtained by Balasubramanian are given.

The diameter of the common carotid artery was estimated to be 8 mm by Balasubramanian. From the other studies, however, it is concluded that this diameter is probably smaller. Only Greenfield et al. (1964) measured a diameter larger than 8 mm, but in their study external diameters were obtained, Balasubramanian's determination of the geometry of the carotid sinus is debatable because it excludes the possibility of an underdeveloped bulb for young adults. The geometry of the bulb found by Balasubramanian has a maximal diameter at about one diameter downstream of the flow divider, which is about 7% larger than the diameter at the entrance of the bulb. Reneman et al. (1985) and Zarins et al. (1983) also found the largest diameter downstream in the internal carotid artery, but the differences with the entrance diameter were smaller in their studies on subjects over 50 years of age. Similar results were obtained by Reneman et al. (1985) in 11 subjects with an age between 20 and 30 years. A bifurcation angle of the daughter branches of 50°, as found by Balasubramanian, is somewhat large. Both Harrison and Marshall (1983) and Peterson et al. (1960) found a mean bifurcation angle which was smaller than 40°. Also the angle of the internal carotid artery with the common carotid artery, as found by Reneman et al. (1985), is smaller as the one found by Balasubramanian. From the confidence intervals mentioned in literature it appears that, especially for the angles and the dimensions of the carotid sinus, large inter–individual variabilities occur. In this light, it is debatable to present a mean geometry of the carotid artery bifurcation because then individual characteristics of this geometry are possibly averaged out.

2.3 Cast study

To obtain insight into the inter–individual variabilities in the geometry of the carotid artery bifurcation and to evaluate the simplifications assumed by Balasubramanian, a cast study was performed. At the University of Limburg (Department of anatomy; Arno Lataster), 7 casts of the carotid artery bifurcation were prepared of subjects varying in age from 37 to 71 years. None of them died as a consequence of atherosclerotic disease of the carotid artery bifurcation. For preparation of the casts the cerebral vascular system was rinsed with a physiological salt solution and filled with Technovit. After termination of the hardening process both carotid artery bifurcations were removed from the body and the connective tissue was stripped off. In figure 2.2 two of these bifurcations are presented. For both bifurcations the internal carotid artery is presented by the upper daughter branch. Due to problems with the casting process the daughter branches of the left bifurcation are somewhat short. From the bifurcation at the right panel it is observed that the external carotid artery has many bifurcating branches soon after its origin, whereas the internal carotid artery shows no bifurcating branches and has a curved geometry. The bulb diameter relative to the diameter of the main branch and the bifurcation angle of the bifurcation shown left are much larger than those of the bifurcation shown right. In this particular case the internal carotid artery at the right panel has almost a constant diameter.

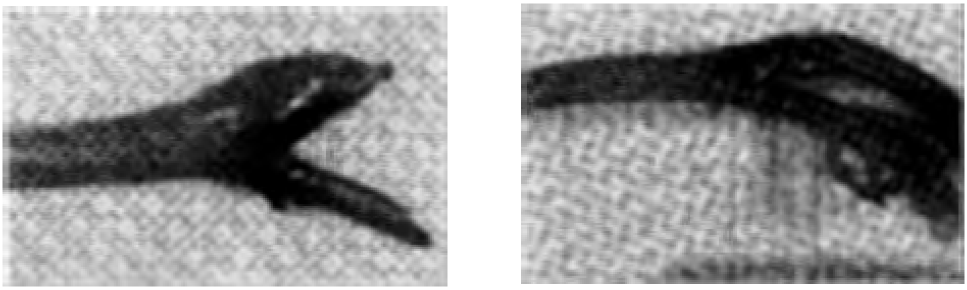

Figure 2.2: Two casts of the carotid artery bifurcation.

The mean diameter of the main branch of all casts was determined by averaging its diameter at three positions in two perpendicular directions, the latter to exclude the influence of elliptical shaped cross–sections. This diameter was used as the dimension to which all distances and diameters are related. Then, the axis of each branch was determined as pointed out in figure 2.3. The entrances of both daughter branches were fixed by points 1 and 2, defined as the points at the apex

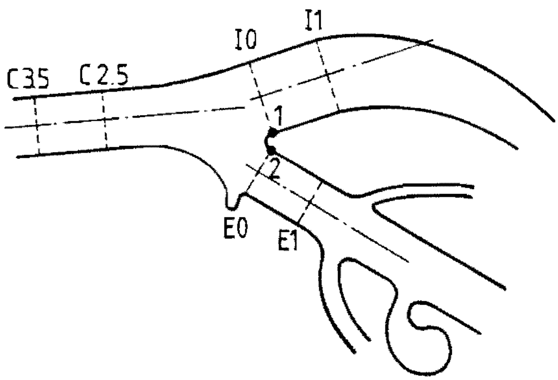

Figure 2.3: Schematical presentation of a cast of the carotid artery bifurcation.

where the divider wall is almost parallel to the axes of the side branches, and the cross–sections C3.5, C2.5, I0, I1, E0 and E1 were determined. The axes of the arteries were defined as the lines through the midpoints of these cross–sections. The diameter of the internal carotid artery was measured at 7 positions (I0, I0.5, I1, I1.5, I2, I3, I4) and of the external carotid artery at 3 positions (E0, E1, E2). Also the angles of the daughter branches with the main branch were determined. Due to problems with the casting procedure or suspected deposition of atherosclerotic lesions, 1 internal carotid artery and 2 external carotid arteries could not be used for determination of their geometry.

In table 2.4 the results as obtained by these measurements, together with the 95%–confidence intervals for the mean dimensions based on a student–t distribution, are shown. The main differences between the data obtained by Balasubramanian (1979) and those from the casts are observed in the angles between the main branch and both daughter branches, which are essentially smaller for the casts. The angle between the internal and common carotid artery found in the present study is in good agreement with the angle obtained by Reneman et al. (1985). The large confidence intervals for the angles point to large inter–individual variabilities. A reason for the differences between the angles obtained by Balasubramanian and those from the casts is that Balasubramanian's definition of these angles possibly deviates from the definition used in the present study. Besides, localization of the axis of a vessel may be very difficult from a pair of angio's. Also the small population, changes in the geometry during the casting process and the large variation in age of the subjects used in the present study and the study of Balasubramanian, may contribute to these discrepancies.

	C	I0	I0.5	I1	I1.5	I2	I3	I4	E0	E1	E2	AI	AE	AIE
cast 1	6.60	1.12	1.05	0.81	0.70	0.75	0.67	0.66				17		
cast 2	6.10													
cast 3	4.55	0.88	0.92	0.92	0.94	0.88	0.77	0.77	0.73	0.73	0.71	0	16	16
cast 4	4.95	1.20	1.13	1.09	0.98	0.80	0.75	0.70	0.55	0.61	0.61	2	13	15
cast 5	4.80	1.25	1.25	1.25	1.21	1.11	0.74	0.57	0.68	0.53		17	7.5	24.5
cast 6	5.85	1.48	1.28	1.00					0.69	0.59		20	25	45
cast 7	4.95	0.84	0.92	0.94	0.88	0.80	0.74	0.74	0.80	0.70	0.66	7	12	19
mean	5.40	1.13	1.09	1.00	0.94	0.87	0.73	0.69	0.69	0.63	0.66	10.5	14.7	23.9
conf.int.	0.62	0.21	0.13	0.13	0.18	0.14	0.04	0.08	0.09	0.08	0.12	7.4	6.4	12.2

Table 2.4: Dimensions of the carotid artery bifurcation obtained from the casts. The dimensions are relative to the diameter of the common carotid artery with the exception of this diameter itself which is given in mm.

Another remarkable difference is the absence of a clearly visible bulb in the casts. For the casts the largest diameter is found at the entrance of the internal carotid artery, whereas in the study of Balasubramanian the largest diameter was found at about one diameter from the entrance. As mentioned before, Balasubramanian only used angio's with a clearly visible bulb to determine the geometry of it and, therefore, excludes the possibility of the existence of an underdeveloped carotid sinus. Another possible reason for this difference is the age of some of the specimen used in the cast study. In the older ones intimal thickening may have been present. The large confidence intervals for the dimensions in the bulb region are possibly caused by this effect.

A mean diameter of the common carotid artery of 5.4 mm, as found in the cast study, is smaller than the diameter obtained by Balasubramanian (1979), but in rather good agreement with the dimensions found by other investigators. Determination of this diameter in two perpendicular directions contributes to the rather small value because of the elliptical shaped cross–sections. The mean diameter of the common carotid artery in the bifurcation plane was found to be 5.7 mm, whereas this diameter in the other direction was found to be 5.1 mm. Shrinking of the specimen during casting is not likely, because casting either does not affect the diameter or slightly increases it. Therefore, it may be concluded that the diameter of the common carotid artery is probably smaller than presumed by Balasubramanian.

Balasubramanian modeled the main branch and both daughter branches as straight tubes with circular cross–sections which are all positioned in one plane. From the casts it was observed that most of the arteries were more or less curved. In some cases modeling of the arteries as straight tubes may be debatable. For the small population used in the present study, it was indeed observed that both the daughter branches and the main branch were all more or less positioned in one plane. As mentioned before, in the common carotid artery the mean cross–sectional diameters in two perpendicular directions differed about 10%. The same value was found for the diameters in the internal carotid artery.

It is concluded that the geometry as determined by Balasubramanian (1979) seems to be a reasonable description of the <u>in vivo</u> situation with the exception of the diameter of the common carotid artery and the angles between the daughter branches and the main branch. Besides, it is concluded that large inter–individual variabilities occur in the geometry of the carotid artery bifurcation and that, by presenting a mean geometry, individual characteristics of this geometry are possibly averaged out. Therefore, studies dealing with the influence of geometry variations, like a smaller bifurcation angle, a smaller diameter of the common carotid artery or a less developed bulb, on the total flow field are indispensable.

3 Numerical method for the solution of the unsteady Navier–Stokes equation

3.1 Introduction

In this chapter the methods, as used for discretization of the unsteady Navier–Stokes and continuity equations, are described. Also, the finite element package and the computers employed to solve the fluid problems presented in this study are discussed. Finally, the results of some test calculations are shown.

In section 3.2 the governing equations are presented as well as the boundary and initial conditions needed to solve the velocity and the pressure from the Navier–Stokes and continuity equations. In the next section the method of the weighted residuals is discussed in combination with Galerkin's finite element method, used for the spatial discretization of the governing equations (Cuvelier et al., 1986). This results in a set of ordinary differential equations with velocity and pressure unknowns. To eliminate the pressure unknowns from the discretized Navier–Stokes equation, a penalized formulation is employed for the continuity equation (Cuvelier et al., 1986), described in section 3.4. Next, the local time derivative in the Navier–Stokes equation is approximated by a finite difference method. In section 3.5 the stability regions of the θ–method (Cuvelier et al., 1986) and the explicit Adams–Bashforth time integration scheme (Canuto et al., 1988) and their implications for the discretized Navier–Stokes equation are discussed. For numerical simulation of fluid flow in three–dimensional geometries with the finite element method, these geometries have to be divided into elements. In section 3.6 the 27–noded Crouzeix–Raviart element (Fortin, 1981), as used in the present study, is discussed. In section 3.7 a special purpose mesh generator employed for the division of the carotid artery bifurcation into 27–noded bricks is presented. For the construction of an approximate solution of the Navier–Stokes and continuity equations, the finite element package Sepran was used (Segal, 1984). In section 3.8 some features of this package are presented which facilitate the use of supercomputers. Earlier performed calculations of steady flow in a 90–degree curved tube (van de Vosse, 1989) revealed that large computing times and input/output times were needed to solve the system of equations, resulting from a Galerkin finite element approach. Therefore, super and minisupercomputers are needed which are outlined in section 3.9. Finally, in section 3.10 some numerical test calculations are presented.

3.2 Governing equations

Flow of an incompressible and isothermal fluid is described by the momentum and continuity equations. In dimensionless form these equations read:

$$\mathrm{Sr}\,\dot{\vec{u}} + \vec{u}\cdot\vec{\nabla}\,\vec{u} - \vec{\nabla}\cdot\sigma - \vec{f} = \vec{0} \tag{3.1a}$$

$$\vec{\nabla}\cdot\vec{u} = 0 \tag{3.1b}$$

with $\vec{u}$ the velocity vector, σ the Cauchy stress tensor, $\vec{f}$ the body force per unit mass, $\vec{\nabla}$ the gradient vector operator and $\dot{}$ the local time derivative. The tensor $\vec{\nabla}\,\vec{u}$ is the so–called velocity gradient tensor. Sr denotes the Strouhal number defined as $\mathrm{Sr} = \omega L/U$ with ω a characteristic angular frequency, L a characteristic length and U a characteristic velocity. In this study only Newtonian fluids will be considered for which the Cauchy stress tensor is coupled at the velocity field as:

$$\sigma = -p\mathrm{I} + \frac{1}{\mathrm{Re}}((\vec{\nabla}\,\vec{u})^{c} + (\vec{\nabla}\,\vec{u})) \tag{3.1c}$$

with p the pressure, I the unit tensor and $(\vec{\nabla}\,\vec{u})^{c}$ the conjugate of tensor $(\vec{\nabla}\,\vec{u})$. Re denotes the Reynolds number and is defined as $\mathrm{Re} = UL/\nu$ with ν the kinematic viscosity. To solve the velocity and the pressure from the momentum and continuity equations for $t>t_0$ in a domain Ω with boundary Γ, boundary and initial conditions are required. It can be shown that for the momentum and continuity equations in a D–dimensional space (D=2,3), D boundary conditions are needed for the velocity or stress in D independent directions (Cuvelier et al., 1986). In their general form these boundary conditions read:

$$\left.\begin{array}{ll} \vec{u}\cdot\vec{n} \ \text{ or } \ (\sigma\cdot\vec{n})\cdot\vec{n} = \sigma_n & \text{prescribed} \\ \vec{u}\cdot\vec{t}_d \ \text{ or } \ (\sigma\cdot\vec{n})\cdot\vec{t}_d = \sigma_{td} & \text{prescribed} \end{array}\right\} \text{ on } \Gamma \text{ for } t>t_0 \tag{3.2a}$$

with $\vec{n}$ the normal unit vector and $\vec{t}_d$ (d=1,D–1) the tangential unit vector on Γ. When for an incompressible fluid on part of the boundary the normal stress σ_n is prescribed, no extra boundary conditions for the pressure are necessary (Ladyzhenskaya, 1969). In that case the pressure is fixed implicitly by the normal stress component. As initial condition it is sufficient to prescribe the velocity field at $t = t_0$:

$$\vec{u} \text{ prescribed on } \Omega \text{ for } t = t_0 \qquad (3.2b)$$

In many application fields the dimensionless momentum equation (eq. 3.1a) combined with the constitutive relation for Newtonian fluids (eq. 3.1c) is written in the form:

$$Sr\,\dot{\vec{u}} + \vec{u}\cdot\vec{\nabla}\,\vec{u} - \frac{1}{Re}\Delta\,\vec{u} + \vec{\nabla}\,p - \vec{f} = \vec{0} \qquad (3.3)$$

with Δ the Laplacian operator. In this equation, which is often referred to as the Navier–Stokes equation, some terms are dropped by using the incompressibility requirement (eq. 3.1b). If this equation is used in Galerkin's finite element method for the construction of an approximate solution, instead of the equations 3.1a and 3.1c, differences occur in the resulting system of equations. As the former formulation is used in the finite element package Sepran (Segal, 1984), in the present study discretization of the momentum equation is preferred. In the sequel, the momentum equation will also be referred to as the Navier–Stokes equation.

3.3 Spatial discretization

To obtain an approximation of the velocity and the pressure field within a domain Ω, the method of the weighted residuals is used. Here a synopsis will be given without paying attention to the incorporation of the boundary conditions. For a more precise description the reader is referred to Cuvelier at al. (1986). In this method the residuals of the momentum and continuity equations are required to be orthogonal to all vector functions $\vec{w}$ and scalar functions v, respectively, lying in proper vector spaces W and V. Integration over the domain considered yields:

$$\int_\Omega \vec{w}\cdot[Sr\,\dot{\vec{u}} + \vec{u}\cdot\vec{\nabla}\,\vec{u} - \vec{\nabla}\cdot\sigma - \vec{f}]d\Omega = 0 \qquad \forall\vec{w} \in W \qquad (3.4a)$$

$$\int_\Omega v[\vec{\nabla}\cdot\vec{u}]d\Omega = 0 \qquad \forall v \in V \qquad (3.4b)$$

All components of the vector function $\vec{w}$ and their partial derivatives in space as well as the scalar function v must be square integratable over the domain Ω. Using integration by parts and Gauss' theorem, the first equation is transformed to:

$$\int_{\Omega}[Sr\ \vec{w}\cdot\dot{\vec{u}} + \vec{w}\cdot\vec{u}\cdot(\vec{\nabla}\,\vec{u}) + (\vec{\nabla}\,\vec{w})^{c}:\sigma]d\Omega = \int_{\Omega}\vec{w}\cdot\vec{f}d\Omega + \int_{\Gamma}\vec{w}\cdot\vec{t}d\Gamma \quad \forall\vec{w}\in W \quad (3.5)$$

with $\vec{t}$ the stress vector defined as $\vec{t} = \sigma\cdot\vec{n}$, $\vec{n}$ being the outward normal unit vector on boundary Γ. Equations 3.5 and 3.4b are suitable for discretization with the finite element method. In this method the region Ω is divided into elements. Every element consists of a number of nodal points for the velocity and the pressure and the unknowns $\vec{u}$ and p are supposed to be a linear combination of the values of these unknowns in the nodal points:

$$\vec{u}(\vec{x},t) = \sum_{i=1}^{N} \varphi_i(\vec{x})\,\vec{u}_i(t) \quad (3.6a)$$

$$p(\vec{x},t) = \sum_{i=1}^{M} \psi_i(\vec{x})\,p_i(t) \quad (3.6b)$$

with N the total number of nodal points for the velocity and M the total number of nodal points for the pressure. The functions φ_i and ψ_i are the so–called basis functions for the velocity and the pressure in nodal point i, respectively. These functions are fully determined by the position vector $\vec{x}$. The symbols $\vec{u}_i$ and p_i present the velocity vector and the pressure in nodal point i, respectively, and are only functions of time. The velocity and pressure fields in the domain under consideration are, therefore, completely determined by the basis functions and the nodal point values. To solve the system of equations also assumptions must be made for the weight functions $\vec{w}$ and v. To this end finite dimensional subspaces $W_h \subset W$ and $V_h \subset V$ are constructed and the equations 3.4b and 3.5 should be true for $\vec{w}_h \in W_h$ and $v_h \in V_h$. Within the Galerkin method the basis functions for the velocity and the pressure are used to define these subspaces. In other words W_h is spanned by the set $\{\varphi_i,\ i=1,N\}$ and V_h is spanned by the set $\{\psi_i,\ i=1,M\}$. Therefore, the arbitrary weight functions $\vec{w}_h$ and v_h can be written as:

$$\vec{w}_h(\vec{x},t) = \sum_{i=1}^{N} \varphi_i(\vec{x})\vec{w}_i(t) \tag{3.7a}$$

$$v_h(\vec{x},t) = \sum_{i=1}^{M} \psi_i(\vec{x})v_i(t) \tag{3.7b}$$

Substitution of the equations 3.6 and 3.7 into the equations 3.5 and 3.4b leads to:

$$\sum_{i=1}^{N} \vec{w}_i \cdot \{ \int_{\Omega} [\mathrm{Sr}\varphi_i \sum_{j=1}^{N} \varphi_j \dot{\vec{u}}_j + \varphi_i \sum_{j=1}^{N} \varphi_j \sum_{l=1}^{N} (\vec{\nabla}\, \varphi_l \vec{u}_l)^c \cdot \vec{u}_j + \sigma^c \cdot \vec{\nabla}\varphi_i] d\Omega \} =$$

$$= \sum_{i=1}^{N} \vec{w}_i \cdot \{ \int_{\Omega} \varphi_i \vec{f} d\Omega + \int_{\Gamma} \varphi_i \vec{t} d\Gamma \} \qquad \forall \vec{w}_h \in W_h \tag{3.8a}$$

$$\sum_{i=1}^{M} v_i \int_{\Omega} \psi_i \sum_{j=1}^{N} \vec{\nabla}\varphi_j \cdot \vec{u}_j d\Omega = 0 \qquad \forall v_h \in V_h \tag{3.8b}$$

The requirement that these equations must hold for all admissable vector functions $\vec{w}_h$ and scalar functions v_h, substitution of the constitutive relation for Newtonian fluids (eq. 3.1c) and presentation in a Cartesian coordinate system leads to a matrix equation. With a gradient operator, a velocity and a pressure column defined as:

$$\underset{\sim}{\nabla}^T = [\partial/\partial x_1,\ldots,\partial/\partial x_D]$$

$$\underset{\sim}{U}^T = [\underset{\sim}{u}_1^T,\ldots,\underset{\sim}{u}_N^T]$$

$$\underset{\sim}{P}^T = [p_1,\ldots,p_M]$$

and $\underline{I}$ being a D–dimensional unit matrix and DN being DxN this matrix equation reads:

$$\underline{M}\, \dot{\underset{\sim}{U}} + [\underline{S} + \underline{N}(\underset{\sim}{U})]\underset{\sim}{U} + \underline{L}^T \underset{\sim}{P} = \underset{\sim}{F} + \underset{\sim}{B} \tag{3.9a}$$

$$\underline{L}\, \underset{\sim}{U} = \underset{\sim}{0} \tag{3.9b}$$

with $\underline{M}$ the mass matrix (DNxDN):

$$\underline{M}^{ij} = \mathrm{Sr} \int_{\Omega} \varphi_i \varphi_j\, \underline{I}\, d\Omega \qquad i=1,N;j=1,N \tag{3.10a}$$

$\underline{S}$ the diffusion matrix (DNxDN):

$$\underline{S}^{ij} = \frac{1}{Re}\int_{\Omega}[(\nabla\varphi_i^T \nabla\varphi_j)\underline{I} + \nabla\varphi_i \nabla\varphi_j^T]d\Omega \qquad i=1,N;j=1,N \qquad (3.10b)$$

$\underline{N}(\underset{\sim}{U})$ the convection matrix (DNxDN):

$$\underline{N}(\underset{\sim}{U})^{ij} = \int_{\Omega}\varphi_i\varphi_j\sum_{l=1}^{N}(\nabla\varphi_l\, \underset{\sim}{u}_l^T)d\Omega \qquad i=1,N;j=1,N \qquad (3.10c)$$

$\underline{L}$ the divergence matrix (MxDN):

$$(\underline{L}^T)^{ij} = -\int_{\Omega}\psi_j\nabla\varphi_i d\Omega \qquad i=1,N;j=1,M \qquad (3.10d)$$

$\underset{\sim}{F}$ the body force column (DNx1):

$$\underset{\sim}{F}^i = \int_{\Omega}\varphi_i\underset{\sim}{f}d\Omega \qquad i=1,N \qquad (3.10e)$$

and $\underset{\sim}{B}$ the boundary stress column (DNx1):

$$\underset{\sim}{B}^i = \int_{\Gamma}\varphi_i\underset{\sim}{t}d\Gamma \qquad i=1,N \qquad (3.10f)$$

In this presentation $\underline{M}^{ij}$, $\underline{S}^{ij}$ and $\underline{N}(\underset{\sim}{U})^{ij}$ are square matrices and $(\underline{L}^T)^{ij}$, $\underset{\sim}{F}^j$ and $\underset{\sim}{B}^j$ are column matrices with dimensions DxD and Dx1, respectively, representing a dimension expansion (D=2,3). For example, $\underline{M}^{kl}$ corresponds to elements in the system matrix ranging from row (k–1)D+1 to row (k–1)D+D and from column (l–1)D+1 to (l–1)D+D.

3.4 Penalty function method

The set of equations resulting from Galerkin's finite element method (eq. 3.9) has a special character due to the absence of the pressure unknowns in the discretized continuity equation. For the linear case this type of problem is a so–called saddle–point problem, for which iterative solution methods are hard to find. Most iterative algorithms in literature are based upon a variant of the Uzawa scheme (Fortin and Glowinski, 1983). A disadvantage of these algorithms is their slow convergence behavior. If a direct method is used, the absence of the pressure unknowns in the discretized continuity equation may cause zeros on the main diagonal, unless a suitable numbering is chosen. The search for such a suitable numbering is quite complicated and not easy to program. If zeros on the main diagonal are present and a direct solving technique is applied partial pivoting is necessary. Partial pivoting procedures, however, are very time and memory consuming and should be avoided if possible. Therefore, the penalty function method is applied which has been described in detail by Cuvelier et al. (1986). In short, in this method the continuity equation is replaced by:

$$\vec{\nabla}\cdot\vec{u} = -\epsilon p \tag{3.11}$$

with ϵ a very small parameter. If the right hand side ϵp is small enough within the domain Ω then the incompressibility of the fluid will be sufficiently approximated. It can be shown that for both the Stokes and Navier–Stokes equations, the solution of the penalty function approach converges to the solution of the unperturbed system for small values of the parameter ϵ (Pelissier, 1975; Temam, 1977). In the same way as the unperturbed continuity equation, eq. 3.11 can be discretized by Galerkin's finite element method, which leads to:

$$\underline{L}\underset{\sim}{U} = \epsilon \underline{M}_p \underset{\sim}{P} \tag{3.12}$$

with $\underline{M}_p$ the pressure matrix (MxM):

$$\underline{M}_p^{ij} = \int_\Omega \psi_i \psi_j d\Omega \qquad i=1,M;j=1,M \tag{3.13}$$

Because of the special structure of the basis functions for the pressure in the element used, the inverse of the pressure matrix is easily determined which leads to an explicit equation for the pressure unknowns. Substitution of this relation into the discretized Navier–Stokes equation (eq. 3.9a) leads to:

$$\underline{\underline{M}}\,\dot{\underset{\sim}{U}} + [\underline{\underline{S}} + \underline{\underline{N}}(\underset{\sim}{U})]\underset{\sim}{U} + \frac{1}{\epsilon}\underline{\underline{L}}^T\underline{\underline{M}}_p^{-1}\underline{\underline{L}}\underset{\sim}{U} = \underset{\sim}{F} + \underset{\sim}{B} \qquad (3.14)$$

which contains only unknowns for the velocity. Beside that for this system of equations the number of unknowns is smaller than for the original system, for direct solving techniques no partial pivoting is needed to solve the velocity unknowns from eq. 3.14. A disadvantage of the penalty function approach is the choice of the value of the penalty parameter ϵ. The matrix $\underline{\underline{L}}^T\underline{\underline{M}}_p^{-1}\underline{\underline{L}}$ is singular due to the singularity of $\underline{\underline{L}}$. Therefore, for too small values of ϵ the total system matrix becomes singular, whereas too large values of this parameter lead to an inadmissable compressibility of the fluid. For the problems solved in this study the value of ϵ was chosen to be $\epsilon=10^{-5}$, which leads to values of ϵp (eq. 3.11) of $O(10^{-5})$ in the dimensionless formulation. Due to the bad condition of the system matrix of eq. 3.14, iterative methods are not suitable for solving the velocity unknowns from the system of equations resulting from a penalty function approach.

From the equations 3.10 and 3.13 it is easily verified that the matrices $\underline{\underline{M}}$, $\underline{\underline{S}}$ and $\underline{\underline{L}}^T\underline{\underline{M}}_p^{-1}\underline{\underline{L}}$ are symmetric. The convection matrix $\underline{\underline{N}}$, however, is asymmetric due to the discretized form of the velocity gradient tensor in eq 3.10c. Therefore, symmetric solvers like LDL^T– and GG^T–decomposition of the system matrix, are not suitable here, and one is forced to use an asymmetric LU–factorization technique (Cuvelier et al., 1986).

3.5 Time integration

3.5.1 Finite difference schemes

To solve the velocity unknowns from eq. 3.14, the local time derivative is approximated by a finite difference method. Consider a set of ordinary differential equations resulting from the discretization of a parabolic differential equation:

$$\dot{\underset{\sim}{u}} = \underline{\underline{A}}\,\underset{\sim}{u} + \underset{\sim}{f} \qquad (3.15)$$

A commonly used finite difference scheme is the θ–method (Cuvelier et al., 1986):

$$\frac{\underset{\sim}{u}^{n+1}-\underset{\sim}{u}^{n}}{\Delta t} = (\underline{A}\underset{\sim}{u} + \underset{\sim}{f})^{n+\theta}$$
$$= \theta(\underline{A}\underset{\sim}{u}^{n+1} + \underset{\sim}{f}^{n+1}) + (1-\theta)(\underline{A}\underset{\sim}{u}^{n} + \underset{\sim}{f}^{n}) \tag{3.16}$$

in which $\underset{\sim}{u}^n$ is an abbreviation for $\underset{\sim}{u}(n\Delta t)$ with Δt the time step. The parameter θ varies between $0 \leq \theta \leq 1$. For $\theta=1$ this scheme reduces to the Euler–implicit scheme and for $\theta=0$ to the Euler–explicit scheme, both $O(\Delta t)$ accurate in time. For $\theta=0.5$ this scheme is known as the Crank–Nicolson scheme which is $O(\Delta t^2)$ accurate in time. A great advantage of the Euler–explicit scheme over the other schemes is that no system of equations needs to be solved. Another explicit time integration scheme which is $O(\Delta t^2)$ accurate in time is the so–called Adams–Bashforth scheme (Canuto et al., 1988):

$$\frac{\underset{\sim}{u}^{n+1}-\underset{\sim}{u}^{n}}{\Delta t} = \tfrac{3}{2}(\underline{A}\underset{\sim}{u}^{n} + \underset{\sim}{f}^{n}) - \tfrac{1}{2}(\underline{A}\underset{\sim}{u}^{n-1} + \underset{\sim}{f}^{n-1}) \tag{3.17}$$

This scheme is a two–step method because two solutions at previous time–steps are required, whereas the θ–method is a one–step method. Because a two–step method requires two initial solutions, in most cases the first time step a one–step method is applied.

Beside the accuracy of a finite difference method, also the stability of the scheme has to be taken into account. If matrix $\underline{A}$ has only real coefficients independent of time, resulting from the discretization of a linear elliptic differential operator, and if A is not–defect, i.e. the number of independent eigenvectors of $\underline{A}$ is equal to the order of $\underline{A}$, then a numerical time integration scheme generally leads to a set of equations of the form (appendix A):

$$\underset{\sim}{\chi}^{n+1} = \underline{G}\underset{\sim}{\chi}^{n} \tag{3.18}$$

with $\underline{G}$ the amplification matrix and $\underset{\sim}{\chi}$ some kind of error column. For stability of the time integration scheme according to the matrix method (Mitchell and Griffiths, 1980), it is necessary that:

$$\rho_G = |\lambda_G|_{max} < 1 \tag{3.19}$$

with ρ_G the spectral radius and $|\lambda_G|_{max}$ the modulus of the absolutely largest eigenvalue of the amplification matrix. From a stability analysis with the matrix method, it can be shown that for a set of equations as presented in eq. 3.15, the θ–method is unconditionally stable for $\theta \geq 0.5$, whereas for $\theta < 0.5$ conditional stability occurs (Cuvelier et al., 1986). The Adams–Bashforth method is only conditionally stable (Canuto et al., 1988). Figure 3.1a shows the stability regions for $\theta=0$ and the Adams–Bashforth method as function of $\lambda_A \Delta t$ with λ_A the eigenvalues of matrix $\underline{A}$.

It is observed that the smallest stability region occurs for the explicit Adams–Bashforth method. If a conditionally stable method is used and the eigenvalues λ_A have a large negative real or large imaginary part, very small time steps have to be applied to ensure stability. Figure 3.1b gives a presentation of ρ_G for real values of $\lambda_A \Delta t$ for the θ–method (θ=1,0.5,0) and for the Adams–Bashforth scheme. In spite of the fact that the Crank–Nicolson scheme is unconditionally stable, for large negative real values of $\lambda_A \Delta t$, ρ_G tends to 1 which means that an undamped behavior of the error column may be expected. For the Euler–implicit time integration scheme, ρ_G tends to 0 for large negative real values of $\lambda_A \Delta t$. In many application fields a combination of these two methods is used. First, several Euler–implicit time steps are applied to damp numerical errors in the solution induced by the assumed initial condition. Second, the Crank–Nicolson scheme is applied to achieve a higher accuracy of the approximate solution.

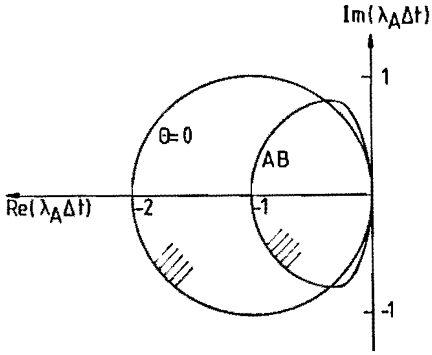

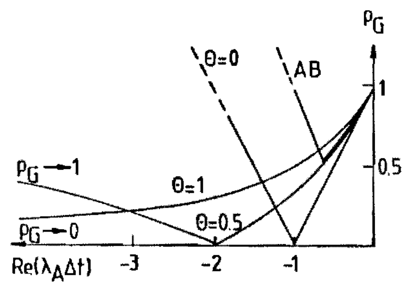

Figure 3.1: Stability regions (///, a) and spectral radii (b) for the θ–method and the Adams–Bashforth integration scheme.

3.5.2 Application to the Navier–Stokes equation

Using the θ–method to approximate the local time derivative in eq. 3.14 yields:

$$\underline{M}\frac{\underset{\sim}{U}^{n+1}-\underset{\sim}{U}^{n}}{\Delta t} + [\underline{S} + \underline{N}(\underset{\sim}{U}^{n+\theta}) + \frac{1}{\epsilon}\underline{L}^{T}\underline{M}_{p}^{-1}\underline{L}]\underset{\sim}{U}^{n+\theta} = \underset{\sim}{F}^{n+\theta} + \underset{\sim}{B}^{n+\theta} \tag{3.20}$$

The non–linear convective term $N(\underset{\sim}{U}^{n+\theta})\underset{\sim}{U}^{n+\theta}$ is linearized by one step of a Newton–Raphson iteration scheme (Cuvelier et al., 1986):

$$\underline{N}(\underset{\sim}{U}^{n+\theta})\underset{\sim}{U}^{n+\theta} = \underline{J}(\underset{\sim}{U}^{n})\underset{\sim}{U}^{n+\theta} - \underline{N}(\underset{\sim}{U}^{n})\underset{\sim}{U}^{n} \tag{3.21}$$

with $\underline{J}(\underset{\sim}{U})$ the Jacobian matrix of $\underline{N}(\underset{\sim}{U})\underset{\sim}{U}$ (DNxDN) defined as:

$$\underline{J}(\underset{\sim}{U})^{ij} = \int_{\Omega}[\varphi_i\varphi_j\sum_{l=1}^{N}(\underset{\sim}{\nabla}\varphi_l\, \underset{\sim}{u}_l^{T}) + \varphi_i\sum_{l=1}^{N}\varphi_l(\underset{\sim}{\nabla}\varphi_j^{T}\, \underset{\sim}{u}_l)\underline{I}]d\Omega \tag{3.22}$$

Using this linearization technique and the equation:

$$\underset{\sim}{U}^{n+\theta} = \theta\underset{\sim}{U}^{n+1} + (1-\theta)\underset{\sim}{U}^{n} \tag{3.23}$$

leads to:

$$[\underline{M}/\theta\Delta t + \underline{S} + \underline{J}(\underset{\sim}{U}^{n}) + \frac{1}{\tau}\underline{L}^{T}\underline{M}_{p}^{-1}\underline{L}]\underset{\sim}{U}^{n+\theta} = [\underline{M}/\theta\Delta t + \underline{N}(\underset{\sim}{U}^{n})]\underset{\sim}{U}^{n} + \underset{\sim}{F}^{n+\theta} + \underset{\sim}{B}^{n+\theta} \tag{3.24}$$

which is an Euler–implicit step from $\underset{\sim}{U}^{n}$ to $\underset{\sim}{U}^{n+\theta}$. The solution $\underset{\sim}{U}^{n+1}$ is calculated afterwards from extrapolation of $\underset{\sim}{U}^{n}$ and $\underset{\sim}{U}^{n+\theta}$ to $\underset{\sim}{U}^{n+1}$ using eq. 3.23. Both schemes are in principal $O(\Delta t)$ accurate in time but a combination of these two methods, as described above, is similar to a Crank–Nicolson scheme which is $O(\Delta t^2)$ accurate in time (van de Vosse, 1987). If a LU–decomposition is used to calculate $\underset{\sim}{U}^{n+\theta}$ from eq. 3.24, at every time–step a system of equations has to be solved because the Jacobian matrix is a function of the solution itself. For three–dimensional flow problems LU–factorization of the system matrix can be very time consuming. When an explicit integration method is used for the convective term, the LU–factorization has to be carried out only once. Therefore, it may be useful to combine an explicit method for the convective term with an implicit method for the other terms. Applying the Adams–Bashforth method and the Crank–Nicolson scheme to eq. 3.14 leads to:

$$[2\underline{M}/\Delta t + \underline{S} + \tfrac{1}{\epsilon}\underline{L}^T\underline{M}_p^{-1}\underline{L}]\underset{\sim}{U}^{n+1/2} = [2\underline{M}/\Delta t - \tfrac{3}{2}\underline{N}(\underset{\sim}{U}^n)]\underset{\sim}{U}^n + \\ + \tfrac{1}{2}\underline{N}(\underset{\sim}{U}^{n-1})\underset{\sim}{U}^{n-1} + \underset{\sim}{F}^{n+1/2} + \underset{\sim}{B}^{n+1/2} \qquad (3.25)$$

which is $O(\Delta t^2)$ accurate in time. If an Euler–implicit scheme is used, it is sufficient to approximate the convective term with an Euler–explicit scheme because both methods are $O(\Delta t)$ accurate in time. In a previous section it was shown that for linear parabolic differential equations explicit methods are only conditionally stable. As for large Reynolds numbers the convective term becomes more important, it is reasonable to presume that the time step needed to solve eq. 3.25 will be smaller than the time step needed to solve eq. 3.24.

3.6 The element used

To solve the Navier–Stokes equation within a domain Ω, the domain has to be divided into elements and assumptions have to be made about the basis functions for the velocity and the pressure. From the discretized Navier–Stokes and continuity equations it can easily be shown that the basis functions for the velocity must be piecewise continuously differentiable and continuous over the element boundaries. The basis functions for the pressure must be continuous in each element. A three–dimensional element satisfying these requirements is the 27–noded element presented in figure 3.2.

Velocity unknowns are defined in all the nodal points of the element which means 81 velocity unknowns per element. In the reference element the basis functions related to each nodal point (eq. 3.6a) are triquadratic functions (Cuvelier et al., 1986). Pressure unknowns are only defined in the center of the element, which are the pressure itself and its three spatial derivatives. The basis functions in the reference element related to the pressure unknowns (eq. 3.6b) are a constant and three linear functions. Since these functions are zero outside the element under consideration, the pressure field varies discontinuously over the element boundaries. This type of element belongs to the group of the so–called Crouzeix–Raviart elements (Crouzeix and Raviart, 1973). An alternative group of elements consists of the Taylor–Hood elements (Taylor and Hood, 1973), which have a continuous pressure field over the element boundaries. An advantage of the Crouzeix–Raviart elements over the Taylor–Hood elements in combination with a penalty function approach for the incompressibility requirement, is the property that the inverse of the pressure matrix (eq. 3.12) can be calculated elementwise (Cuvelier et al., 1986). Besides, Crouzeix–Raviart elements satisfy the continuity equation elementwise, whereas Taylor–Hood elements satisfy this equation only on Ω.

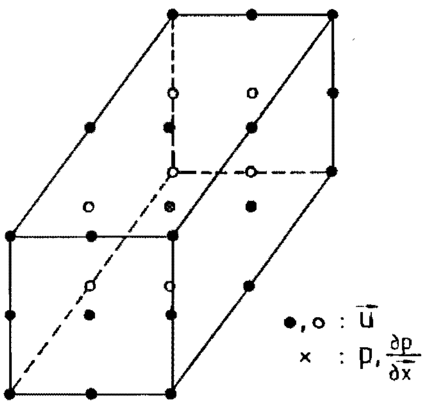

Figure 3.2: The 27–noded Crouzeix–Raviart element.

For Crouzeix–Raviart elements it is possible to eliminate the velocity unknowns and the pressure derivatives within the centroid of the element by consideration of the Navier–Stokes and continuity equations elementwise (Cuvelier et al., 1986). For the triangular quadratic element in two dimensions this leads to a reduction for the velocity unknowns of about 15%. For the 27–noded Crouzeix–Raviart element it reduces the total number of velocity unknowns by 3 to 78 (4%). Because this reduction is relatively small and, for post–processing reasons, the eliminated unknowns have to be calculated afterwards, this reduction technique was not carried out for the 27–noded element.

With regard to the incompressibility requirement Fortin and Fortin (1985) states that numerical experience indicates that the 27–noded element, as used in this study, is a too compressible, too soft element since the pressure imposes only 4 constraints on the 81 degrees of freedom for the velocity. However, because of the special structure of the basis functions for the pressure, it can be shown that the divergence freedom of the velocity field is satisfied elementwise, which seems to be contradictory with the observations of Fortin and Fortin (1985).

In order to construct an appropriate approximation of the solution of the Navier–Stokes and continuity equations, the element has to satisfy the so–called Brezzi–Babuska condition (Brezzi, 1974), which is a rather abstract condition and difficult to verify. A rather simple method to check the Brezzi–Babuska condition is given by Fortin (1981), who also states that the 27–noded Crouzeix–Raviart element, as used in this study, satisfies this condition. In practice, it is mostly sufficient to require that the order of the basis functions for the pressure are at least one degree less than that of the basis functions for the velocity, and that the number of pressure unknowns is essentially smaller than the number of velocity unknowns. The latter implies that the velocity field is not fully determined by the continuity equation. These conditions hold for the 27–noded Crouzeix–Raviart element. Other important reasons for using this element are that it was found to be successful for the calculation of steady flow in a 90–degree curved tube (van de Vosse et al., 1989) and that the accuracy of the approximation was found to be $O(h^3)$ for a simple test example (Segal, 1986) with h a characteristic element size.

3.7 Division of the carotid artery bifurcation into elements

To approximate the solution of the Navier–Stokes and continuity equations with the finite element method, the domain under consideration has to be divided into elements. For two–dimensional problems many commercial software packages are developed, which are able to divide any two–dimensional domain into triangles or rectangles. For three–dimensional problems only a few of such so–called mesh generators are available. Usage of these mesh generators for the division of complex geometries into elements generally leads to a too large number of elements. This problem is even more important when for a three–dimensional geometry hexahedrons instead of tetrahedrons are used. The former elements have rather complex "connection–rules" which means that steep gradients of the element sizes in the element division in general implies a large number of elements.

To divide the carotid artery bifurcation into a limited number of hexahedrons, it was decided to develop a special purpose mesh generator ourselves. Therefore, the plane of symmetry of the carotid artery bifurcation was divided into rectangles with 4 nodal points as shown in figure 3.3a. The plane of symmetry was divided into three regions, indicated by A, B and C. Regions A and C have circular cross–sections, whereas in region B the main branch divides itself into two daughter branches. Divider line D is the projection on the plane of symmetry of the intersection curve of the two daughter branches. This line was not allowed to cross an element boundary.

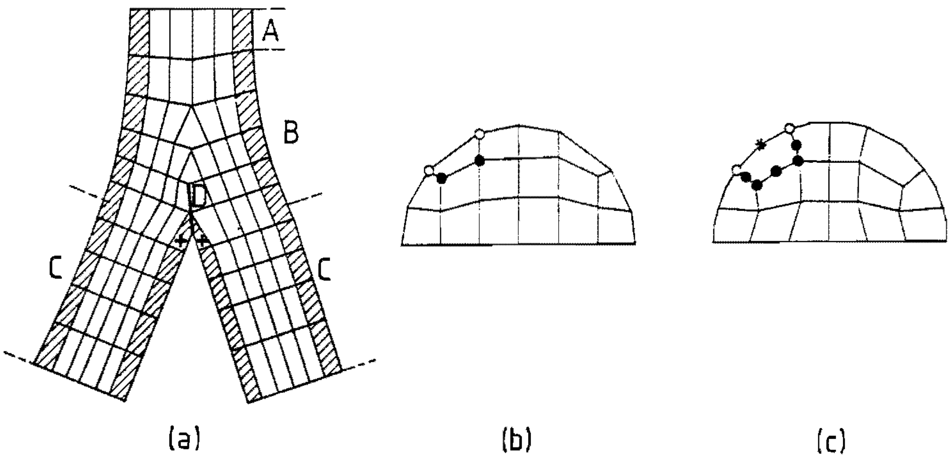

Figure 3.3: Three stages of the mesh generator for the carotid artery bifurcation.

The two–dimensional element division was expanded in the third direction by placing 8–noded hexahedrons on it as indicated in figure 3.3b. For the boundary region, indicated in figure 3.3a by shaded lines, the number of elements in the third direction was one less than for the inner region. The external nodal points (fig. 3.3b and 3.3c, open circles) were positioned at the outer surface of the carotid artery bifurcation, as best as possible. After repositioning of the internal nodal points (fig. 3.3b and 3.3c, closed circles), so that the maximal angle between two element boundaries of an element was as small as possible, the 8–noded hexahedrons were transformed into 27–noded hexahedrons (fig. 3.3c). Finally, the midpoints of the external points (fig. 3.3c, asterisks) were positioned at the outer surface. To position the external points and the midpoints at the outer surface of the carotid artery bifurcation, in an upscaled model the geometry of region B was determined in about 400 points. For the main and both daughter branches (regions A and C) rotational symmetry was assumed and only the diameters were measured. Due to the special structure of the mesh generator, some ill–shaped elements occurred in the region near the flow divider, indicated in figure 3.3a by cross marks. The largest angles between two element boundaries were 143° and 162° for the internal and the external carotid artery, respectively, whereas an angle of 90° is supposed to be ideal. These large angles may cause errors in the calculated flow field near the flow divider.

3.8 The finite element package Sepran

For the construction of an approximate solution of the Navier–Stokes and continuity equations, the finite element package Sepran was used (Segal, 1984). Globally, the Sepran package can be divided into subroutines handling the mesh generation, a computational part consisting of a problem definition and a problem solution part, and subroutines for postprocessing purposes. The input and output possibilities of the computational part are arranged in such a way that one can use his own preprocessor and/or postprocessor. The package consists of a large number of subroutines, written in Standard Fortran, and contains as less as possible machine dependent subroutines. For most of its basic linear operations the package uses BLAS–routines (Lawson et al., 1979), which have optimal codes implemented on almost every computer, including super and minisupercomputers. Therefore, implementation of the package on the super and minisupercomputers, as used in this study, was relatively simple and optimization of the code for vectorization purposes was hardly necessary. The latter aspect highly depends on the kind of problems studied. For the problems solved in this study, however, most of the computing time was spended to LU–decomposition of the system matrix, which can be fully performed by BLAS–routines.

Discretization of the Navier–Stokes and continuity equations in combination with a penalty function approach leads to a system matrix with a symmetric profile structure. To economize the memory usage a profile storage technique was used. In the package, a one–dimensional array is employed for a row–columnwise storage of the system matrix and a row–columnwise LU–decomposition procedure is available for solving the system of equations by a direct method, resulting in optimal code for supercomputers. The system matrix can be stored on either disk or virtual memory. For most cases the latter one is the most suitable, because communication with virtual memory generally occurs by page faults handled by the operating system of the computer itself. This is much faster than communication with disk, which has to be carried out by the user himself in the form of Fortran input/output statements.

3.9 Supercomputers to solve large systems of equations

Earlier performed calculations of steady entrance flow in a 90–degree curved tube (van de Vosse et al., 1989) revealed that large computing times (CPU–times) and input/output times (I/O–times) were needed to solve the system of equations resulting from a Galerkin finite element approach. For instance, for the 2205–noded element division, as used by van de Vosse et al. (1989), one iteration on a minicomputer (Apollo–dsp90) took about 24 hours CPU–time and 48 hours I/O–time. These numbers have to be interpreted with care because they are highly dependent on the configuration of the computer used. For example, for reasons pointed out in appendix C, the I/O–time needed for the calculations of van de Vosse et al. (1989) would be essentially smaller when the central memory of the Apollo–dsp90 used, was about twice as big. Nevertheless, it may be concluded that for calculations of fluid flow in 3D–models of the carotid artery bifurcation faster computers, like super and minisupercomputers, are needed.

Super and minisupercomputers can be 10 to 1000 times as fast as conventional computers concerning their CPU–speed. In appendix B the peak performances of several systems are given and compared with their real speeds, as achieved for the problems solved in this study. Another important aspect is the I/O–time needed for a calculation. In appendix C it is pointed out that large I/O–times are needed if the capacity of the central memory is too small, as compared with the bandwidth of the system matrix. With N_c the capacity of the central memory and $N_b=0.5b^2$, b being the bandwidth of the system matrix, enormous I/O–times will occur if $N_c<N_b$.

In principal there are three ways to avoid this problem. The first and most straight forward method is to reduce the number of elements in such a way that the inequality $N_b<N_c$ is satisfied. The limit of this reduction is dictated by the physics of the fluid flow under consideration. In practice, however, it was found that if the inequality $N_b<N_c$ was not satisfied, beside large I/O–times also unacceptable large CPU–times were needed to solve the fluid problems with the computers used in the present study. A second method to achieve smaller I/O–times is to make use of special LU–factorization techniques which recognize the page faulting problem. Such techniques are successfully applied to full square matrices. A disadvantage of these techniques is that they make use of the backing storage device, which is

essentially slower than the use of the virtual memory system. Also, it is not known what the implications of such techniques are for band matrices. A third method to minimize the page faults needed is to renumber the unknowns in such a way that the bandwidth of the system matrix is as small as possible. In the finite element package used the Cuthill–McKee (Cuthill and McKee, 1969) and the Sloan (Sloan, 1986) renumbering procedure are available, of which the Sloan renumbering is superior compared to the Cuthill–McKee renumbering when quadratic elements are used. An example of the effect of these renumbering procedures on the profile of the system matrix is given below. For the problems solved in the present study a combination of the first and the third method was used to minimize the CPU–times and I/O–times needed.

3.10 Numerical test calculations

3.10.1 Steady entrance flow in a 90–degree curved tube

In a pilot–study on the Cyber–205 steady entrance flow in a 90–degree curved tube was investigated at a Reynolds number of 100. The problem definition was the same as described by van de Vosse et al. (1989), who used an element division consisting of 10 elements in axial direction and 22 elements per cross–section with a total of 2205 nodal points. Because of symmetry only half of the curved tube was considered. If Cuthill–McKee renumbering was applied to the nodal points, the I/O–time needed was about 10 times larger then the CPU–time needed to solve the system of equations, due to the enormous amount of page faults occurring. Figure 3.4a shows the profile of the system matrix after Cuthill–McKee renumbering. For this problem the maximal number of matrix elements needed in–core was N_b=788412, whereas the maximal number of elements, which could be stored in central memory, was N_c=786432. From these numbers it is concluded that, for at least part of the system matrix, $N_c<N_b$, resulting in large I/O–times. If Sloan renumbering was used, the profile of the matrix looked as presented in figure 3.4b. The local bandwidth of this matrix is changing rapidly, whereas, the maximal bandwidth is about the same as for Cuthill–McKee renumbering. The maximal number of elements needed in–core was reduced to N_b=408367. On the Cyber–205 the I/O–time was about the same as the CPU–time needed for solving the system of equations. In case of Sloan renumbering the total CPU–time and the number of matrix elements were also reduced with a factor 2 compared to Cuthill–McKee

renumbering.

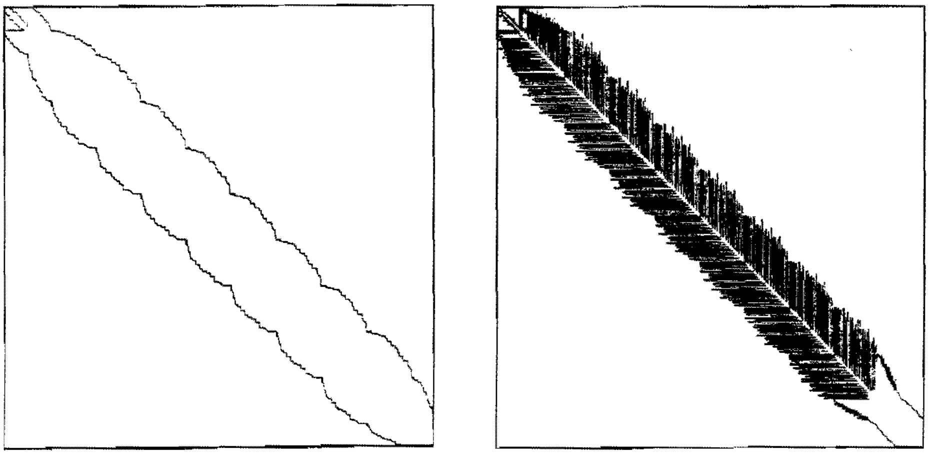

(a) (b)

Figure 3.4: Profile of the system matrix after Cuthill—Mckee renumbering (a) and Sloan renumbering (b).

3.10.2 Fully developed unsteady flow in a circular pipe

At the start of this study, the finite element package Sepran was not able to deal with unsteady flow in three–dimensional geometries. To test the implementation of the mass matrix (eq. 3.10a) for three–dimensional problems, the simple problem of fully developed unsteady flow in a circular pipe was studied and compared with analytical solutions (Schlichting, 1979). For the dimensionless problem the length/diameter ratio of the tube was L/D=1. The Reynolds number varied sinusoidally between 0<Re<400 and the Womersley parameter, often used instead of the Strouhal number and defined as $\alpha=a(\omega/\nu)^{1/2}$ with a the radius of the tube, was equal to 10. At the inlet of the tube in axial direction a fully developed pipe flow was prescribed ($\alpha=10$, –200<Re<200) superimposed on a parabolic velocity profile (Re=200), while both secondary velocity components were set equal to zero. The outlet was presumed to be stress free. The domain was divided into 2 elements in axial direction and 11 elements per cross–section. Due to symmetry, only a quarter of the tube was considered. Because flow at the inlet was fully developed, the axial velocity profile at the outlet had to be the same as the prescribed inlet profile. Figure 3.5 shows these profiles as function of time. The agreement is quite satisfactory. Errors occurring were not larger than 2% of the time–averaged mean axial velocity.

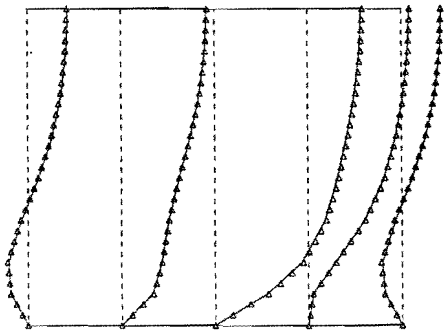

Figure 3.5: Comparison between the prescribed inlet (solid lines) and the calculated outlet (triangles) axial velocity profiles as function of time.

3.10.3 Unsteady entrance flow in a circular pipe

For large systems of equations LU–factorization of the matrix takes about 75% of total CPU–time. Applying a fully explicit time integration scheme to the convective acceleration term in the momentum equation, results in a system matrix which is constant in time. Therefore, LU–factorization has to be carried out only once, which, at first sight, seems to be very attractive. However, smaller time steps are needed for convergence of the solution because explicit methods are only conditionally stable.

To study the ratio of time steps needed for the unconditionally stable and the conditionally stable time integration schemes, unsteady entrance flow in a circular tube has been studied for the two–dimensional axisymmetrical case. The ratio of the length of the tube and the diameter was L/D = 1. The Womersley parameter was $\alpha = 10$ and the minimal Reynolds number was $Re_{min}=0$. At the inlet of the tube a parabolic axial velocity profile was prescribed which varied sinusoidally in time, while the radial velocity component was set equal to zero. At the outlet both normal and tangential stresses were presumed to be zero. For the conditionally stable time integration scheme the solution of the unconditionally stable time integration scheme was used as initial condition.

First, the unconditionally stable Euler–implicit (EI) method and the conditionally stable Euler–explicit (EE) method for the convective term were combined with the Euler–implicit method for the other terms. Both schemes are

$O(\Delta t)$ accurate in time. Next, the unconditionally stable Crank–Nicolson (CN) scheme and the conditionally stable Adams–Bashforth (AB) scheme were combined with a Crank–Nicolson scheme, resulting in a time integration scheme $O(\Delta t^2)$ accurate in time. Table 3.6 shows the time steps needed in one period as function of the maximal Reynolds number (Re_{max}) for the conditionally stable time integration schemes. For the unconditionally stable schemes always 16 time steps per period were applied. A maximal difference between the solutions at the end of two successive periods smaller than 1% of the mean axial velocity was used as stability criterion.

Re_{max}	EI–EE	CN–AB
100	$16<N<24$	$24<N<32$
200	$80<N<100$	$80<N<100$
300	$180<N<200$	$180<N<200$

Table 3.6: Number of time steps needed (N) for the conditionally stable time integration schemes.

From table 3.6 it is concluded that for large Reynolds numbers many time steps are required for stability. The number of time steps needed is almost the same for both schemes. This seems to be contradictory to the findings in section 3.5, where it is stated that the stability region for the Adams–Bashforth scheme is smaller than the one for the Euler explicit scheme. However, it must be kept in mind that the theory presented in section 3.5 is only valid for linear parabolic differential equations with coefficients constant in time. This is certainly not valid for the Navier–Stokes equation. Besides, for eigenvalues with large imaginary parts, as compared to the real parts, the stability regions of the Euler–explicit and Adams–Bashforth integration schemes are almost the same (fig. 3.1).

Due to the large number of time steps needed, the benefit of a constant system matrix becomes less important because at every time step still the right hand side of the matrix equation has to be updated. For example, one time step for the Adams–Bashforth and the Crank–Nicolson scheme took about 6 sec, whereas one time step for the fully Crank–Nicolson scheme took about 17 sec. For larger problems this difference will increase rapidly, but due to the larger number of time steps needed for a conditionally stable time integration scheme and because the algorithm for updating of the right hand side is hard to vectorize, in total at least comparable but likely larger computing times are needed for the conditionally stable time integration schemes. Therefore, in this study only unconditionally stable time integration schemes are employed.

4 Experimental method

4.1 Introduction

In this chapter a short description is given of the methods and materials used for the velocity measurements under steady and unsteady flow conditions in a 90–degree curved tube and the velocity measurements under steady flow conditions in a 3D–model of the carotid artery bifurcation. A one–component forward–scattering reference–beam laser Doppler technique was used to measure both axial and secondary velocities (sect. 4.2). Because of its lower viscosity, in case of unsteady flow a solution of zinciodide was used as measuring fluid instead of a mixture of oil and kerosine, which was used in case of steady flow (sect. 4.3). In section 4.4 the fluid circuit is described. In section 4.5 the acquisition and processing of the velocity data is discussed. There are several sources which give rise to errors in the velocity measurements. These error sources together with estimates of the influence of these errors on the velocity measurements are presented in section 4.6.

4.2 Laser Doppler anemometry

Laser Doppler anemometry is commonly used to measure fluid velocities. In contrast with other methods, like heat wire anemometry, with laser Doppler techniques fluid velocities are measured without disturbing the flow pattern itself. Drain (1981) gives an extensive description of the physical aspects of this method. In the experiments performed in this study a one–component forward–scattering reference–beam method was used (Drain, 1981). In short, one laser beam, generated by a 5mW He–Ne–laser (Spectra Physics, 120S), is splitted into two laser beams. To detect negative velocities the reference beam is shifted in frequency with frequency f_v, as compared to the frequency of the main beam, by using a Bragg cell unit (DISA, 55X29). The two laser beams intersect in a measuring volume with dimensions 400μm x 40μm x 40μm. Due to particles dissolved in the fluid (Lichrosorb, Si100, mean particle diameter 5μm) the laser light is scattered in the direction of a photodetector (DISA, 55L11) causing a Doppler shift f_d in the frequency of the main beam. This Doppler shift is linearly related to the fluid velocity component in the measuring volume parallel to the plane spanned by the reference and the main beam and perpendicular to the optical axis of the He–Ne–laser. Interference of the laser light of the reference beam and the main beam causes the intensity of the laser light on the photodetector to vary with frequency (f_v + f_d). The frequency signal of the photodetector is transferred into a voltage signal between 1V and 10 V, by using a shifter (DISA, 55N12) and a tracker (DISA, 55N21).

4.3 Zinciodide as measuring fluid

Velocity measurements in 3D–models require exact matching of the refraction indices of the fluid and of the perspex models (refraction index perspex 1.493). In a study by Bovendeerd et al. (1987) a mixture of oil and kerosine was successfully employed for velocity measurements under steady flow conditions in a 90–degree curved tube. In this study the oil mixture was also used for the steady flow analysis in a 3D–model of the carotid artery bifurcation (chapter 6). A disadvantage of the oil mixture is its high kinematic viscosity. Therefore, for unsteady velocity measurements high pump frequencies are required for matching of the Womersley parameter to the one in vivo, which was not possible with the conventional pumps available. Beside the high kinematic viscosity, the dependence of the oil mixture on temperature caused problems. In figure 4.1a the dependence of the kinematic viscosity on temperature is shown. The steady flow experiments were performed at 40 ^{o}C to lower the kinematic viscosity of the oil mixture and to eliminate the influence of ambient temperature variations. From figure 4.1a it is concluded that small variations in the temperature cause large variations in the kinematic viscosity, resulting in relative large changes in the Reynolds number. It should be kept in mind that electromagnetic flow rate measurements can not be used in combination with a mixture of oil and kerosine, because this mixture is a non–ionic fluid. For unsteady flow experiments, however, dynamic volume flow measurements are indispensable for correct adjustment of the cyclically varying Reynolds number.

Another fluid with a high variable refraction index is a solution of zinciodide, as used by Hendriks and Aviram (1981). Beside its much lower kinematic viscosity at a temperature of 25 ^{o}C and a refraction index equal to perspex, its dependence on temperature is less dramatic as for the mixture of oil and kerosine (fig. 4.1b). With a solution of zinciodide it is also possible to use electromagnetic flow probes to measure flow rates. If a zinciodide solution is used as measuring fluid, contact with oxygen needs to be avoided because otherwise oxidation will occur. Therefore, nitrogen gas was injected into the zinciodide reservoir. To eliminate the influence of ambient temperature variations, the zinciodide reservoir was immersed in water, which was kept at a constant temperature of 25 ^{o}C using a thermostat (Julabo V).

Besides, usage of a zinciodide solution requires special materials. Due to the fact that small portions of zinciodide dissolve in perspex, this material weakens and, as a consequence, crack formation may occur at places where internal stresses are high (stress corrosion). Therefore, the two halves of perspex used must be as free as possible of internal stresses. This can be achieved by annealing these parts in an oven for a couple of hours. Nevertheless, problems may still arise at screwed or clamped connections. Stainless steel and synthetic materials, like teflon and nylon, seem to be spared. Finally, a zinciodide solution is somewhat poisonous and rather aggressive, and, therefore, must be treated with care. Due to its high costs it can only be used in small amounts.

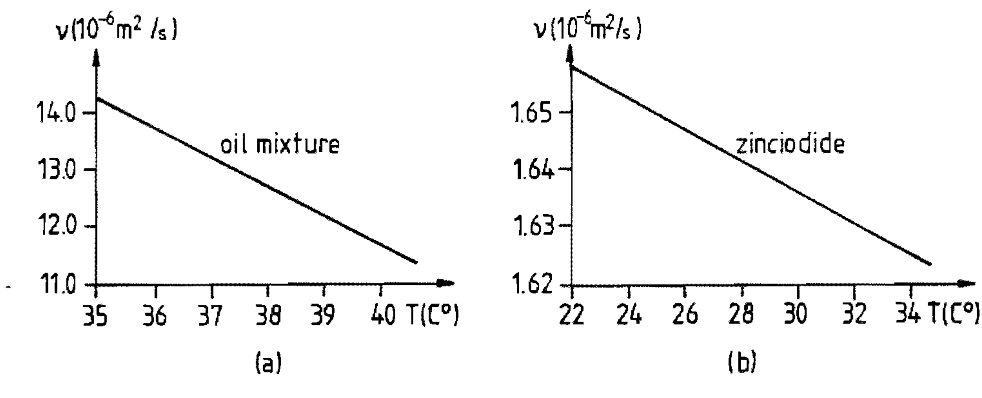

Figure 4.1: Dependence on temperature of the kinematic viscosity of a mixture of oil and kerosine (a) and a solution of zinciodide (b). Note differences in scaling.

4.4 Fluid circuit

The fluid circuit used for steady flow analysis in a 3D–model of a 90–degree bend and the carotid artery bifurcation has been described in detail before (Bovendeerd et al., 1987; Rindt et al., 1988). This fluid circuit was quite similar to the fluid circuit used for the unsteady velocity measurements in a 3D–model of a 90–degree curved tube. Figure 4.2 gives a schematic presentation of this fluid circuit. A gear pump was used for generation of the steady flow component (Verder, 114–1.ty–316). The unsteady flow component was generated by a special plunger pump (Vivitro Systems Incorporated). This pump is a piston–in–cylinder pump consisting of a low inertia electric motor (33VM82), a linear actuator (SP3891) and a standard pump head (SPH5891). The motor was driven by a servo power amplifier (SPA3891), which uses the piston position and the motor speed as feed back signals. A programmable waveform generator was used (WG5891) for driving the pump. The frequency of the waveforms generated is selectable at 8 levels and ranges from 30 to 200 cycles per minute with an accuracy of ±1%. The waveform generator also provides an output signal to facilitate synchronization to external instrumentation.

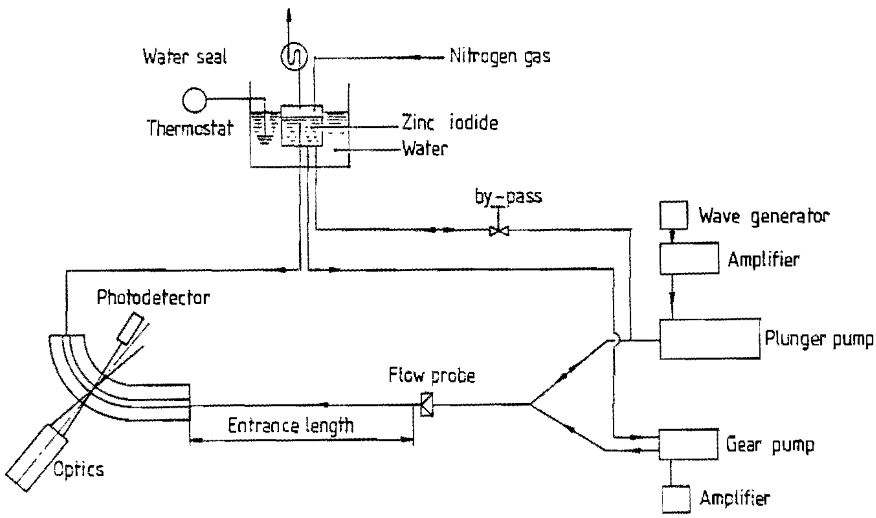

Figure 4.2: Fluid circuit for the unsteady flow experiments.

The standard pump head had a surface of 38.25 square centimeters. Using a zinciodide solution in combination with the 3D–model of the 90–degree curved tube described below, the piston displacement was about 0.75 mm for a Reynolds number varying between $-425<Re<425$ and a Womersley parameter of 5.5. This small piston displacement of about 2% of the maximal piston displacement resulted in unacceptable differences between the imposed and the measured waveforms of the flow rate. Therefore, a pump head was manufactured with a surface of 2.27 square centimeters, resulting in a piston displacement of about 30% of the maximal value. This value could even be increased by using a bypass in the fluid circuit. In figure 4.3 the generator wave, the piston velocity and the flow rate are presented as function of time for a maximal Reynolds number of 425 and a frequency of 0.5 Hz, using the small pump head. Irregularities in the piston velocity occur during the zero crossings. Probably, these irregularities are caused by an inadequate control loop. They become smaller for higher frequencies. The rather rough appearance of the flow wave is caused by the unfiltered recording of the electromagnetic flow rate signal and the finite accuracy of ±0.3 ml/s of the flow probes used (Skalar, Transflow 601).

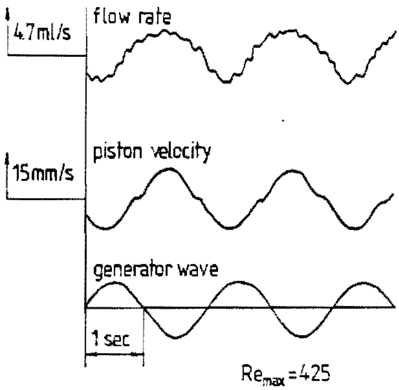

Figure 4.3: Generator wave, piston velocity and flow rate for the small pump head.

As connecting tubes between the various systems, wired tubes were used to avoid wave propagation and reflection phenomena. An analytical study and the observed zero phase lag between the imposed and measured flow rate confirmed that these phenomena did not occur. An entrance length of 0.4 m (50 diameters) was used to ensure that fluid flow was fully developed before it reached the measuring section.

The 3D–models consisted of two halves of perspex, split at the plane of symmetry, in which the 90–degree curved tube and the carotid artery bifurcation were machined out. In figure 4.4 these models are presented. The radius of the 90–degree curved tube was a=4 mm and the curvature ratio was δ=a/R=1/6. This curvature ratio was chosen because the entrance region of the internal carotid artery can be regarded as a curved tube with a curvature ratio of δ=1/6. The geometry of the carotid artery bifurcation was almost similar to the one described by Balasubramanian (1979), with the exception of the angle between the external and common carotid artery which, for manufacturing reasons, was 30° instead of 25°. The radius of the common carotid artery was equal to a=4 mm.

To adjust the correct Reynolds number for the unsteady flow measurements the electromagnetic flow rate signal of the flow probe was used. Adjustment of the correct Reynolds number for the steady flow measurements was performed by measurement of the maximal axial velocity in the main branch with the laser Doppler anemometer. To achieve a flow division ratio over the daughter branches of

50/50 in case of steady flow in the carotid artery bifurcation, long outstream tubes with the same diameter for both daughter branches were used. This flow division ratio was checked by numerical integration of the axial velocity field in the daughter branches.

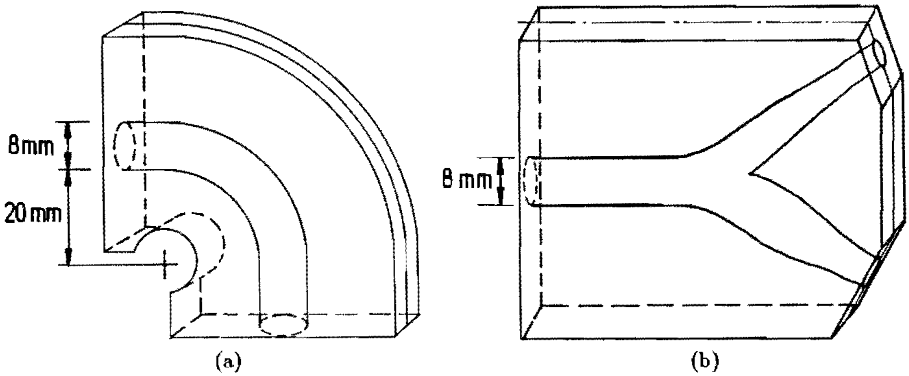

Figure 4.4: The perspex models of the 90–degree curved tube (a) and the carotid artery bifurcation (b).

4.5 Data acquisition and data processing

Data intake was performed by a measuring system consisting of a personal computer, a 4–channel signal processing unit and an interface. The voltage signal of the tracker, which is related to one component of the fluid velocity in the measuring volume, was fed to the signal processing unit. There, with a gain and offset, the input signal was adjusted between –5V and 5V and it was filtered to avoid aliasing. Next, the signal was fed to an AD–converter and stored on disk of a personal computer. The sample frequency in the unsteady flow experiments was dependent on the frequency of the unsteady flow component. Per period 50 samples were taken. The start of data intake was controlled by the keyboard in the steady flow case and by a trigger pulse in the unsteady flow case. This trigger pulse was generated by the wave generator of the plunger pump. After calibration of the measuring unit and the laser Doppler equipment, the data obtained were converted to physical units. Beside the mean values, 95%–confidence intervals based on a student–t distribution were calculated. Therefore, 10 samples were taken in case of steady flow with a sample frequency of 2 Hz, and 10 periods were measured in case of unsteady flow. Plot facilities were used for inspection of the intermediate experimental results.

For measurement of the axial velocity component and the secondary velocity component parallel to the plane of symmetry, the optical axis of the He–Ne–laser was put perpendicular to the plane of symmetry of the 3D–models used. By rotation of the plane spanned by the laser beams both velocity components could be obtained. For measurement of the secondary velocity component perpendicular to the plane of symmetry the optical axis had to be parallel to the plane of symmetry and the plane spanned by the laser beams had to be perpendicular to the plane of symmetry. Problem with this kind of measurements is that total reflection at the plane of symmetry may occur of one of the laser beams due to an air film between the two halves of perspex. Therefore, in case of the steady and unsteady flow experiments in a 90–degree bend, a perspex model was used which was split along the axis of the tube and perpendicular to the plane of symmetry. In case of the steady velocity measurements in a 3D–model of the carotid artery bifurcation, reflection at the plane of symmetry was avoided by a film of oil and kerosine between the two halves of perspex.

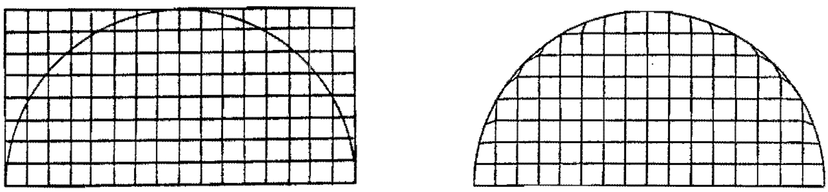

(a) (b)

Figure 4.5: Measuring grid (a) and finite element mesh (b).

Three stepper motors were used to traverse the model in three independent directions, through which positioning of the measuring volume at various sites in the model was possible. Due to the step size, positioning of the measuring volume occurred with an accuracy of $\pm 3 \mu m$, $\pm 8 \mu m$ and $\pm 8 \mu m$ in x–, y– and z–direction, respectively. Detailed analysis of the axial and secondary velocity distributions was performed at 5 levels in the 90–degree curved tube (chap. 5) and at 6 levels in the carotid artery bifurcation (chap. 6). At each level the measuring volume was traversed according to a rectangular grid (fig. 4.5a). Independently, the axial velocity component and both secondary velocity components were measured in each grid point. Afterwards, for presentation purposes, the rectangular measuring grid was transformed to a finite element mesh as depicted in figure 4.5b. The velocities at the wall were presumed to be zero according to the no–slip boundary condition.

Then, using post–processing software (SDRC, Sepran), axial and secondary flow were presented by axial isovelocity lines and secondary velocity vectors, respectively. Using linear interpolation also presentation of axial or secondary velocity profiles at arbitrary positions in the 3D–models was performed.

4.6 Error estimates

Several kind of error sources result in detection errors of the fluid velocities. First, errors result from small variations in the fluid velocity due to small variations in the imposed flow rate and the limited electronic detection accuracy of the frequency of the photodetector signal. For unsteady flow experiments also frequency instabilities of the plunger pump result in detection errors. All these errors can be estimated by calculation of the 95%–confidence intervals, which were found to be less than 0.5% of the maximal axial velocity for the steady flow case and less than 1% for the unsteady flow case.

Errors also result from positioning failures of the measuring volume due to localization errors of a starting point and the finite accuracy of the traversing system. For measurements performed in a plane this may lead to measurements outside the plane originally defined. In straight tubes the velocity gradients in axial direction are likely to be small, and hence errors caused by the measurements outside the plane may be neglected. However, in curved tubes axial and radial directions continuously change and, therefore, positioning of the measuring volume outside the plane causes detection of the wrong velocity component. These errors can be observed as errors resulting from failures in the adjustment of the correct measuring angles of the optics, which will be discussed below. Positioning errors of the measuring volume in the plane are estimated to be ±0.1 mm due to localization errors of a starting point and ±0.1 mm due to the finite accuracy of the traversing system. Detection errors of the velocity caused by these positioning errors are estimated to be 5% of the local velocity.

Besides, errors are caused by failures in the adjustment of the correct angles. The measuring direction of the laser Doppler anemometer used in this study is parallel to the plane spanned by the reference and the main beam and perpendicular to the optical axis. In figure 4.6 this direction is denoted by line m and deviates from the planned direction with the angles $\Delta\varphi$ and $\Delta\psi$ ($\Delta\varphi$, $\Delta\psi$ <<1). The measured velocity component v_m is a function of v_x,v_y and v_z with v_x the velocity component which was planned to be measured and v_y and v_z the velocity components perpendicular to v_x. Errors in the adjustment of the correct angles result from several sources, like errors in the localization of the measuring plane ($\pm 0.5^\circ$ for the carotid artery bifurcation and $\pm 1.0^\circ$ for the 90–degree curved tube), errors in the positioning of the 3D–model with respect to the optics ($\pm 0.5^\circ$) and errors caused by traversing failures as described above ($\pm 0.5^\circ$ for the 90–degree curved tube). Therefore, the total error in the adjustment of the correct angles is estimated to be $\pm 1.25^\circ$ for the 90–degree curved tube and $\pm 0.85^\circ$ for the carotid artery bifurcation. For the configurations used in this study the maximal secondary velocities are about 25% of the maximal axial velocities. Therefore, it is reasonable to presume that the largest absolute errors occur in the detection of the secondary flow field. For the 90–degree curved tube these errors are estimated to be 2% of the local axial velocity, whereas for the carotid artery bifurcation these errors are estimated to be 1.25% of the local axial velocity. However, in regions with low axial velocities, errors in the detection of axial velocities due to the secondary velocity components can not be neglected.

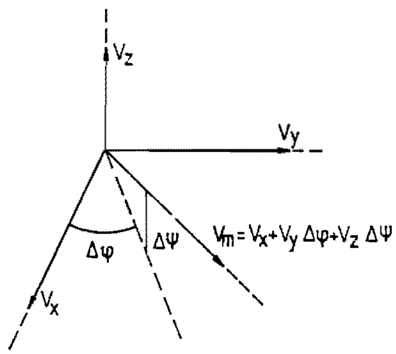

Figure 4.6: Planned measuring direction (x–direction) and real measuring direction (m–direction).

Next, errors in the determination of the angle between the reference and the main beam cause detection errors of the velocity, which are estimated to be ±0.5%. The size of the measuring volume (400μm x 40μm x 40μm) with regard to the size of the 3D–models used (8 mm), also causes presumably small detection errors of the velocity, dependent on the velocity gradients. The highest influence of these errors is expected near the side walls of the models, where the velocity gradients are mostly large.

Finally, errors result from adjustment failures of the correct Reynolds number and Womersley parameter. Errors in the Reynolds number are caused by inaccuracies in the values of the flow rate and the kinematic viscosity and are estimated to be ±5% for the steady flow experiments and ±10% for the unsteady flow experiments. The large confidence interval for the steady flow case is almost completely determined by the high dependence of the kinematic viscosity of the oil mixture on temperature, as the temperature variations in the experiments are of the order of ±0.5 ^{o}C. The large confidence interval in case of unsteady flow is possibly caused by inadequate adjustment of the flow rate. Here the influence of the unsteady flow component on the 'steady' flow component was not taken into account.Finally, errors in the adjustment of the Womersley parameter are estimated to be ±1%.

It may be concluded that the largest errors occur due to positioning failures of the measuring volume in the measuring plane. However, it should be kept in mind that these errors hardly influence the flow phenomena observed but only cause shifts in, for example, the axial velocity contours. On the other hand, the errors resulting from incorrect adjustment of the measuring angles do influence the flow phenomena observed, because also parts of other velocity components are measured.

5 Steady and unsteady entrance flow in a 90–degree curved tube

5.1 Introduction

In this chapter the results of steady and unsteady velocity calculations in a 90–degree curved tube are presented. These velocity calculations are performed for various frequency parameters and flow wave forms. For one set of parameters a detailed comparison is made with the results obtained from laser Doppler velocity measurements. A comparison with data available in literature is difficult to perform because only a small range of parameters, describing unsteady entrance flow in curved tubes, is studied. Most investigators are dealing with fully developed flows or entrance flows under totally different flow conditions.

Olson (1971) studied steady flow in a symmetrical three–dimensional bifurcation using hot wire anemometry, and compared the results with data obtained from velocity measurements performed in curved tubes. Olson concluded that the flow phenomena occurring in the daughter branches of such a symmetrical bifurcation are highly determined by curvature effects. In spite of the fact that the geometry of the carotid artery bifurcation is highly asymmetric, also here the influence of curvature effects on the flow phenomena occurring in the daughter branches of this bifurcation, are presumed to play an important role. Therefore, steady and unsteady entrance flow in a 90–degree curved tube was investigated to gain more insight into the complicated flow field in the carotid artery bifurcation. Besides, because of its rather simple geometry, numerical modeling of fluid flow in a curved tube is relatively simple, as compared to modeling of fluid flow in asymmetrical bifurcations.

In analytical studies the Navier–Stokes and continuity equations are often presented in a toroidal coordinate system. It then appears that for loosely coiled pipes (low curvature ratios) the Dean number is more appropriate to characterize steady flow than the Reynolds number (Berger et al., 1983). This number, in combination with the curvature ratio or the Reynolds number, is also commonly used for characterization of the flow phenomena occurring in curved tubes with higher curvature ratios. The Dean number is defined as $\kappa=\delta^{1/2}\mathrm{Re}$ with Re the Reynolds number and δ the curvature ratio. This latter number is defined as $\delta=a/R$ with a the radius and R the curvature radius of the axis of the tube. The Dean number can be interpreted as the ratio of the square root of the product of centrifugal and inertia forces to the viscous forces (Berger et al., 1983). Besides, in analytical studies on fully developed unsteady flows in curved pipes with low curvature ratios the Womersley parameter and the secondary Reynolds number are often used to characterize the influence of the unsteady flow component on the flow phenomena occurring. The Womersley parameter is defined as $\alpha = a(\omega/\nu)^{1/2}$ and can be interpreted as the ratio of the radius of the tube to the penetration depth of the viscous forces (Schlichting, 1979). In these analytical studies secondary flow is found to be governed by the secondary Reynolds number defined as $R_s = \delta U^2/(\nu\omega)$, with U the amplitude of the mean axial velocity variation. In the present study we will focus on the Reynolds number as function of time and the Womersley parameter in combination with the curvature ratio. In the definition of the Reynolds number the mean axial velocity is used as characteristic velocity.

Analytical studies on fully developed oscillating flows in curved tubes reveal that for $\alpha << 1$ a Dean type secondary flow and for $\alpha >> 1$ a Lyne type secondary flow occurs (Lyne, 1970; Lin and Tarbell, 1980), with secondary flow being defined as the flow field perpendicular to the axis of the curved tube. For a Dean type secondary flow, the secondary velocities near the plane of symmetry are directed from the inner wall towards the outer wall due to the dominating centrifugal forces in this region. These centrifugal forces induce a positive pressure gradient in that direction. Near the side wall, where due to viscosity the axial velocities and consequently the centrifugal forces are low, the pressure forces will dominate the centrifugal forces. Hence, near the side wall a circumferential inward motion of the fluid occurs. These secondary velocities cause a so-called Dean vortex at each side of the plane of symmetry (fig. 5.1a). For high frequencies ($\alpha >> 1$) the viscous effects are restricted to a small layer near the side wall and at each side of the plane of symmetry, two vortices appear. The first one has the same circulation direction as the Dean vortex but is only present close to the side wall, while in the central region

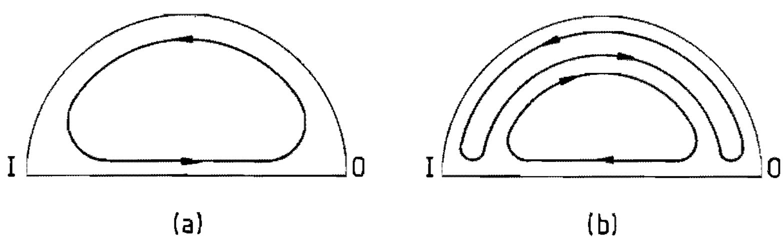

Figure 5.1: Schematical presentation of the Dean type (a) and Lyne type (b) secondary flow fields (I: inner wall, O: outer wall).

a second vortex develops with an opposite circulation direction, resulting in a Lyne type secondary flow (fig. 5.1b). Munson (1975) visualized fully developed oscillating flow in a curved tube (δ=1/14) for Womersley parameters ranging from 0 to 32. According to his observations a Lyne type secondary flow field occurs for α>13.

Fully developed flows in curved tubes have been studied theoretically and/or experimentally by many investigators (Lyne, 1970; Zalosh and Nelson, 1973; Bertelsen, 1975; Munson, 1975; Smith, 1975; Lin and Tarbell, 1980; Mullin and Greated, 1980; Berger et al., 1983). In recent studies on this subject (Chang and Tarbell, 1988; Hamakiotes and Berger, 1988) the system of equations was solved by some kind of finite difference method. Singh et al. (1978) performed an analytical study of unsteady entrance flow in a curved tube ($\delta=O(10^{-1})$) using a uniform inlet profile. Mullin and Greated (1980) used laser Doppler anemometry for their velocity measurements in a curved tube with a curvature ratio of 1/7. As inlet condition an oscillating fully developed pipe flow was employed. The measurements were performed at a Womersley parameter of 0.99 and 4.36, while the peak Dean number ranged from 5.8 to 64.2. Chandran et al. (1979) performed laser Doppler velocity measurements for a sinusoidally varying flow rate in a curved tube with a curvature ratio of 1/10. The time–averaged Dean number was equal to 322 and the Womersley parameter was equal to 21.9. Chandran and Yearwood (1981) performed the same sort of study for a physiologically varying flow rate at a time–averaged Dean number of 320 and a Womersley parameter of 20.7. Talbot and Gong (1983) performed laser Doppler experiments in a curved tube with a curvature ratio of 1/20 and 1/7. Two situations were investigated for which the characteristic flow parameters were $80<\kappa<160$, $\alpha=8$ and $0<\kappa<744$, $\alpha=12.5$, respectively. Perktold et al. (1987) analyzed pulsatile blood flow in a carotid siphon model, composed of several curved segments. They used the finite element method to solve the time dependent, three–dimensional Navier–Stokes and continuity equations under physiological flow conditions.

In this chapter unsteady entrance flow in a 90–degree curved tube with a curvature ratio of 1/6 is analyzed for oscillating, pulsating and physiological flow rates. As a preparatory study in section 5.2 steady flow at a Reynolds number of 700 is investigated. A qualitative and quantitative comparison of the calculated velocity field is made with that obtained from laser Doppler velocity measurements of Bovendeerd et al. (1987).

In section 5.3 the results of a velocity calculation are shown for a pulsating flow rate. The Reynolds number varied sinusoidally between 200 and 800, corresponding to the diastolic and systolic Reynolds numbers in the carotid artery bifurcation, respectively. The Womersley parameter was equal to 7.8, about twice the in vivo value. This value was chosen to match the sinusoidal flow rate variation with the physiological flow rate variation in the systolic phase of the heart cycle. For this particular case a detailed description of the axial and secondary flow fields is given as function of time. Afterwards, a qualitative and quantitative comparison with laser Doppler velocity measurements is made.

The influence of the frequency parameter on both axial and secondary flow is described in section 5.4, where the results are presented of velocity calculations under pulsatile flow conditions at various values of the Womersley parameter. Besides, in this section the results of a velocity calculation of fluid flow at a physiological flow rate are shown, elucidating the influence of the wave form on the flow phenomena occurring. Also in this section the influence of the steady flow component is studied. Finally, a qualitative and quantitative comparison between the various flow situations is performed and a comparison is made with laser Doppler velocity measurements.

In section 5.5 the results are discussed and compared to data available in literature.

5.2 Steady entrance flow

5.2.1 Introduction

In a study performed by van de Vosse et al. (1989) the results of finite element calculations of steady flow in a 90–degree curved tube with a curvature ratio of 1/6 are presented for Reynolds numbers up to 500. Application of higher Reynolds numbers caused oscillations in the predicted velocity field, probably due to bifurcation of the solution in this range of Reynolds numbers or a too coarse element division. To avoid these problems, in this study a finer element division is employed and iteration towards higher Reynolds numbers was achieved by solving the unsteady Navier–Stokes problem.

Figure 5.2 shows the element division used, consisting of 20 elements in axial direction and 30 elements per cross–section. The lengths of the inlet and outlet sections are both 6 times the radius of the curved tube. Flow at the inlet was supposed to be fully developed, which means a parabolic axial velocity profile and zero secondary velocities. The velocities at the wall were presumed to be zero, according to the no–slip condition. At the outlet the normal and both tangential stresses were set to zero, while in the plane of symmetry both tangential stresses and the normal velocity component were put to zero. For the mesh as shown in figure 5.2, one iteration on an Alliant–fx/4 (2 processors) took about 30 minutes of computing time.

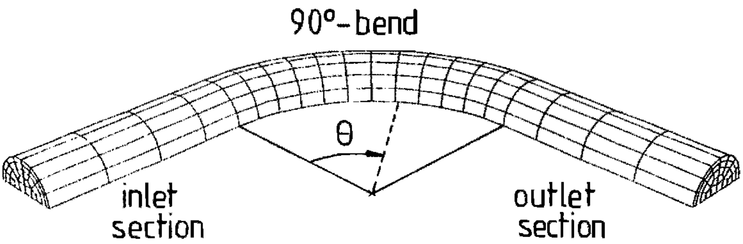

Figure 5.2: The element division for the 90—degree curved tube.

In figure 5.3 the Reynolds number is presented as function of the iteration number. For the iteration numbers 1 to 13 an unsteady velocity calculation was performed, using an Euler–implicit (θ=1) time integration scheme. In the first iteration a zero velocity field was used as initial condition. The Reynolds number was varied by adjusting the maximal axial velocity at the inlet of the curved tube. Because of convergence problems, at the end of the calculation procedure the steady Navier–Stokes problem was solved. To reach convergence another 4 iterations were needed. The maximal difference between the velocity components of the final 2 iterations was of $O(10^{-6})$.

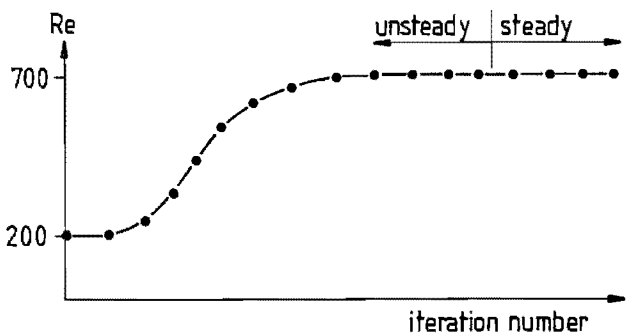

Figure 5.3: The Reynolds number as function of the iteration number.

5.2.2 Description of the flow field

Figure 5.4 shows the development of axial and secondary flow by axial isovelocity lines, lines often denoted as axial velocity contours, and secondary velocity vectors. The presentation sites are $\theta=0^{o}$, 22.5^{o}, 45^{o}, 67.5^{o} and 90^{o} (fig. 5.2). Axial contour level 0 corresponds to zero axial velocity and level 10 to the maximal axial velocity (U_{max}) at the inlet of the curved tube. The secondary velocities at $\theta=0^{o}$ are scaled up 3 times with respect to the secondary velocities at the other cross–sectional planes.

At the entrance of the curved tube ($\theta=0^{o}$) the axial velocity maximum is slightly shifted towards the inner wall. Secondary flow is completely directed from the outer bend towards the inner bend, pointing at upstream influences of the curved tube.

At $\theta=22.5^{o}$ the maximum of axial velocity is shifted towards the outer wall, due to centrifugal forces. Near the plane of symmetry the secondary velocities are directed towards the outer bend, whereas these velocities are directed towards the inner bend near the side wall of the curved tube. The secondary flow field resembles a Dean type vortex. The center of the vortex is positioned near the side wall at the center line of the cross–sectional plane.

Halfway the curved tube, at $\theta=45^{o}$, as a consequence of secondary flow the shift of the maximum of axial velocity towards the outer wall continues. Besides, some of the axial velocity contours become C–shaped because fluid particles with high axial velocities situated near the outer wall, are transported towards the inner wall by circumferential secondary flow. The center of the secondary vortex is shifted towards the inner bend and, at this position in the curved tube, the highest secondary velocities are observed near the side wall.

At $\theta=67.5^{o}$ the curvature of the axial isovelocity lines has intensified and the maximum of axial velocity has shifted further towards the outer bend. The secondary velocities at this position are much lower as compared with the secondary velocities halfway the curved tube, especially near the plane of symmetry. The secondary vortex at this level has developed a 'tail', through which fluid particles near the center of the tube are transported in the direction of the side wall. This 'tail'–formation is possibly due to the fact that the fluid particles with relatively low axial and secondary velocities, situated near the center of the tube, are not able to penetrate into the region with high axial velocities near the outer wall. The

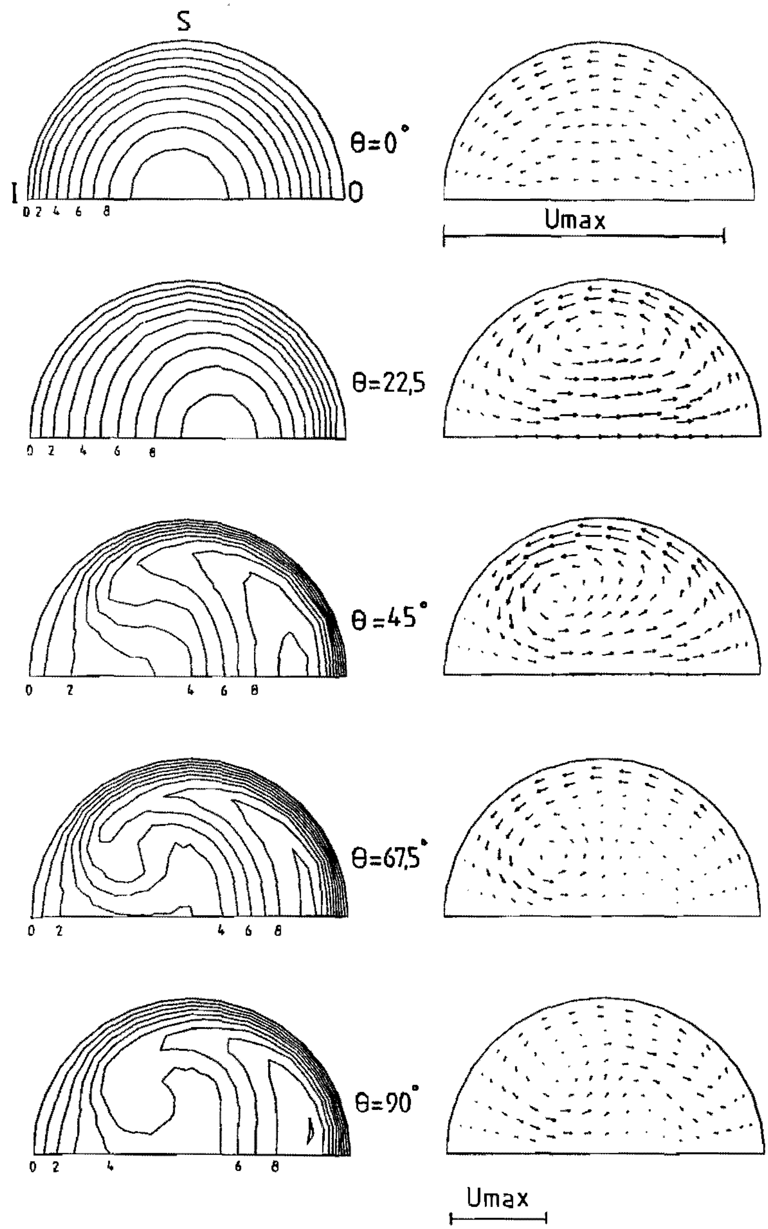

Figure 5.4: Axial and secondary flow for the steady flow case (I: inner wall, O: outer wall, S: side wall).

center of the vortex has shifted somewhat towards the plane of symmetry.

At θ=90° the same sort of phenomena occur as observed at θ=67.5°. At this position a further decrease of the secondary velocities is observed, possibly due to upstream influences of the straight outlet section.

5.2.3 Qualitative comparison with experiments

Bovendeerd et al. (1987) performed an experimental study of steady entrance flow in a 90–degree curved tube, with a curvature ratio of 1/6, at a Reynolds number of 700. They used a laser Doppler anemometer to measure axial and secondary velocities at 7 positions in the curved tube (θ=0°, 4.6°, 11.7°, 23.4°, 39.8°, 58.8° and 81.9°). A qualitative comparison with their measurements is performed by comparing the axial velocity profiles in the plane of symmetry. In figure 5.5 these axial velocity profiles are presented for both the measurements and the calculations. There is an excellent agreement between the experimental and numerical data. In the numerical case the axial velocity plateau at θ=58.5° is somewhat less developed.

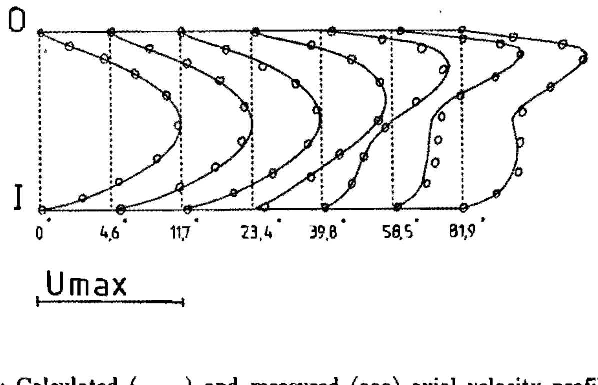

Figure 5.5: Calculated (——) and measured (ooo) axial velocity profiles in the plane of symmetry (I: inner wall, O: outer wall).

For a qualitative comparison between the calculated and measured secondary flow field, in figure 5.6 secondary flow at θ=23.4° and 58.5° is presented by velocity profiles of the component parallel to the plane of symmetry (upper half) and the component perpendicular to the plane of symmetry (bottom half). Here again a relatively good agreement exists between the experimental and numerical results. The largest differences are found near the side wall at θ=23.4°, where the calculated secondary velocities parallel to the plane of symmetry are higher than the measured ones. Possibly, measuring errors due to the dimensions of the measuring volume contribute to this discrepancy.

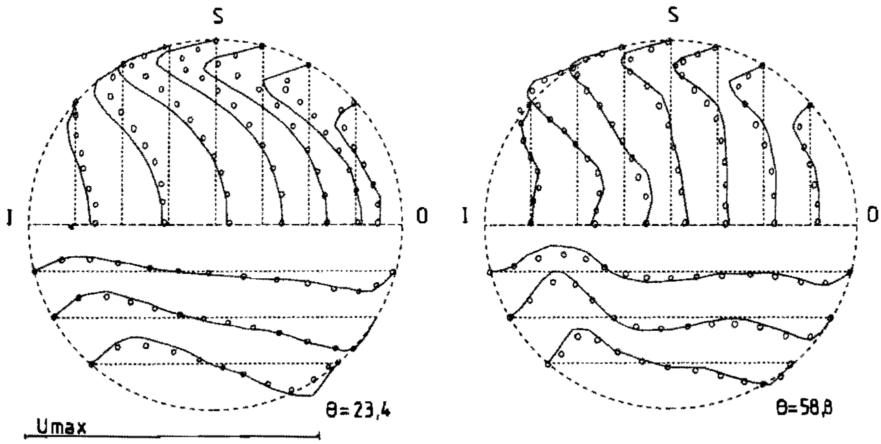

Figure 5.6: Calculated (——) and measured (ooo) secondary velocity profiles (I: inner wall, O: outer wall, S: side wall).

5.2.4 Quantitative comparison with experiments

A quantitative comparison of the numerical results of axial flow with those obtained by Bovendeerd et al. (1987) is performed by the dimensionless first moment of axial flow, defined as (Olson and Snyder, 1985):

$$\langle X/a\rangle = \frac{1/a \int_A u_{ax}\, x\, dA}{\int_A u_{ax}\, dA} \tag{5.1}$$

with u_{ax} the axial velocity component, A the surface of the cross–sectional plane, x the distance parallel to the plane of symmetry towards the center line of the cross–sectional plane and a the radius of the tube (fig. 5.7). A positive value of this quantity indicates a shift towards the outer bend.

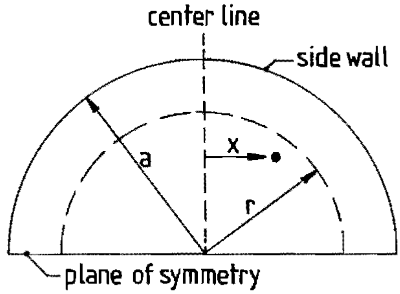

Figure 5.7: Definition of x—coordinate and semicircle in a cross—sectional plane of the bend.

In table 5.8 the first moment of axial flow for both the measurements and the calculations is presented as function of the axial position. The 95%—confidence intervals, based upon errors in the adjustment of the laser Doppler equipment, are estimated to be ±0.02. Errors in the adjustment of the correct Reynolds number are not taken into account. There is a rather good agreement between the experimental and numerical data. The largest difference occurs at θ=23.4°. At the first three positions the axial flow field is slightly shifted towards the inner bend as a consequence of upstream influences. The largest shift towards the outer bend occurs about halfway the curved tube.

θ	0°	4.6°	11.7°	23.4°	39.8°	58.5°	81.9°
exp	−0.03	−0.03	−0.03	0.04	0.16	0.13	0.12
num	−0.03	−0.04	−0.02	0.07	0.16	0.14	0.11

Table 5.8: First moment of axial flow for the measurements (±0.02) and the calculations.

The secondary flow field is quantified by its dimensionless axial vorticity ξ, defined as (Olson and Snyder, 1985):

$$\xi = \frac{a}{AU_{mn}} \int_S u_{tg} ds \qquad (5.2)$$

with S the boundary of a region with surface A, u_{tg} the tangential secondary velocity at S, a the radius of the tube and U_{mn} the mean axial velocity. A positive value of ξ indicates a counter clockwise vortex. When S is chosen along the plane of symmetry and the side wall of the curved tube (fig. 5.7), the vorticity ξ_c of the central core is found. Because of the no–slip condition at the wall, in fact ξ_c quantifies the secondary velocities in the plane of symmetry. In table 5.9 ξ_c is presented as function of the position in the curved tube for both the calculations and the experiments. The 95%–confidence intervals are estimated to be ±0.02. The agreement between the numerical and experimental data is good. The highest secondary velocities in the plane of symmetry are found at θ=23.4°. At θ=0° a negative value is found due to upstream influences of the curved tube, causing secondary velocities in the plane of symmetry directed towards the inner bend.

θ	0°	4.6°	11.7°	23.4°	39.8°	58.5°	81.9°
exp	−0.06	0.04	0.18	0.32	0.24	0.09	0.05
num	−0.03	0.07	0.20	0.34	0.26	0.08	0.01

Table 5.9: Axial vorticity of the central core for the measurements (±0.02) and the calculations.

In table 5.10 the maximum of axial vorticity is presented. This quantity ξ_m was calculated along a path S consisting of a semicircle in the cross–sectional plane, which was closed along the plane of symmetry (fig. 5.7). The 95%–confidence intervals for this quantity are estimated to be ±0.05. These relatively large intervals are due to positioning errors of the measuring volume near the side wall, where the secondary velocity gradients may be large. In spite of these large confidence intervals the agreement between the experimental and numerical data is bad. This discrepancy is caused by the lower tangential velocities near the side wall in the experimental case. In general, it is seen from figure 5.6 that close to the side wall the experimental values deviate from the numerical ones, while in the central region the agreement between both values is fair. Possibly, the finite dimensions of the measuring volume are more dominant than suggested in chapter 4, but an adequate reason for this discrepancy is not yet known. The maximal value of ξ_m is found at θ=39.8° for both the measurements and the calculations. Further downstream in the curved tube this value decreases rapidly.

θ	0°	4.6°	11.7°	23.4°	39.8°	58.5°	81.9°
exp	−0.04	0.11	0.31	0.57	0.64	0.26	0.13
num	−0.07	0.24	0.54	0.98	1.06	0.59	0.25

Table 5.10: Maximal axial vorticity for the measurements (±0.05) and the calculations.

5.3 Unsteady entrance flow

5.3.1 Introduction

In this section a detailed description of unsteady entrance flow in a 90–degree curved tube at a particular set of parameters is given. The flow rate consisted of a sinusoidally varying unsteady flow component ($-300<Re<300$) superimposed on a steady flow component ($Re=500$). With a curvature ratio of 1/6 this yields a Dean number varying between 82 and 327. The Womersley parameter was equal to 7.8.

For the finite element calculation, the element division as depicted in figure 5.2 was used. The boundary conditions were the same as used for the steady flow analysis, i.e. zero velocity components at the wall, zero normal and tangential stresses at the outlet of the tube and zero tangential stress components and a zero normal velocity component in the plane of symmetry. At the inlet of the tube both tangential velocity components were set equal to zero, whereas the normal velocity component described an unsteady fully developed axial flow field for which analytical solutions are available (Schlichting, 1979). From velocity calculations in a two–dimensional model of the carotid artery bifurcation (Rindt et al., 1987), it appeared that 20 time steps per period were sufficient to achieve an accurate solution. In this study one period consisted of 24 time steps. A zero velocity field was used as initial condition. To damp numerical errors induced by this initial condition, first an Euler–implicit time integration scheme was applied for 3/4 of a period. Hereafter, a Crank–Nicolson time integration scheme was employed until the maximal difference between the velocity components of the solution at the same time intervals of two successive periods was of $O(10^{-2})$. For the reference flow case treated here, 3 periods were needed to reach this goal.

In figure 5.11 the Reynolds number is presented as function of time and the time intervals are indicated at which the results are reported. Time interval t=0 corresponds to mean flow rate in the acceleration phase, t=1/4T to maximal flow rate, t=1/2T to mean flow rate in the deceleration phase and t=3/4T to minimal flow rate.

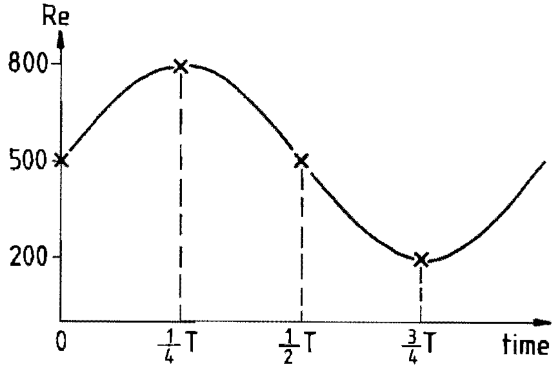

Figure 5.11: Reynolds number as function of time and the time intervals of presentation.

5.3.2 Description of the flow field

In figure 5.12 the results of axial and secondary flow at 5 axial positions in the curved tube ($\theta=0^{\circ}$, 22.5°, 45°, 67.5° and 90°) are shown. Axial flow is presented by axial isovelocity lines and secondary flow is visualized by means of velocity vectors. Contour level 0 corresponds to zero axial velocity and the difference in axial velocity between two successive levels is equal to 0.32 times the mean axial velocity at t=0 (U_{mn}). The secondary velocities at $\theta=0^{\circ}$ are scaled up three times, as compared to the secondary velocities at the other cross–sectional planes.

At $\theta=0^{\circ}$ (fig. 5.12a) the axial velocity contours at t=1/2T and 3/4T are almost concentrical circles. At t=0 and 1/4T the maximum of axial velocity is slightly shifted towards the inner bend of the curved tube, resulting in larger axial velocity gradients at the inner wall, as compared to those at the outer wall. The secondary velocities are completely directed from the outer wall towards the inner wall, pointing at upstream influences of the curved tube. These secondary velocities are about equal halfway the acceleration and deceleration phase. They are almost zero at minimal flow rate. At maximal flow rate oscillations are observed in the secondary flow field, possibly due to numerical failures as a consequence of a too coarse element division in the axial direction or a too short entrance length.

At θ=22.5° (fig. 5.12b) the secondary velocities near the plane of symmetry are directed towards the outer bend, as a consequence of centrifugal forces, whereas near the side wall of the curved tube these secondary velocities are directed towards the inner bend, resulting in a Dean type secondary flow field. For the total period of time the center of this secondary vortex is situated near the center line of the cross–sectional plane. The secondary velocities at t=1/4T and 1/2T are about equal, as well as the secondary velocities at t=3/4T and t=0. At minimal flow rate a region with low secondary velocities is found near the inner bend. As a consequence of secondary flow a shift of the maximum of axial velocity towards the outer bend is observed for the whole period of time. This shift is maximal at minimal flow rate (t=3/4T). At this time interval a region with negative axial velocities is observed at the inner bend. The largest axial velocity gradients are found at the outer wall at maximal flow rate (t=1/4T)

The highest secondary velocities throughout the curved tube occur at θ=45° (fig. 5.12c) at peak flow rate. Still, the secondary velocities are directed from the inner wall towards the outer wall near the plane of symmetry and circumferentially back near the side wall. The center of the vortex is situated near the center line of the cross–sectional plane for t=0 and it is slightly shifted towards the inner wall for t=1/4T, 1/2T and 3/4T, describing some kind of circle. In the deceleration phase and at minimal flow rate a 'tail' in the secondary flow field develops, through which the secondary velocities in the central region of the tube are no longer parallel to the plane of symmetry but slightly directed towards the side wall. Possibly, this 'tail'–formation is due to the relatively large axial velocity gradients in the central region. The shift of the axial isovelocity lines towards the outer wall continues, as compared to the shift at θ=22.5°, resulting in large axial velocity gradients at the outer wall. The largest shift is found at t=3/4T but, due to the smallest flow rate at this time interval, the axial velocity gradients are relatively small. At all time intervals C–shaped axial velocity contours are observed, which develop in the deceleration phase and become less pronounced in the acceleration phase. These C–shaped axial velocity contours are caused by secondary flow, through which fluid particles with high axial velocities situated at the outer bend are injected at the inner bend. Halfway the deceleration phase, at t=1/2T, a region with negative axial velocities is observed near the inner wall. At minimal flow rate (t=3/4T) also a region with reversed axial flow is found in the central region of the tube. At t=0 large regions occur with hardly varying axial velocities, pointing to the formation of axial velocity plateaus.

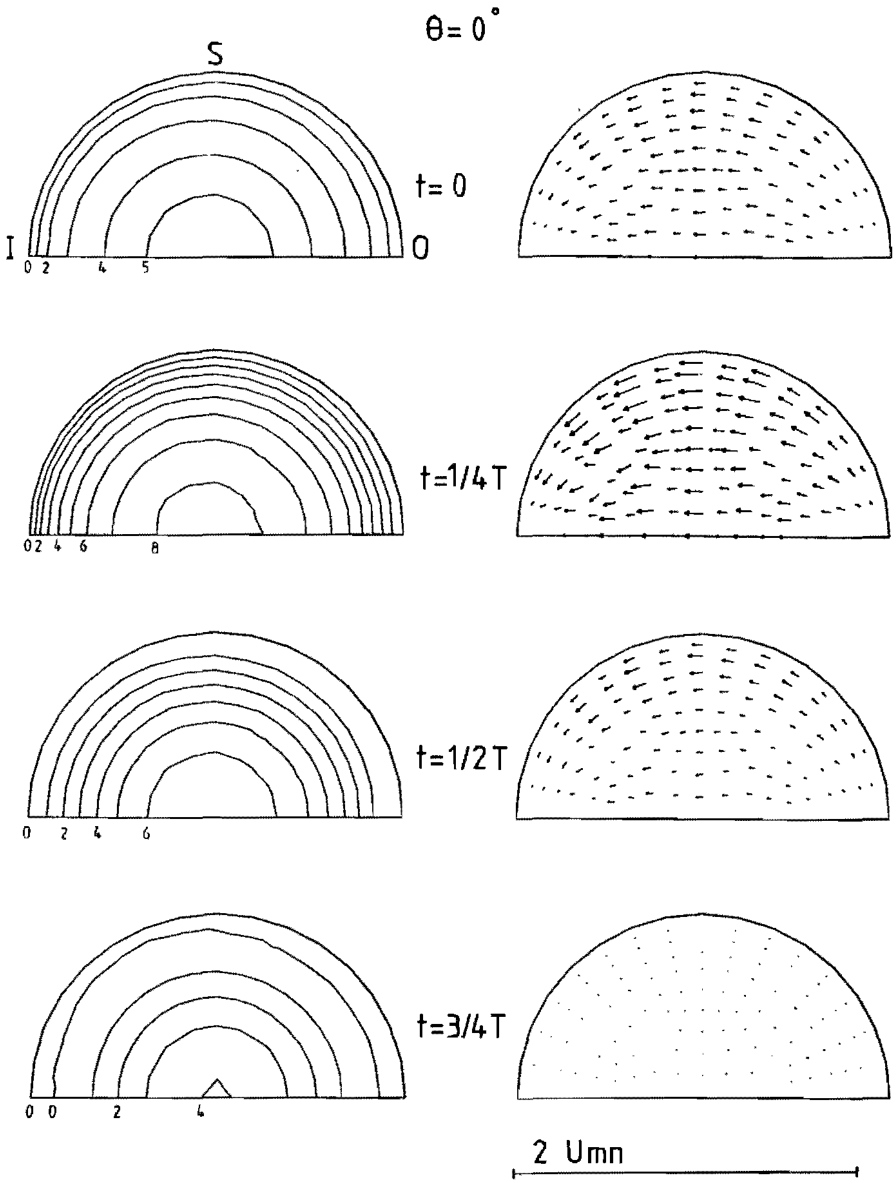

Figure 5.12a: Axial and secondary flow for the reference flow case at $\theta=0^{\circ}$ (I: inner wall, O: outer wall, S: side wall, U_{mn}: time–averaged mean axial velocity).

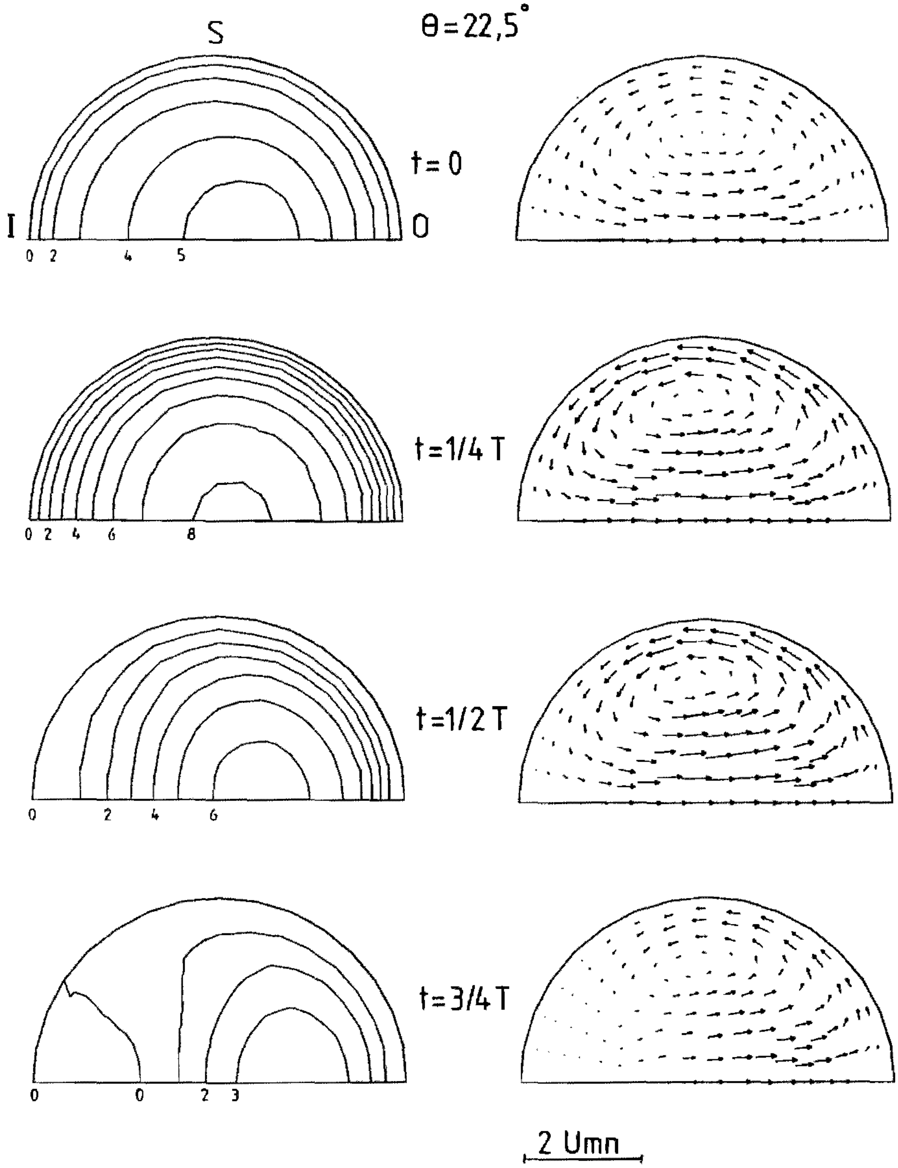

Figure 5.12b: Axial and secondary flow for the reference flow case at θ=22.5°.

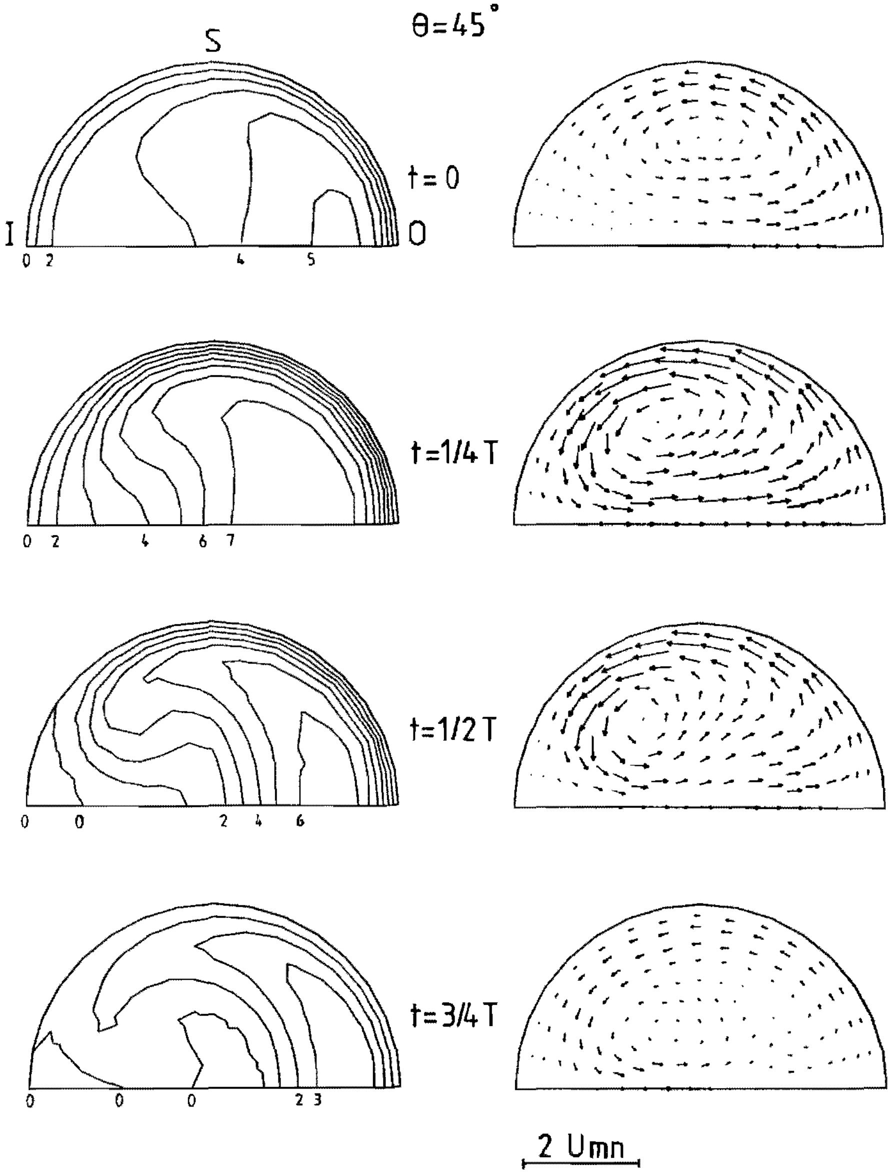

Figure 5.12c: Axial and secondary flow for the reference flow case at θ=45$^{\text{o}}$.

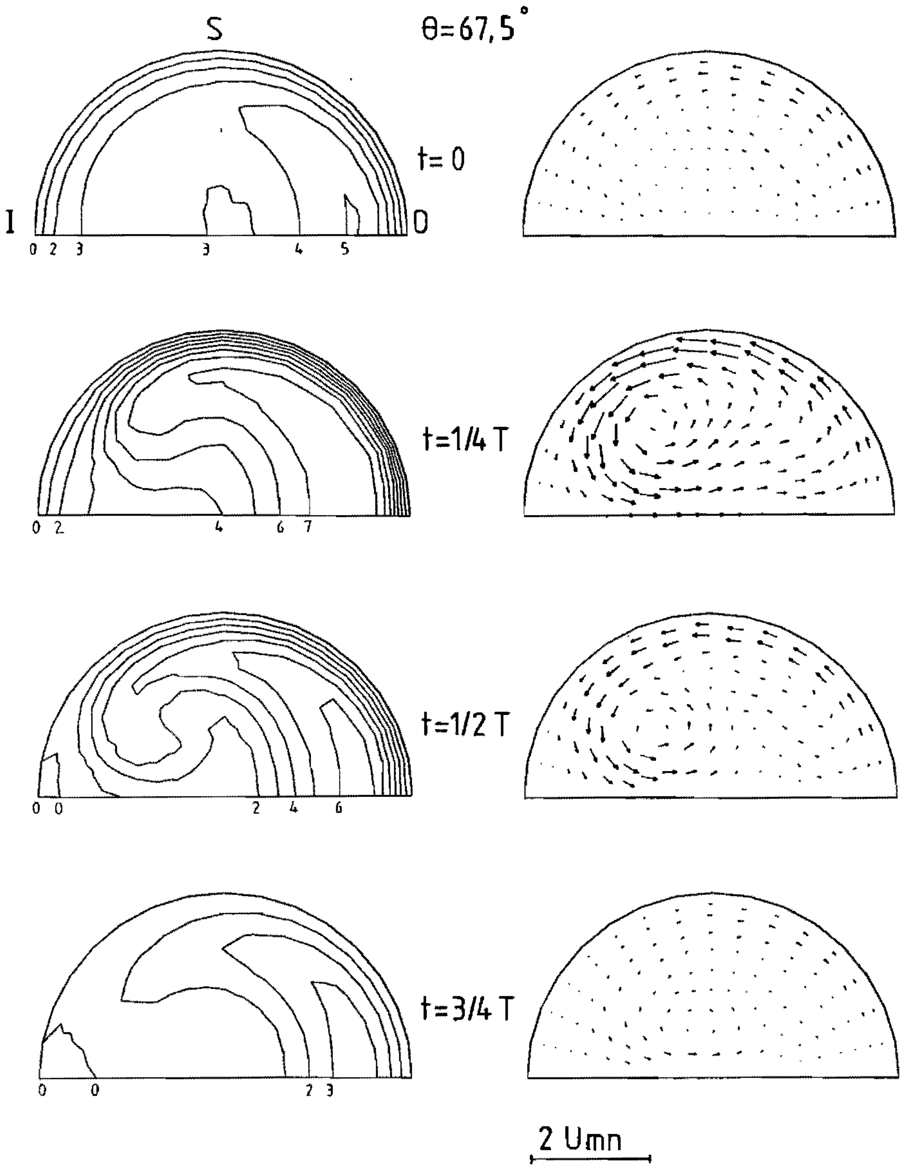

Figure 5.12d: Axial and secondary flow for the reference flow case at θ=67.5°.

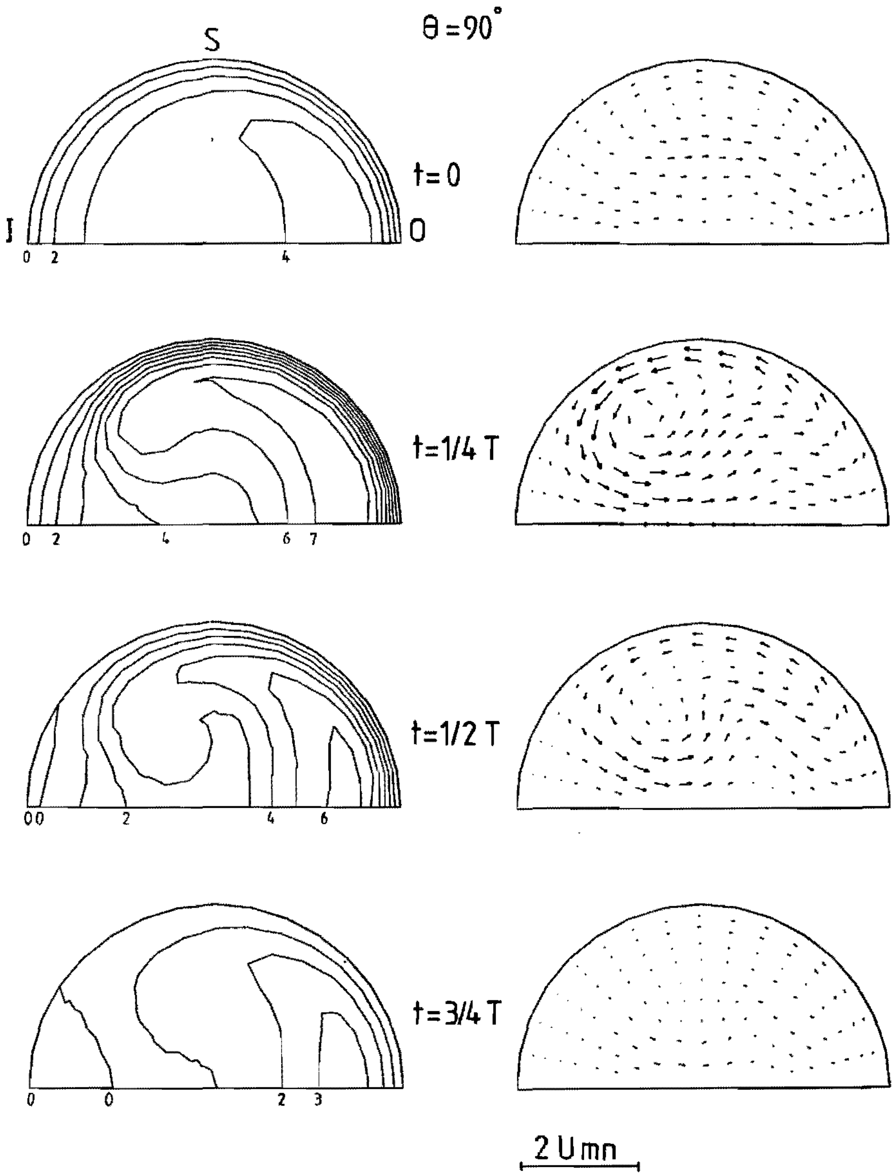

Figure 5.12e: Axial and secondary flow for the reference flow case at θ=90°.

At θ=67.5° (fig. 5.12d) the secondary velocities are considerably lower, as compared to the secondary velocities halfway the curved tube, except at maximal flow rate (t=1/4T). At θ=67.5° the 'tail' in the secondary flow field is also observed at maximal flow rate and it intensifies in the deceleration phase. The position of the center of the secondary vortex at t=1/4T, 1/2T and 3/4T is almost the same as compared to the position halfway the curved tube. Also in the deceleration phase, C–shaped axial velocity contours develop with highly curved segments at t=1/2T. Halfway the acceleration phase (t=0) a local minimum is observed at the center of the tube. Regions with almost constant axial velocities occur at minimal flow rate (t=3/4T) and halfway the acceleration phase (t=0). Reversed axial flow regions are found near the inner wall at t=1/2T and 3/4T. The region with negative axial velocities at the center of the tube has disappeared.

Globally spoken, the axial and secondary flow fields at θ=90° (fig. 5.12e) have the same appearance as the flow fields at θ=67.5°. However, the secondary velocities at maximal flow rate are lower, as compared with the secondary velocities at θ=67.5°. Also the C–shaped axial velocity contours are less pronounced at t=3/4T and the local axial velocity minimum at t=0 has disappeared.

5.3.3 Qualitative comparison with experiments

To validate the numerical results, laser Doppler experiments were performed in a 90–degree curved tube. The experimental set–up is described earlier in chapter 4. Although the adjusted flow rate in the experiments consisted of a sinusoidally varying component (–300<Re<300) superimposed on a steady flow component (Re=500), some differences with the numerical situation were found to be present. It appeared that the minimal Reynolds number was larger than 200 and that the flow rates at t=0 and 1/2T showed rather large differences. In table 5.13 the Reynolds number is presented as function of time, averaged over the positions at which laser Doppler velocity measurements were performed (θ=0°, 22.5°, 45°, 67.5° and 90°). Errors in the Reynolds number resulting from numerical integration of the axial flow field are estimated to be ±10. The rather large differences between the experimental and numerical situation can possibly be explained by the strategy applied for the adjustment of the flow rate in the experiments. First, the steady flow component was adjusted at a Reynolds number of 500. Afterwards the unsteady flow component was imposed and a maximal Reynolds number of 800 was adjusted. In this strategy, however, the influence of the unsteady flow component on the 'steady' flow component was not taken into account, which may result in the observed discrepancies. Besides, the sampling frequency of 50 samples per period contributes to these discrepancies. Due to this sampling frequency data presentation at exactly minimal, mean and maximal flow rate is impossible. This may result in errors in the Reynolds number of ±20 at mean flow rate.

t	0	1/4T	1/2T	3/4T
Re	565	800	460	250

Table 5.13: Reynolds number as function of time in the experiments.

A qualitative comparison with the laser Doppler velocity measurements is achieved by presentation of the axial velocities in the plane of symmetry and the axial contour levels and secondary velocity profiles at θ=22.5° and 67.5°. In figure 5.14a the axial velocity profiles in the plane of symmetry are presented as function of time for both the measurements and the calculations. A good agreement between the experimental and numerical data is observed. The largest differences occur

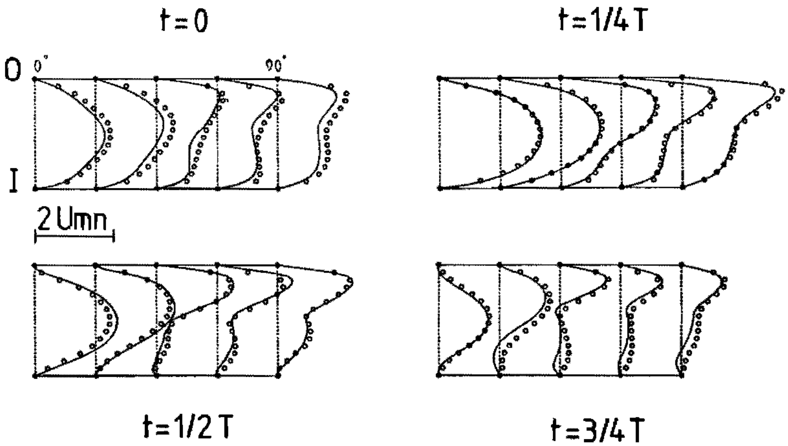

Figure 5.14a: Calculated (——) and measured (ooo) axial velocity profiles in the plane of symmetry.

halfway the acceleration phase at t=0 and at the end of the deceleration phase at t=3/4T. For both time intervals the velocities found in the experiments are somewhat higher than the velocities calculated by the numerical model, probably caused by the larger Reynolds number in the experiments at these time intervals. For the experiments this discrepancy results in the absence of regions with reversed axial flow downstream in the curved tube at minimal flow rate (t=3/4T). The shift of the maximum of axial velocity towards the outer wall is clearly seen at all time intervals. Also the presence of a local minimum in the axial velocity field at $\theta=67.5^{\circ}$ and t=0 is observed for both the measurements and the calculations. Such minima also occur downstream in the curved tube at t=1/2T and 3/4T.

In figure 5.14b the axial velocity contours at $\theta=22.5^{\circ}$ and 67.5° are presented as function of time. Contour level 0 corresponds to zero axial velocity and the difference in axial velocity between two successive levels corresponds to 0.52 times the time–averaged mean axial velocity (U_{mn}). The agreement between the numerical and experimental data is satisfactory. The regions with reversed axial flow calculated by the numerical model at the end of the deceleration phase are absent in the experiments, probably due to the larger Reynolds number in the experiments at this time interval. The largest differences in the C–shaped appearance of the axial velocity contours occur at $\theta=67.5^{\circ}$ and t=1/2T, where the curvature of the contour levels 2 and 3 is more pronounced, whereas the curvature of contour level 1 is less pronounced for the computations, possibly also as a consequence of the difference in the Reynolds number at this time interval. The position of the local axial velocity minimum at $\theta=67.5^{\circ}$ and t=0 is closer to the inner bend for the experiments than for the calculations.

A qualitative comparison of the secondary flow field is performed with the use of velocity profiles of secondary flow. In figure 5.14c the component of secondary flow parallel to the plane of symmetry is presented in the upper half and the component perpendicular to the plane of symmetry in the lower half of the cross–sectional area. The agreement between the experimental and numerical data is fair. The largest differences occur in the component parallel to the plane of symmetry near the side wall of the curved tube at both positions for t=1/4T and 1/2T. Near the plane of symmetry the largest differences in this component occur at $\theta=67.5^{\circ}$ for t=1/4T and 1/2T, but these differences are small compared to the differences near the side wall. Possibly, the rather large dimensions of the measuring volume contribute to these discrepancies. The main differences in the component perpendicular to the plane of symmetry occur at $\theta=67.5^{\circ}$ for t=1/4T and 1/2T, where a shift in the profiles near the inner bend of the curved tube is observed, probably due to positioning errors of the measuring volume.

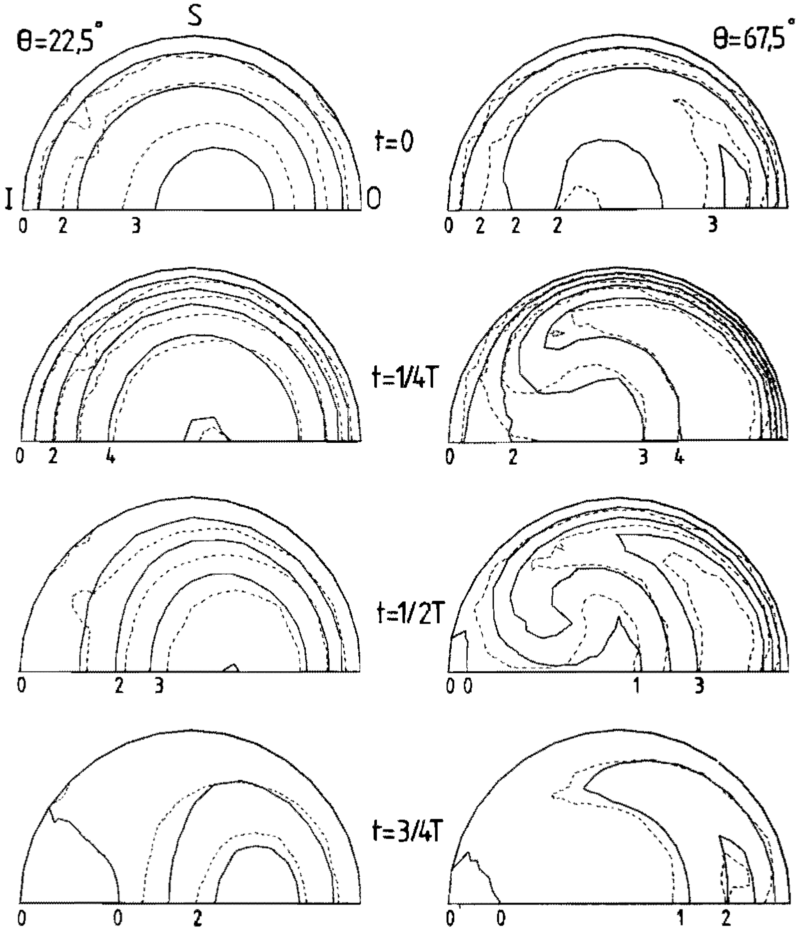

Figure 5.14b: Calculated (——) and measured (— —) axial flow field at 2 positions in the curved tube.

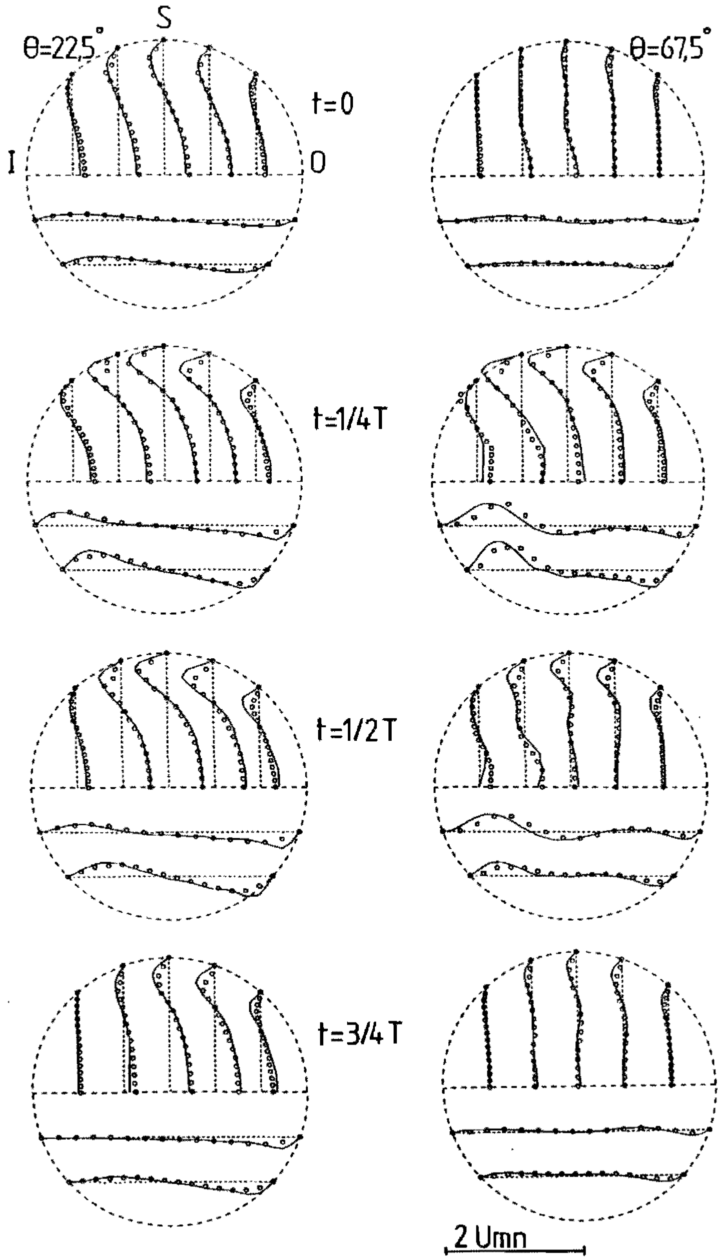

Figure 5.14c: Calculated (——) and measured (ooo) secondary flow field at 2 positions in the curved tube.

5.3.4 Quantitative comparison with experiments

A quantitative comparison of the axial flow field calculated by the numerical model with the axial flow field found in the experiments, is carried out by its first moment <X/a>, the definition of which is given in section 5.2.4. (eq. 5.1). In table 5.15 the experimental and numerical values of this quantity are presented as function of time and position in the curved tube. Taking into account the 95%–confidence intervals, which are only based upon errors in the adjustment of the laser Doppler equipment, there is a rather good agreement between the experimental and numerical data. The largest differences occur at the end of the deceleration phase (t=3/4T). This is due to the absence of reversed axial flow in the experiments at this time interval, as a consequence of the larger Reynolds number. At $\theta=0^{\circ}$ a small shift of the axial flow field towards the inner bend is found. The largest shifts towards the outer wall are observed at t=3/4T. At this time interval <X/a> is almost constant throughout the curved tube. A quarter of a period later, halfway the acceleration phase, the smallest values of <X/a> are found.

	$\theta=0^{\circ}$	$\theta=22.5^{\circ}$	$\theta=45^{\circ}$	$\theta=67.5^{\circ}$	$\theta=90^{\circ}$
t=0	−0.02/−0.03	0.03/0.01	0.09/0.11	0.05/0.06	0.08/0.07
t=1/4T	−0.02/−0.03	0.05/0.03	0.08/0.11	0.08/0.10	0.13/0.10
t=1/2T	−0.01/−0.03	0.13/0.12	0.17/0.22	0.14/0.16	0.21/0.18
t=3/4T	0.00/−0.01	0.20/0.29	0.21/0.30	0.16/0.26	0.23/0.30

Table 5.15: First moment of axial flow as function of time and position (experiments (±0.02)/calculations).

Quantification of the secondary velocities in the plane of symmetry is performed by the axial vorticity of the central core ξ_c (sect. 5.2.4, eq. 5.2). In table 5.16 the values of this quantity are presented for both the calculations and the experiments. The agreement between the numerical and experimental values is satisfactory. The largest differences occur at the onset and halfway the acceleration phase at $\theta=45^{\circ}$. At $\theta=0^{\circ}$ the secondary velocities in the plane of symmetry are directed towards the inner bend causing negative values of ξ_c, whereas at all other cross–sections these velocities are directed towards the outer wall. Halfway the acceleration phase at θ=67.5°, however, ξ_c is equal to zero for the experimental case and small for the numerical one. The largest values of ξ_c are found at θ=22.5° at all time intervals and at θ=45° at peak flow rate. During the deceleration phase the values of ξ_c at θ=67.5° and 90° are almost the same.

	θ=0°	θ=22.5°	θ=45°	θ=67.5°	θ=90°
t=0	−0.06/−0.05	0.26/0.24	0.21/0.12	0.00/0.02	0.10/0.06
t=1/4T	−0.08/−0.07	0.39/0.37	0.35/0.38	0.18/0.19	0.16/0.17
t=1/2T	−0.03/−0.03	0.36/0.38	0.17/0.20	0.10/0.07	0.12/0.07
t=3/4T	−0.02/ 0.00	0.21/0.21	0.06/0.13	0.07/0.08	0.07/0.06

Table 5.16: Axial vorticity of the central core as function of time and position (experiments (±0.02)/calculations).

For quantification of the secondary velocities near the side wall, the axial vorticity was calculated along a path consisting of a semicircle in the cross–sectional plane, with a radius equal to 4/5 times the radius of the tube, which was closed along the plane of symmetry (ξ_s). In this study quantification is performed by ξ_s rather than by ξ_m, the maximum of axial vorticity, as in this way a better comparison can be achieved between the various flow problems to be dealt with in the next section. In table 5.17 ξ_s is presented as function of time and position for both the experiments and the calculations. The agreement between the experimental and numerical results is satisfactory at θ=0°, 22.5° and 67.5°. At θ=45°, however, throughout the deceleration phase the value of this quantity is much larger for the calculations than for the experiments. This also holds at θ=90° at peak flow rate. These differences are possibly caused by measuring inaccuracies near the side wall of the curved tube and positioning errors of the measuring volume. Also for the steady flow case large differences between the experimental and numerical values of the maximum of axial vorticity are found. In spite of these differences it can be concluded that the maximal values of this quantity occur at θ=22.5° and 45° at peak flow rate. Small values of ξ_s are found at θ=90° and 67.5° at the time intervals t=0 and 3/4T. The positive values at θ=0° over the full period of time, point to the fact that the secondary velocities, which are directed towards the inner bend, are higher near the side wall than in the plane of symmetry.

	$\theta=0^{\circ}$	$\theta=22.5^{\circ}$	$\theta=45^{\circ}$	$\theta=67.5^{\circ}$	$\theta=90^{\circ}$
t=0	0.04/0.05	0.69/0.65	0.57/0.56	0.14/0.19	0.11/0.12
t=1/4T	0.08/0.09	1.12/1.11	1.14/1.44	0.83/0.94	0.26/0.47
t=1/2T	0.07/0.07	0.99/1.10	0.68/0.98	0.38/0.44	0.15/0.14
t=3/4T	0.02/0.01	0.54/0.58	0.28/0.51	0.15/0.21	0.08/0.13

Table 5.17: Axial vorticity at r=4/5a as function of time and position (experiments (±0.05)/calculations).

5.4 Influence of various parameters on axial and secondary flow

5.4.1 Introduction

To gain more insight into the influence of the frequency parameter and the steady flow component on axial and secondary flow, calculations were performed at a Womersley parameter of 15 and 24.7, for a Reynolds number varying between 200 and 800, and at a Womersley parameter of 7.8 and 24.7, for a Reynolds number varying between –300 and 300. For the latter two flow cases the Reynolds number was adjusted by lowering the axial velocity values. Also axial and secondary flow were investigated for a physiologically varying flow rate, as presented in figure 5.20. The Reynolds number varied between 200 and 800, with a time–averaged mean Reynolds number of about 300. The Womersley parameter for this flow case was equal to 4. All flow cases are summarized in table 5.18. Flow case 1 is the situation described in detail before. This case will be denoted as the reference flow case.

	Reynolds number	Dean number	Womersley parameter	Flow wave
case 1	200:800	82:327	7.8	pulsating
case 2	200:800	82:327	15.0	pulsating
case 3	200:800	82:327	24.7	pulsating
case 4	200:800	82:327	4.0	physiological
case 5	–300:300	–122:122	7.8	oscillating
case 6	–300:300	–122:122	24.7	oscillating

Table 5.18: Summary of the parameters for the unsteady flow cases.

For the flow cases 2 and 3 the finite element division consisted of 15 elements in axial direction and 30 elements per cross–section. The lengths of the inlet and outlet sections were equal to 2 times the radius of the tube and consisted of 1 and 2 elements in the axial direction, respectively. Using this element division for the calculation of axial and secondary flow for flow case 1, no remarkable differences with the results presented earlier were found. For flow case 4 the same element division was used as for flow case 1. The boundary conditions for the flow cases 2,3 and 4 were the same as employed for flow case 1, i.e. at the inlet fully developed unsteady pipe flow was assumed. To that end for the physiological flow wave 15 harmonics were used to correctly prescribe the axial flow field at the inlet. From a velocity calculation of fully developed oscillating flow in a straight tube, it appeared that the stress–free boundary condition at the outlet gave rise to large oscillations in the velocities in the outstream region. Therefore, essential boundary conditions, describing fully developed oscillating flow in straight tubes, were applied to both ends of the curved tube for the flow cases 5 and 6. To ensure that fluid flow was fully developed, the lengths of the instream and outstream sections for flow case 5 were chosen to be 20 times the radius of the tube. For flow case 6 the same element division was used as for flow case 1. Two dimensional test calculations in straight tubes revealed that these lengths were reasonable estimates. Because of the long instream and outstream pipes for flow case 5 and due to the limited capacity of the computer used for this calculation, the number of elements per cross–section had to be reduced to 20. The total number of elements in the axial direction was equal to 28.

In table 5.19 the number of periods needed to reach convergence are presented. For the flow cases 1,2 and 3 the number of periods seems to be linearly dependent on the Womersley parameter. For these flow cases it was typical to see that the curvature of the axial isovelocity lines intensified with increasing period number. This phenomenon probably indicates that the number of periods needed to reach convergence is dominated by the development of the flow field induced by the steady flow component. For the physiological flow case one and a half period was sufficient to reach convergence because flow at the end of the diastolic phase was found to be quasi–steady. For oscillating flow rates the number of periods appears to be smaller for higher Womersley parameters, which is different from the pulsatile flow cases. This is plausible due to the absence of a steady flow component and the resulting lower secondary velocities at higher frequencies.

flow case	1	2	3	4	5	6
N	3	6	9	1.5	6	3

Table 5.19: Number of periods needed to reach convergence (N) for the various flow cases.

As for the reference case, the number of time steps per period for the flow cases 2,3,5 and 6 was equal to 24. For the physiological flow case variable time steps were applied, as pointed out in figure 5.20. The time steps in the systolic phase were taken equal to 1/128T, whereas the time steps at the end of the diastolic phase were set equal to 3/64T.

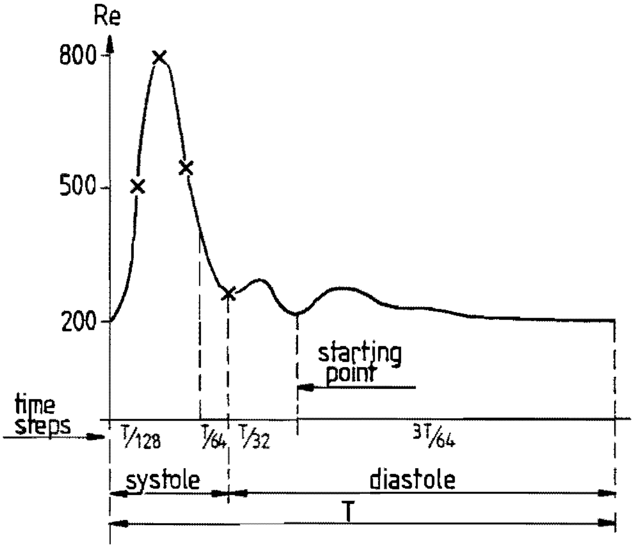

Figure 5.20: Time steps and presentation levels for the physiological flow case.

For the flow cases 2,3,5 and 6 first an Euler–implicit time integration scheme was applied during 3/4T, succeeded by a Crank–Nicolson scheme. For the flow cases 2,3 and 5, after 3 periods again an Euler–implicit time integration scheme was applied during 3/4T because of the bad convergence of the solution. All velocity calculations were started at minimal flow rate and used a zero velocity field as initial condition. In case of the physiological flow wave the calculation was started near the onset of the diastolic phase (fig. 5.20). For this flow case during 11 time steps an Euler–implicit time integration scheme was applied.

For all flow cases except 4, the results are presented at the same time levels as for the reference flow case, i.e. at mean flow rate in the acceleration phase, at peak flow rate, at mean flow rate in the deceleration phase and at minimal flow rate. For the physiological flow wave the results are presented at the time intervals indicated in figure 5.20. At these time intervals the Reynolds numbers were equal to 500, 800, 540 and 265, respectively.

5.4.2 Qualitative comparison between the various flow cases

– *The influence of the frequency parameter*

In figure 5.21 the results of axial flow in the plane of symmetry and axial and secondary flow at θ=22.5° and 67.5° as function of time are shown for the flow cases 1 and 2 (flow case 2: 200<Re<800, α=15, pulsating). From the axial velocity profiles (fig. 5.21a) it is observed that at minimal flow rate and halfway the acceleration phase the axial velocities near the inner bend are consequently lower for flow case 2, as compared to those for the reference flow case, whereas these velocities are consequently higher at the other time intervals. This results in larger regions with reversed axial flow at t=3/4T and more pronounced axial velocity plateaus at t=1/4T. The shift of the axial velocity maximum towards the outer bend is about the same for both flow cases. At peak flow rate relatively high axial

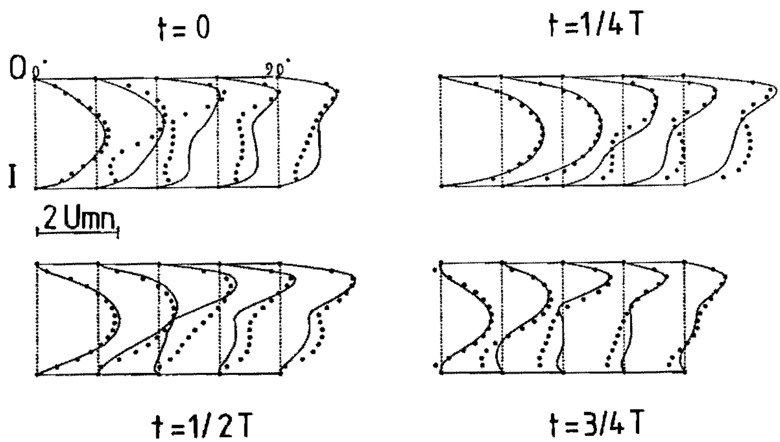

Figure 5.21a: Axial flow in the plane of symmetry for flow case 1 (——) and flow case 2 (●●●).

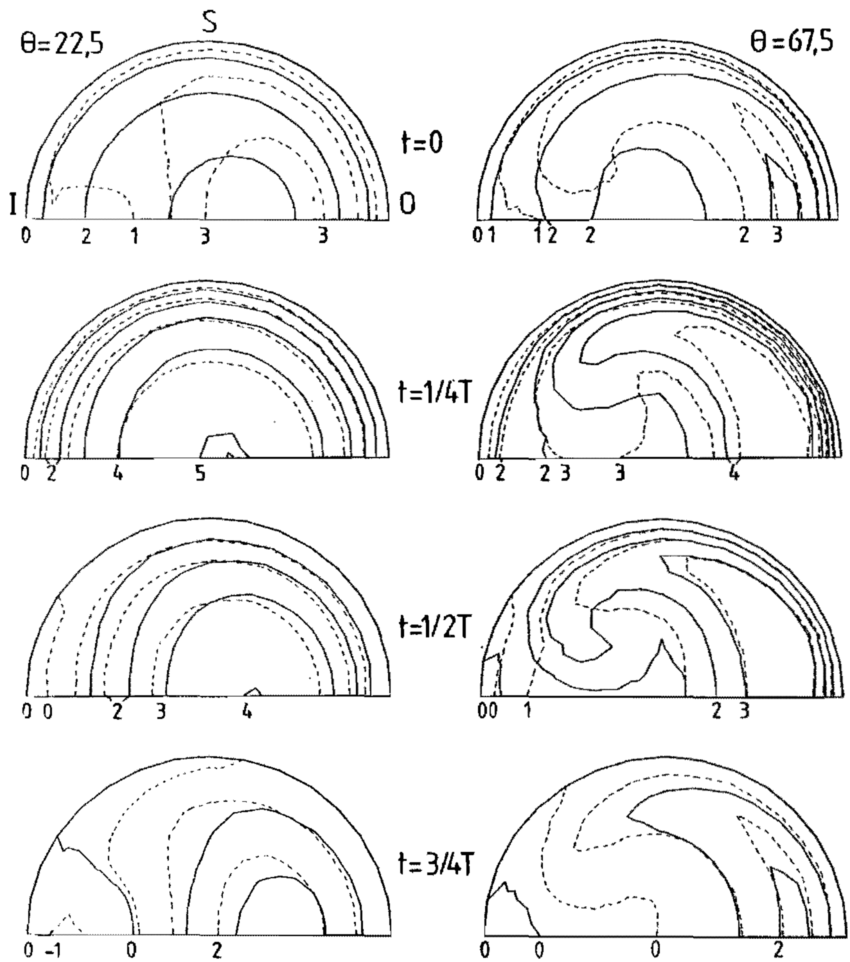

Figure 5.21b: Axial flow at θ=22.5° and 67.5° for flow case 1 (——) and flow case 2 (— —).

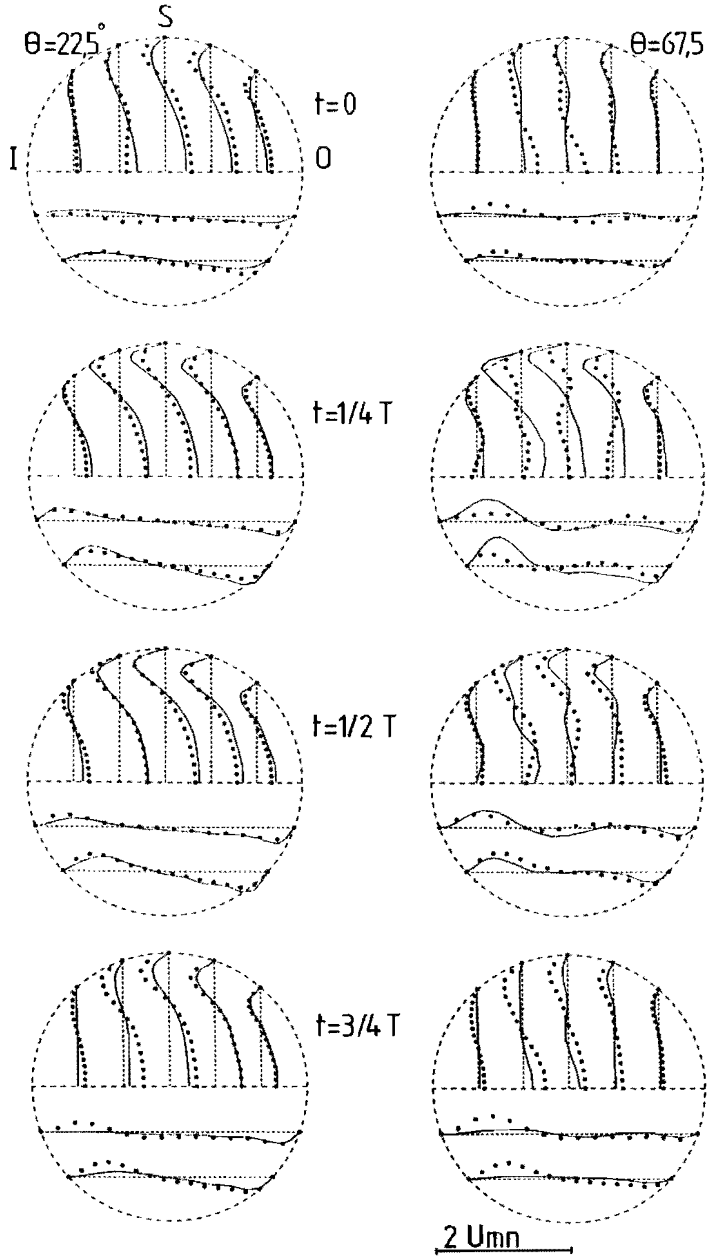

Figure 5.21c: Secondary flow at θ=22.5° and 67.5° for flow case 1 (——) and flow case 2 (●●●).

velocity minima occur downstream in the curved tube for flow case 2. On the contrary to the velocity gradients at the outer wall, for flow case 2 the velocity gradients at the inner wall are much larger at peak flow rate and much smaller at minimal flow rate, as compared to the velocity gradients for the reference flow case.

In figure 5.21b the axial velocity contours at $\theta=22.5^\circ$ and 67.5° are presented as function of time. At $\theta=22.5^\circ$ the largest differences in the axial velocities occur halfway the acceleration phase (t=0), where the contours have a much more asymmetric appearance for flow case 2 than for the reference flow case, and at the end of the deceleration phase (t=3/4T). At the latter time interval, for flow case 2 a larger region with reversed axial flow is found with negative axial velocities of about 50% of the mean axial velocity at t=0. This region has extended towards the upper side wall of the curved tube. At $\theta=67.5^\circ$, the differences between the two flow cases are expressed by the more or less pronounced C–shaped axial velocity contours and the larger region with negative axial velocities at minimal flow rate for flow case 2, which extends towards the center of the tube in the plane of symmetry.

Secondary flow for the flow cases 1 and 2 is presented in figure 5.21c by secondary velocity profiles. At $\theta=22.5^\circ$ these secondary velocity profiles look quite the same for both flow cases. At minimal flow rate and halfway the acceleration phase the secondary velocities are somewhat higher for flow case 2, whereas, at peak flow rate these velocities are somewhat lower. At $\theta=67.5^\circ$, however, secondary flow for flow case 2 shows complicated structures, especially at t=1/4T and 1/2T. At peak flow rate on each line both components of secondary flow are changing two or three times of direction. Near the side wall all secondary velocities are directed from the outer bend towards the inner bend. Near the plane of symmetry, however, secondary velocities are found directed from the inner bend towards the outer bend, as well as secondary velocities directed from the outer bend towards the inner bend, pointing to the development of Lyne type structures. At all time intervals, except t=1/4T, the secondary velocities for flow case 2 are higher than the secondary velocities for the reference flow case.

In figure 5.22 the results are shown for the flow cases 1 and 3 (flow case 3: $200<Re<800$, $\alpha=24.7$, pulsating). From the axial velocity profiles in the plane of symmetry (fig. 5.22a) it is observed that the shift of the axial velocity maximum towards the outer bend develops in the same way for both flow cases. Also the velocity gradients at the outer wall are about the same, except at minimal flow rate at the positions $\theta=0^\circ$ and 22.5° due to the difference in the inlet profiles. On the contrary, large differences are found between the velocity gradients at the inner wall. As for flow case 2, for flow case 3 these velocity gradients are much larger at peak flow rate and much smaller at minimal flow rate, as compared to the velocity gradients for the reference flow case. At t=1/4T and 1/2T, the axial velocities near the inner bend are consequently higher for flow case 3. The region with reversed axial flow contains higher negative velocities for flow case 3. For θ=22.5° and 90° these regions are somewhat smaller in the plane of symmetry, whereas larger regions with reversed axial flow are found at θ=45° and 67.5°. Local minima in the axial velocity profiles are not observed for flow case 3.

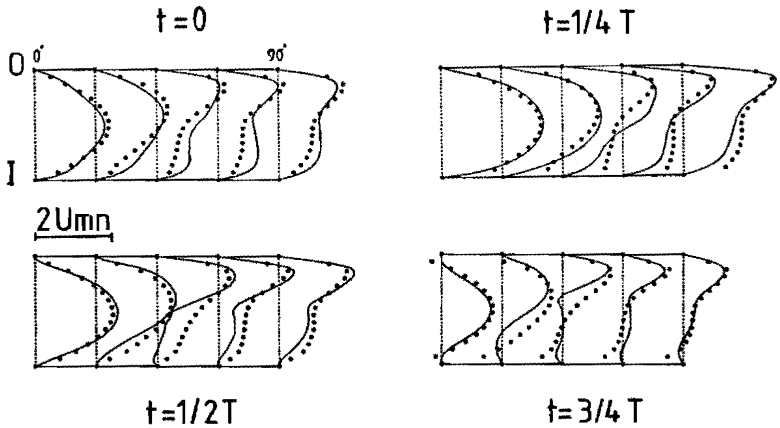

Figure 5.22a: Axial flow in the plane of symmetry for flow case 1 (——) and flow case 3 (●●●).

The axial velocity contours at θ=22.5°, presented in figure 5.22b, are quite the same at all time intervals, except at minimal flow rate. At this time interval a region with negative axial velocities along the total side wall is observed, whereas for the reference flow case this region is situated near the inner bend. This difference is mainly caused by the differences in the velocity profiles prescribed at the inlet for both flow cases. The axial velocity contours at θ=67.5° show more or less pronounced C–shaped isovelocity lines for flow case 3 and a larger region with reversed axial flow near the inner bend at t=3/4T. This region has extended towards the upper side wall.

The secondary velocity profiles for this flow case are presented in figure 5.22c. At θ=22.5° these profiles have the same appearance as the profiles for the reference flow case. The secondary velocities are somewhat higher for the time levels t=0 and 3/4T and somewhat lower for t=1/4T and 1/2T. At θ=67.5° larger

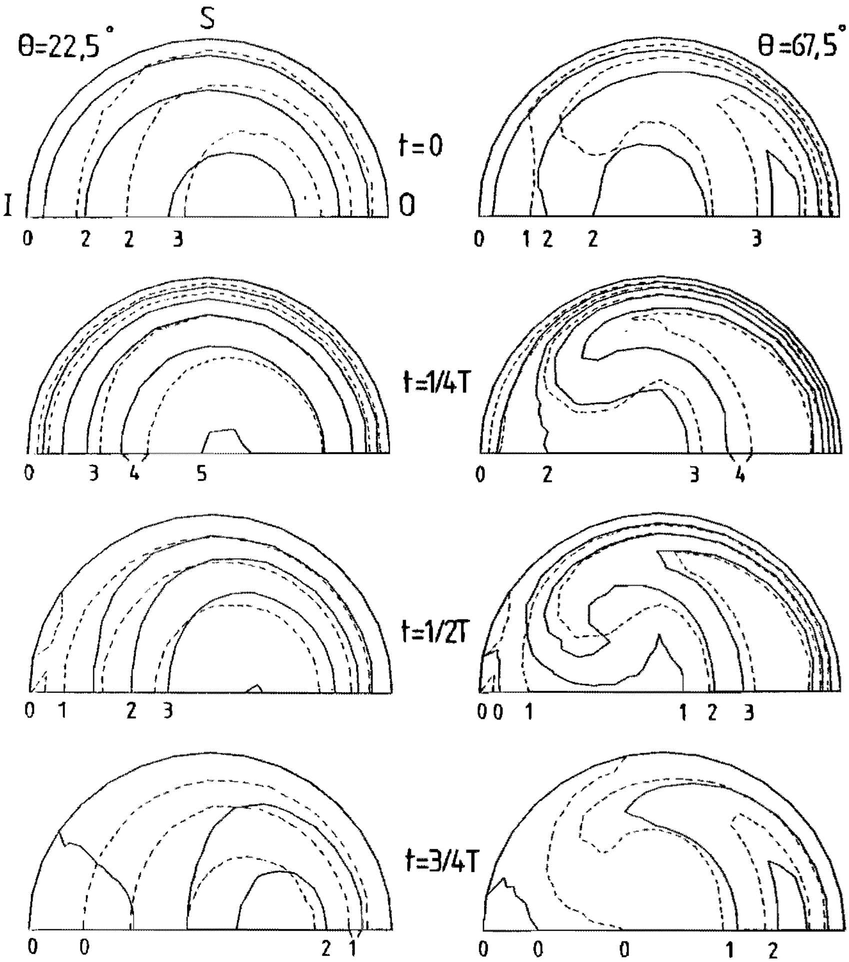

Figure 5.22b: Axial flow at θ=22.5° and 67.5° for flow case 1 (——) and flow case 3 (— —).

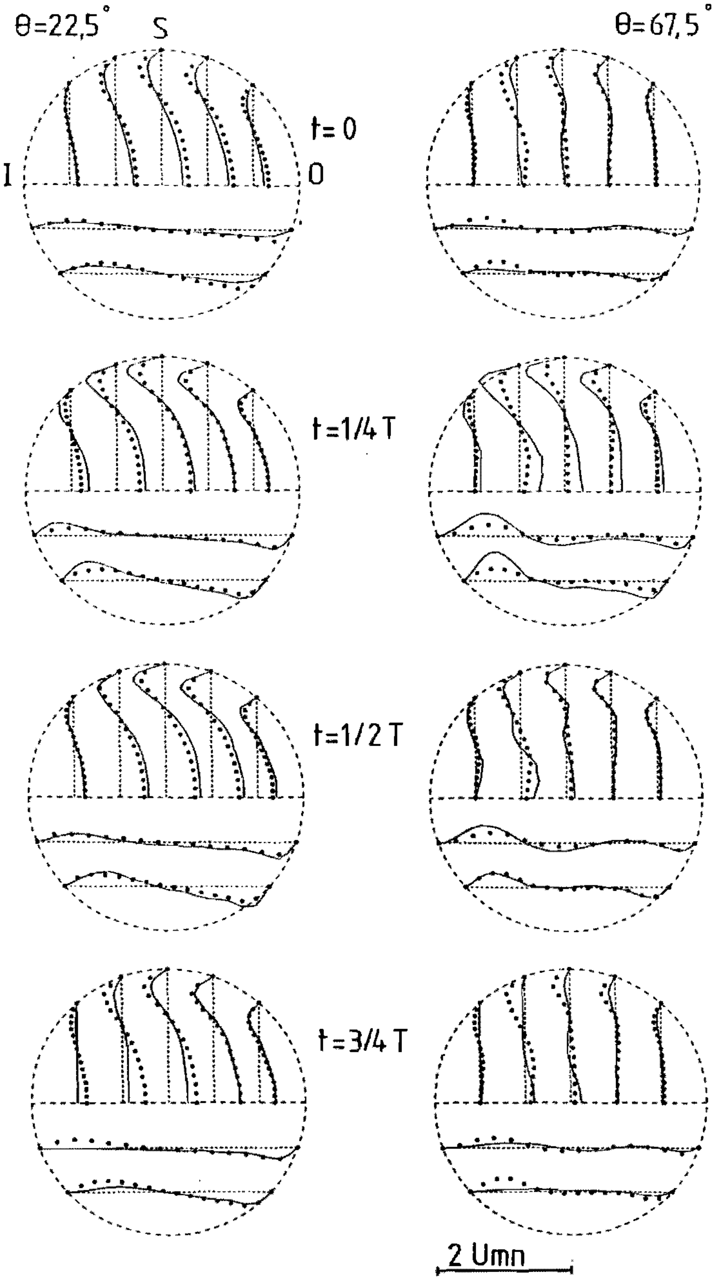

Figure 5.22c: Secondary flow at θ=22.5° and 67.5° for flow case 1 (——) and flow case 3 (●●●).

differences are found in the secondary flow field. The irregular structures as found for flow case 2, however, are not present here. Throughout the flow cycle, the secondary velocities parallel to the plane of symmetry, are directed from the inner bend towards the outer bend near the plane of symmetry and circumferentially back near the side wall. For flow case 3 at peak flow rate both secondary velocity components near the side wall are lower, whereas these components are higher at minimal flow rate, as compared to the secondary velocities for the reference flow case. It is remarkable that the secondary velocity profiles at both positions for flow case 3 are almost constant in time. Apparently the unsteadiness of the flow rate at this high value of the Womersley parameter, hardly affects the secondary flow field.

– Influence of the flow wave form

In figure 5.23 the results are shown for flow case 1 and flow case 4, the physiological flow wave (flow case 4: 200<Re<800, α=4, physiological). From the axial velocity profiles in the plane of symmetry, presented in figure 5.23a, it may be concluded that there is a good agreement between both flow cases. The largest differences occur at minimal flow rate and halfway the acceleration phase. At t=3/4T these differences are mainly observed in the higher axial velocities near the inner bend for flow case 4 and the absence of a region with reversed axial flow, probably due to the larger Reynolds number at this time interval. At t=0 the development of an axial velocity plateau near the inner bend is less pronounced for flow case 4 than for the

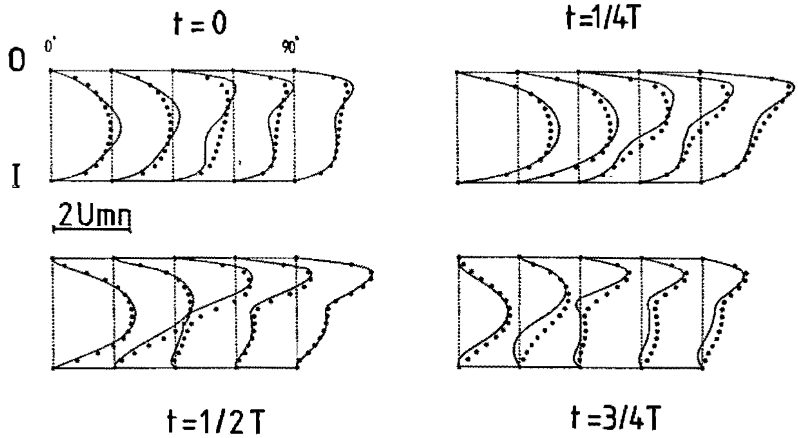

Figure 5.23a: Axial flow in the plane of symmetry for flow case 1 (——) and flow case 4 (●●●).

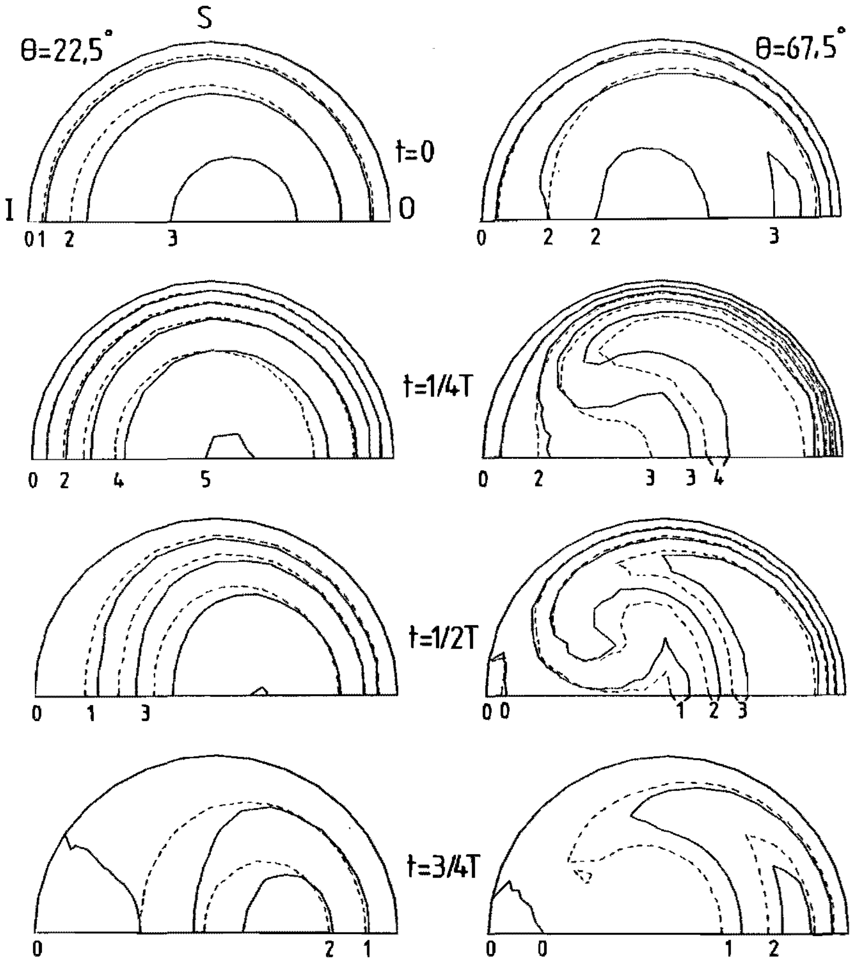

<u>Figure 5.23b</u>: Axial flow at θ=22.5° and 67.5° for flow case 1 (——) and flow case 4 (— —).

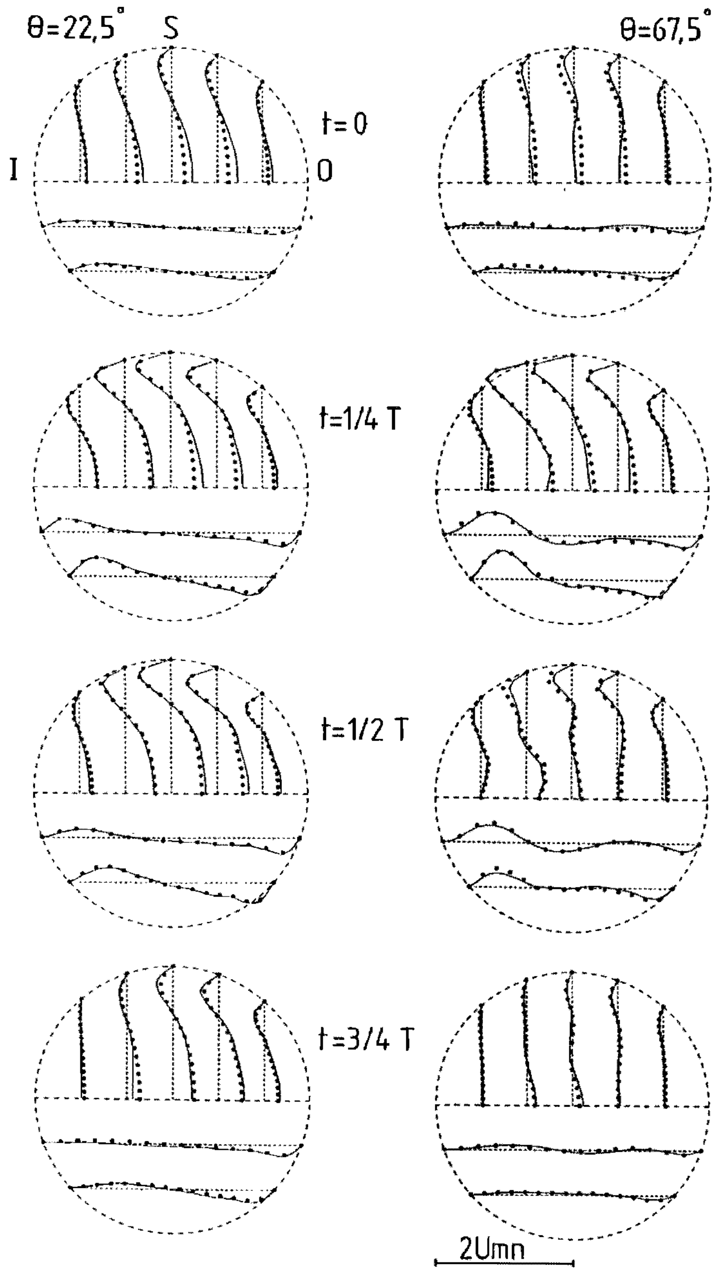

Figure 5.23c: Secondary flow at θ=22.5° and 67.5° for flow case 1 (——) and flow case 4 (●●●).

reference flow case. The shift of the axial velocity maximum towards the outer bend and the axial velocity gradients at the outer wall are about the same for both flow cases.

In figure 5.23b the axial velocity contours are presented for flow case 1 and 4. It is observed that there is a rather fair agreement between the axial velocity data at both cross–sectional planes. The main differences are characterized by the absence of regions with reversed axial flow due to the larger Reynolds number, and the absence of a local minimum in the axial flow field at θ=67.5° and t=0.

Also the secondary velocity profiles, presented in figure 5.23c, are in good agreement. The largest differences occur at t=0 and θ=67.5° for the secondary velocities near the plane of symmetry and near the side wall. From this comparison between axial and secondary flow it can be concluded that the influence of the diastolic phase on the flow phenomena occurring in the systolic phase is of minor importance.

– Influence of the steady flow component

To study the influence of the steady flow component on the secondary flow field, the secondary velocities parallel to the plane of symmetry are presented along the lines as depicted in figure 5.24. These secondary velocities are presented along the line IO in the plane of symmetry and the line CS, perpendicular to this plane. A positive value points at a secondary velocity directed towards the outer bend. Both the results of the pulsating and oscillating flow cases are presented. Besides, the numerical results are compared with experimental data.

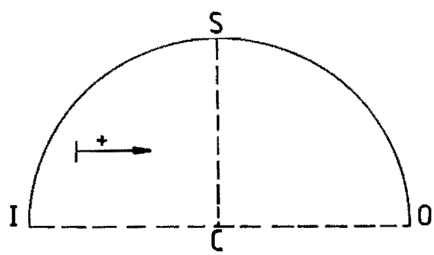

Figure 5.24: Presentation lines of the secondary velocity component directed parallel to the plane of symmetry (I: inner, O:outer, C:center, S: side).

In figure 5.25 the results for the flow cases 1 and 5 (flow case 5: –300<Re<300, α=7.8, oscillating) are presented. For flow case 1 all secondary velocities at $\theta=0^\circ$ are directed towards the inner wall, caused by upstream influences of the curved tube. For all time intervals downstream in the curved tube the secondary velocities in the plane of symmetry are directed towards the outer bend, except for a small region at t=0 and $\theta=67.5^\circ$. For most time intervals the secondary velocities in the plane of symmetry at $\theta=67.5^\circ$ and 90° are higher at the inner bend than at the outer bend. The secondary velocities along the line CS are directed from the inner bend towards the outer bend near the plane of symmetry and circumferentially back near the side wall at $\theta=22.5^\circ$, 45°, 67.5° and 90°, except for a small region at $\theta=67.5^\circ$ at t=0 and 1/2T.

For flow case 5 the secondary velocities in the plane of symmetry at $\theta=22.5^\circ$, 45° and 67.5° are always directed towards the outer bend. At $\theta=0^\circ$ these velocities are directed towards the outer wall at t=0, 1/2T and 3/4T and directed towards the inner wall at t=1/4T. At this time interval $\theta=0^\circ$ can be regarded as the inlet of the curved tube which, therefore, experiences upstream influences. At t=3/4T, however, $\theta=0^\circ$ can be regarded as the outlet of the curved tube due to the negative flow rate. Therefore, at this time interval the secondary velocities in the plane of symmetry are directed towards the outer wall due to centrifugal forces. At $\theta=90^\circ$ the opposite is happening. At $\theta=22.5^\circ$, 45° and 67.5° the secondary velocities along the line CS are directed towards the outer bend near the plane of symmetry and circumferentially back near the side wall. At these positions the secondary velocities are relatively constant in time. At minimal flow rate and halfway the acceleration phase, the same happens at $\theta=0^\circ$, whereas, at t=1/4T these velocities are directed towards the inner wall. At t=1/2T these velocities are almost zero.

A comparison between the pulsating and oscillating flow cases reveals that the secondary velocities for the pulsating flow case are higher than those for the oscillating flow case, especially at peak flow rate and halfway the deceleration phase. This is caused by the presence of a steady flow component. The velocity profiles for the oscillating flow case are much smoother than the velocity profiles for the pulsating flow case. The secondary velocity profiles point at the occurrence of a pure Dean type vortex for the oscillating flow case, whereas for the pulsating flow case 'tail'–formation occurs in the secondary flow field, resulting in the non–smooth secondary velocity profiles downstream in the curved tube. A comparison with the experiments reveals a relatively good agreement between the numerical and experimental data. For the oscillating flow case the velocities in the plane of symmetry are consequently lower for the experiments than for the calculations. It is likely that inaccuracies in the measurements are the major cause for this.

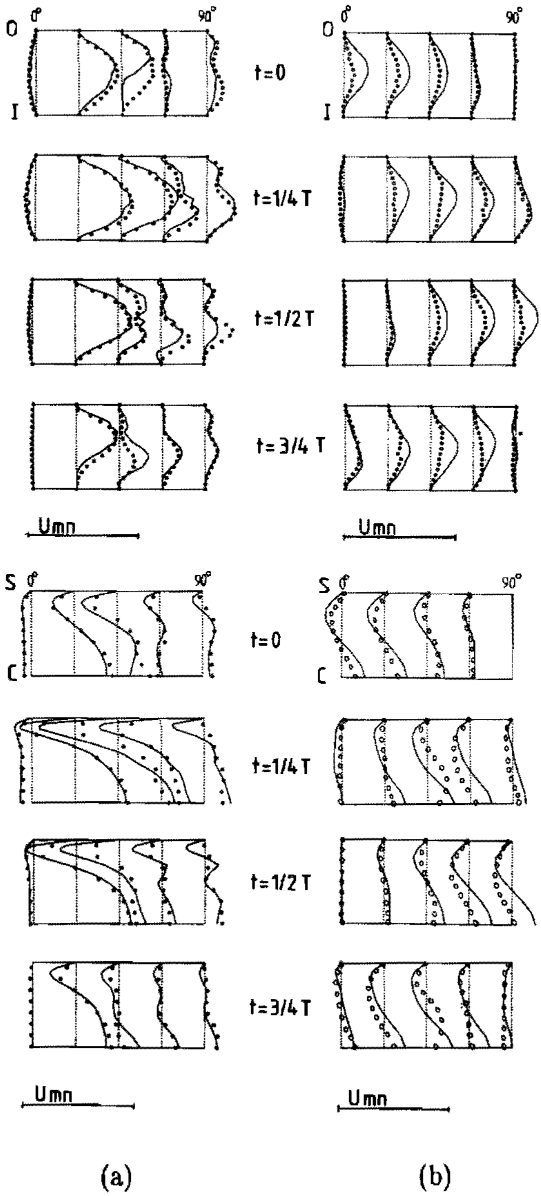

Figure 5.25: Secondary velocities parallel to the plane of symmetry for the pulsating (a) and the oscillating (b) flow case at α=7.8. Experimental data are indicated by dots. U_{mn} stands for the time–averaged mean axial velocity for the pulsating flow case.

In figure 5.26 the results for the flow cases 3 and 6 (flow case 3:$200<Re<800$, $\alpha=24.7$, pulsating; flow case 6: $-300<Re<300$, $\alpha=24.7$, oscillating) are presented. For the pulsating flow case it is observed that the secondary velocities are directed towards the outer wall near the plane of symmetry and towards the inner wall near the side wall of the curved tube at $\theta=22.5^\circ$, 45°, 67.5° and 90°. The secondary velocities in the plane of symmetry are much lower at $\theta=67.5^\circ$ and 90°, as compared to the secondary velocities at $\theta=22.5^\circ$ and 45°. The secondary velocities at the entrance of the tube ($\theta=0^\circ$) are always directed towards the inner bend. Compared to the pulsating flow case at $\alpha=7.8$, the secondary velocities are relatively constant at all time intervals, indicating that at higher frequencies secondary flow is highly determined by the steady flow component.

The secondary velocities for the oscillating flow case are presented in figure 5.26b. These velocities are scaled up 5 times, as compared to the secondary velocities for the pulsating flow case. At $\theta=22.5^\circ$, 45° and 67.5° the secondary velocities predicted by the numerical model are low, as compared to the secondary velocities at $\theta=0^\circ$ and 90°. At $\theta=0^\circ$ the secondary velocities are directed towards the inner bend at t=1/4T and 1/2T (for the numerical case) and towards the outer wall at t=0 and 3/4T. At $\theta=90^\circ$ the opposite is happening.

A comparison between the experimental and numerical data reveals relatively large differences in case of oscillating flow. At most time intervals and positions in the tube, the measured velocities are higher than the calculated ones. It must be kept in mind, however, that the secondary velocities for the oscillating flow case are very low, as compared to the axial velocities. Therefore, small errors in the adjustment of the laser Doppler equipment may result in rather large errors in the determination of the secondary velocities. The oscillations in the numerical profiles for the secondary velocity component in the plane of symmetry at $\theta=0^\circ$ and 90° are probably caused by a too coarse element division in the axial direction. The axial velocity profiles at $\theta=22.5^\circ$, 45° and 67.5°, presented in figure 5.27, reveal that the entrance angle to reach full development is smaller than 22.5°. Therefore, the applied number of 3 elements in the axial direction between $\theta=0^\circ$ and 22.5° was probably to small to adequately predict this rapid development.

In figure 5.27 the axial velocity profiles in the plane of symmetry and the secondary velocity profiles at $\theta=45^\circ$ and t=1/4T, are presented for the oscillating flow cases. It is observed that for both flow cases the axial velocity maximum is shifted towards the inner wall except in the downstream region of the curved tube for $\alpha=7.8$ at t=3/8T. For both Womersley parameters large upstream influences are

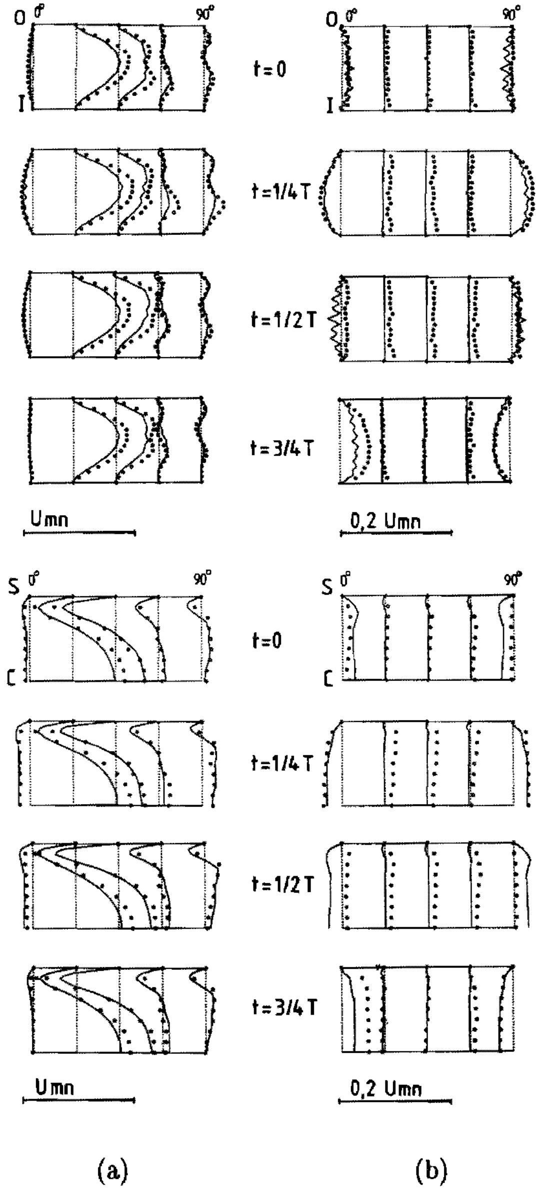

Figure 5.26: Secondary velocities parallel to the plane of symmetry for the pulsating (a) and the oscillating (b) flow case at α=24.7. Experimental data are indicated by dots. U_{mn} stands for the time–averaged mean axial velocity for the pulsating flow case.

observed at t=1/8T and 1/4T. The secondary flow field at θ=45° resembles a pure Dean type vortex for α=7.8, whereas the secondary flow field for α=24.7 shows a central core in which the velocities are directed towards the inner wall pointing at a Lyne type secondary flow field. The secondary velocities for α=24.7, however, are about 50 times lower than the secondary velocities for α=7.8.

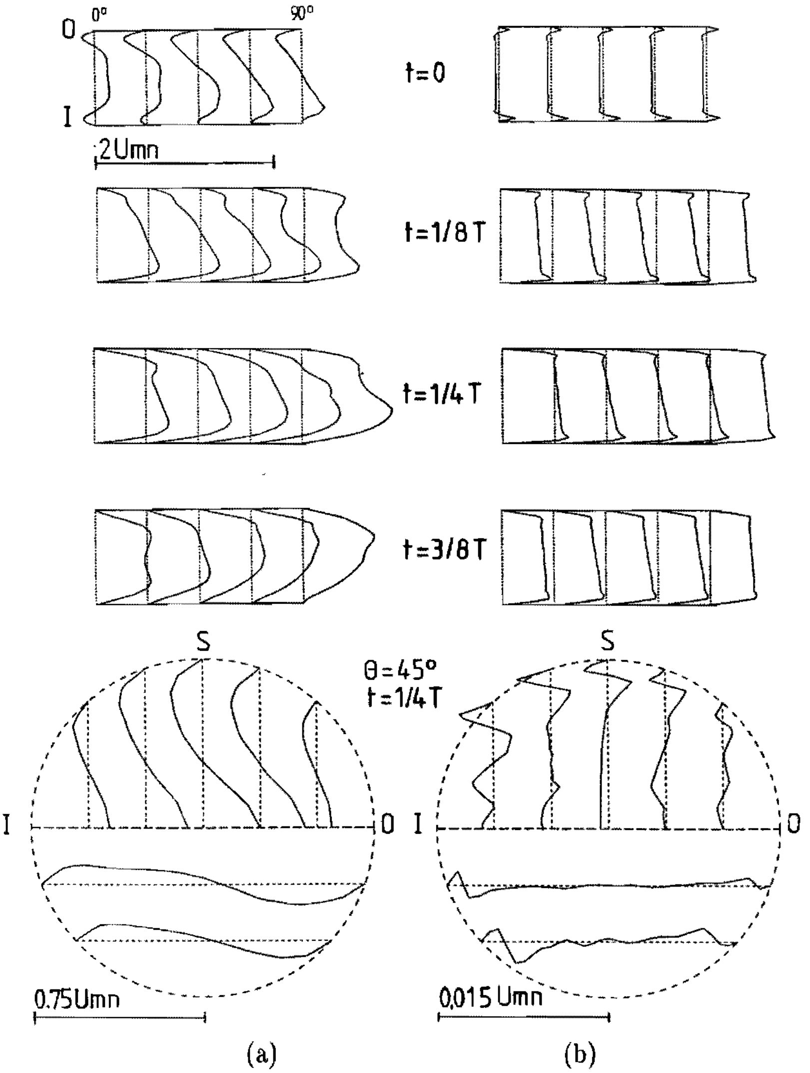

Figure 5.27: Axial velocities in the plane of symmetry and secondary velocities halfway the curved tube at peak flow rate for the oscillating flow cases 5 (a) and 6 (b). U_{mn} stands for the time—averaged mean axial velocity for the pulsating flow cases.

5.4.3 Quantitative comparison between the various flow cases

A quantitative comparison of axial and secondary flow for the flow cases studied is performed by its first moment of axial flow, the axial vorticity of the central core and the axial vorticity at a radius of 4/5 times the radius of the tube. In the definition of the axial vorticity (eq. 5.2) for all flow cases the time–averaged mean axial velocity for the reference flow case was substituted for U_{mn}. In figure 5.28 the first moment of axial flow is presented at θ=22.5° and 67.5° as function of time for the flow cases 1 to 3 and for the flow cases 1 and 4 compared with the steady flow case, as presented in section 5.2.

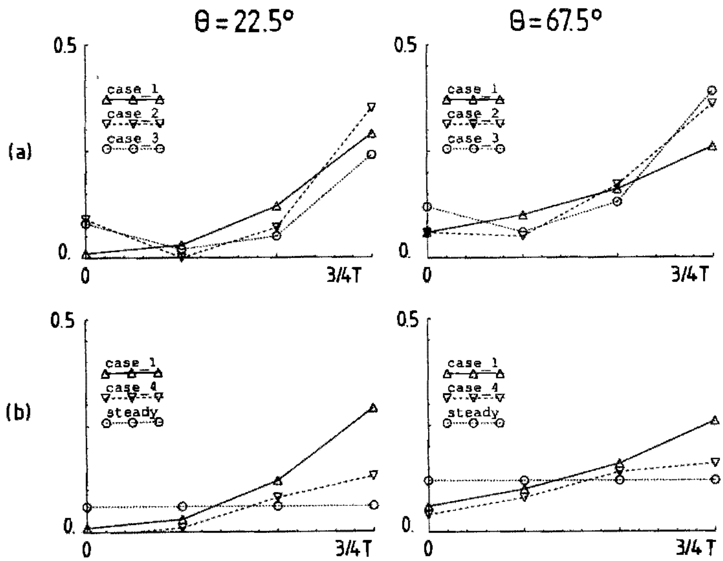

Figure 5.28: First moment of axial flow at two positions in the curved tube as function of time for the flow cases 1 to 3 (a) and the flow cases 1, 4 and the steady flow case (b).

From this figure it can be concluded that for all flow cases the highest value of <X/a> is found at minimal flow rate for both positions θ=22.5° and 67.5°. The values of <X/a> for the flow cases 1 to 3 are relatively close at all time intervals. Also the values of <X/a> at θ=22.5° and 67.5° are quite the same. Apparently the frequency parameter hardly affects the shift of axial flow towards the outer wall in case a steady flow component is present. It must be kept in mind, however, that the first moment of axial flow is rather insensitive to differences in, for example, the C–shaped curvatures of the axial isovelocity lines. The first moment of axial flow for the physiological wave form is in rather good agreement with the value for the reference flow case at t=0, 1/4T and 1/2T at both positions θ=22.5^{o} and 67.5^{o} and shows a relatively large difference at t=3/4T. Probably, this is due to the difference in the Reynolds number at this time interval for both flow cases. The value of <X/a> for the reference flow case is in rather good agreement with the value for steady flow at t=0, 1/4T and 1/2T.

The axial vorticity of the central core as function of time is presented in figure 5.29. For the axial vorticities also a comparison is made between the oscillating and pulsating flow cases at α=7.8 and 24.7. For all pulsating flow rates the axial vorticity at θ=22.5^{o} is maximal halfway the deceleration phase at t=1/2T. The values at peak flow rate, however, are about the same. For flow case 3 the axial vorticity is about constant for the whole period of time. At θ=67.5^{o} the values of the axial vorticities are smaller than the values at θ=22.5^{o}. At peak flow rate for flow case 1 a maximum is observed, whereas for flow case 2 a minimum is found at this time interval. The minimum for the latter flow case is caused by the Lyne type structures in the secondary flow field at t=1/4T. Again, the axial vorticity for flow case 3 is about constant for the whole period of time. This suggests that the secondary flow field for higher frequencies is dominated by the steady flow component. This supposition is supported by the fact that the values of ξ_c for flow case 3 are in good agreement with the values of this quantity for steady flow.

A comparison between the reference flow case and the physiological flow wave reveals a good agreement at all time intervals, suggesting that the influence of the diastolic phase is of minor importance for the secondary flow field in the systolic phase. The values of ξ_c for the steady flow case at θ=22.5^{o} are in rather good agreement with the values for the reference flow case at t=1/4T and 1/2T. At θ=67.5^{o} this is only valid halfway the deceleration phase at t=1/2T.

The axial vorticity of the central core for an oscillating flow rate at α=7.8 shows a large minimum for t=1/2T at θ=22.5^{o}. The reason for this phenomenon is not yet understood. The values of ξ_c are smaller than the values of this quantity for the reference flow case for the whole period of time due to the smaller Reynolds number. This is not valid, however, at θ=67.5^{o} due to the 'tail'–formation in the secondary flow field for the pulsating flow case. The axial vorticity of the central

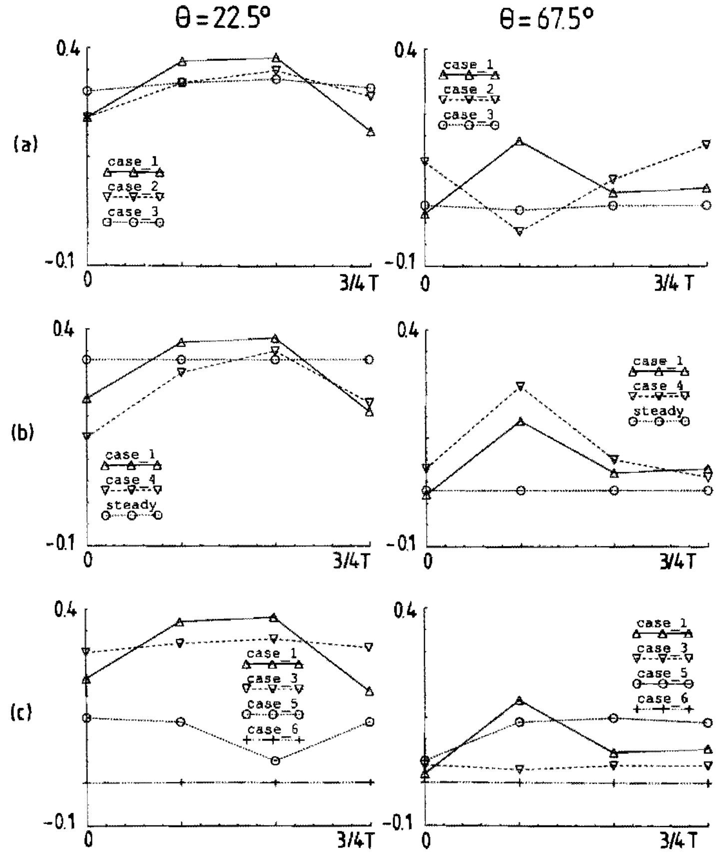

Figure 5.29: **Axial vorticity of the central core at two positions in the curved tube as function of time for the flow cases 1 to 3 (a), for the flow cases 1,4 and the steady flow case (b) and for the oscillating and pulsating flow cases at α=7.8 and 24.7 (c).**

core for an oscillating flow rate at α=24.7 is almost zero and slightly negative at all time intervals, due to the Lyne type secondary flow field occurring. The velocities in the central core for such kind of secondary flow fields are low, as compared to the secondary velocities for Dean type vortices.

At last it should be mentioned that a comparison of the first moment of axial flow and the axial vorticity of the central core between the reference flow case and the steady flow case, reveals a good agreement at peak flow rate and halfway the deceleration phase. Except at θ=67.5° relatively large differences occur in ξ_c at peak flow rate. These features were also observed from a qualitative comparison between the two flow cases. A presentation of ξ_s will not be given in the present study because these diagrams are quite similar to the diagrams presented in figure 5.29, except that the values of ξ_s are two to three times larger than the values of ξ_c.

Concluding discussion

– *General description of the flow field*

For steady entrance flow in a 90–degree curved tube (Re=700, δ=1/6) a shift of the maximum of axial velocity towards the outer wall occurs due to centrifugal forces. The observed C–shaped axial isovelocity lines and the axial velocity plateaus near the inner bend, downstream in the curved tube, are caused by a Dean type secondary flow, directed outward near the plane of symmetry and directed inward near the side wall. Downstream in the curved tube 'tail'–formation occurs in the secondary flow field, possibly caused by the fact that fluid particles with relative low axial and secondary velocities near the center of the tube are not able to penetrate into the region with high axial velocities near the outer wall.

For a fluid flow with a sinusoidally varying Reynolds number between 200 and 800 and a Womersley parameter of 7.8, the maximum of axial velocity shifts towards the outer wall at all time intervals. Near the inner wall regions with reversed axial flow are found halfway the deceleration phase (t=1/2T) and at minimal flow rate (t=3/4T). Halfway the curved tube, at θ=45°, also a reversed axial flow region is situated at the center of the tube at minimal flow rate (t=3/4T). From θ=45° towards θ=90° the axial isovelocity lines show C–shaped contours at maximal flow rate (t=1/4T), which intensify in the deceleration phase. These C–shaped contours are caused by secondary flow, which on its turn is induced by centrifugal effects. The secondary flow field is directed from the inner wall towards the outer wall near the plane of symmetry and circumferentially back near the side wall of the curved tube, transporting fluid particles with high axial velocities from the outer bend towards the inner bend. Due to viscous forces the velocity of these particles is lowered. Near the plane of symmetry secondary flow transports particles with relatively low axial velocities from the inner bend towards the center of the tube, resulting in axial velocity plateaus at the inner half of the cross–sectional plane. At all positions the highest secondary velocities occur at peak flow rate, but also halfway the deceleration phase these velocities are high. As for steady flow, in the downstream end of the curved tube the secondary flow field shows 'tail'–formation in the deceleration phase, which is best visible at t=1/2T. At the entrance of the curved tube the secondary velocities are directed from the outer wall towards the inner wall, pointing at upstream influences of the tube. A qualitative and quantitative comparison with the results of steady flow, shows a surprising resemblance between the axial and secondary flow fields halfway the deceleration phase (t=1/2T).

– *Influence of parameters*

An increase of the Womersley parameter appears to have almost no effect on the shift of the maximum of axial velocity towards the outer wall as well as on the axial velocity gradients at this wall. The axial velocity gradients at the inner wall, however, increase considerably with increasing Womersley parameter. Also large differences are observed in the regions with reversed axial flow which have extended towards the upper side wall at higher frequencies. It is likely that these differences in the upstream region of the curved tube are a consequence of the difference in the prescribed axial flow field at the inlet. There, a fully developed unsteady pipe flow is assumed, consisting of a Womersley profile for the axial component, being strongly dependent on the Womersley number, superimposed on a Poiseuille profile. Generally spoken, the secondary flow field under pulsatile flow conditions resembles a Dean type vortex. Only for α=15, at θ=67.5° and at peak flow rate, small regions near the plane of symmetry are found with secondary velocities directed towards the inner bend, pointing to the formation of a Lyne type secondary flow field. Probably, full development of this Lyne type secondary flow field is prohibited by the much higher secondary velocities resulting from the steady flow component. For α=24.7 the secondary flow field is almost constant in time at both positions θ=22.5° and 67.5°. A qualitative and quantitative comparison of the secondary flow field with that found for the steady flow case, reveals a good agreement. Therefore, it is presumed that secondary flow at higher frequencies is highly determined by the steady flow component.

A comparison of the axial flow field for the physiological flow pulse with the axial flow field for the sinusoidally varying flow rate with a Womersley parameter of 7.8 reveals a good resemblance between the two flow cases. The main differences are found in the absence of axial flow reversal for the physiological flow pulse. This is probably caused by the fact that the Reynolds number at minimal flow rate for this case is equal to 265 instead of 200 for the sinusoidally varying flow pulse. The secondary flow fields, however, show a great resemblance. Only halfway the acceleration phase small differences are found. This supports the idea that the diastolic phase is only of minor importance for the systolic phase.

To study the influence of the steady flow component on axial and secondary flow, oscillating flow was studied at Womersley parameters of 7.8 and 24.7 and compared to pulsating flow. This comparison reveals that for oscillating flow at α=7.8 the secondary flow fields at θ=22.5°, 45° and 67.5° are pure Dean type vortices with a slightly varying vortex strength. The irregularities in the profiles of the secondary velocities in the plane of symmetry, as observed for the pulsating flow case due to 'tail'–formation in the secondary flow field, are not present in the oscillating flow case, for which these profiles are about symmetric around the center of the tube and have a much smoother appearance. For oscillating flow at a Womersley parameter of 24.7 the secondary velocities are about 50 times lower as those for the pulsating flow case. Near the plane of symmetry and in a small layer near the side wall the secondary velocities are directed towards the inner bend, whereas in a small layer within these two regions, secondary flow is directed towards the outer wall. This confirms the analytically predicted change in the secondary flow field, due to the restricted influence of viscous effects, which for α>13 results in a Lyne type secondary flow. However, the element division in the axial direction near the entrance of the curved tube is probably too coarse to predict adequately the rapid development of this secondary flow, which may cause the oscillations observed. Axial flow in the plane of symmetry shows for both oscillating flow cases a shift of the maximum of axial velocity towards the inner wall, in contrast with a shift towards the outer wall as found for both pulsating flow cases. It is likely that this is due to the differences in the axial velocity profiles prescribed at the inlet, which are more uniform for the oscillating flow cases than for the pulsating flow cases.

– *Comparison with experiments*

For the steady flow case comparison of the axial and secondary velocities determined by the numerical model with those obtained from laser Doppler velocity measurements reveals a good agreement. The largest differences are found in the secondary velocities near the side wall, which are lower in the experiments. This discrepancy is also found in the smaller values of the maximal axial vorticity for the measurements. Probably, these differences are caused by measuring problems near the side wall of the curved tube.

Also for the reference flow case (α=7.8, 200<Re<800, sinusoidally varying flow rate), the numerical and experimental data show a good agreement. The largest differences in the axial flow field occur near the inner bend of the tube, where no reversed axial flow is found in the experimental case, whereas regions with axial flow reversal are predicted by the numerical model halfway the deceleration phase and at minimal flow rate. These regions with reversed axial flow cause larger values of $<X/a>$ for the calculations at the end of the deceleration phase. It is likely that the absence of axial flow reversal in the experiments is caused by the larger Reynolds number at minimal flow rate, as compared to the one used for the calculations. The largest differences in the secondary flow field are found in the secondary velocities near the side wall, whereas the secondary velocities in the plane of symmetry are in good agreement with each other. This is also expressed by the values of ξ_c, which are in relative good agreement, and the values of ξ_s, which show large differences in the deceleration phase halfway the curved tube. The reason for this discrepancy has to be sought in the finite dimensions of the measuring volume, the steep velocity gradients at the wall, the differences in the Reynolds numbers at the time intervals presented and positioning errors of the measuring volume. Besides, numerical oscillations occur in the secondary flow field at the entrance of the curved tube. These oscillations are possibly caused by a too short inlet section or a too coarse element division in the axial direction. A calculation of the velocity field in a curved tube with a smaller entrance length showed larger oscillations in the secondary flow field. The solution more downstream in the curved tube, however was not affected.

Finally, the numerical results for the cases of oscillating and pulsating flow rates were confronted to experiments. The experimentally measured and numerically determined secondary velocities in the plane of symmetry and along a line perpendicular to this plane, show a good qualitative agreement. The relatively large differences between the experimental and numerical data are mainly induced by the fact that the secondary velocities, especially for the oscillating flow cases, are small, as compared to the axial velocities, through which small errors in the adjustment of the laser Doppler equipment result in relatively large detection errors of these velocities. The observed oscillations in the numerical solution for the oscillating flow case at α=24.7 are probably caused by a too coarse element division in this region.

– *Comparison to literature*

A comparison of the results obtained in the present study with those reported in literature is difficult to perform, because most studies are dealing with fully developed flows, which is probably only valid for the oscillating flow case at a Womersley parameter of 24.7. Studies dealing with unsteady entrance flow in curved tubes are mostly performed under totally different flow conditions. Nevertheless, a comparison is being made with the results of laser Doppler velocity measurements performed by Talbot and Gong (1983). In their first experiment axial and secondary flow were measured in a 180–degree curved tube with a curvature ratio of 1/20. The Dean number varied sinusoidally between 80 and 160 ($360<Re<720$) at a Womersley parameter of 8.0. At all positions and time intervals they observed a Dean type secondary flow field. The plots of the profiles of the secondary velocity component parallel to the plane of symmetry do not suggest that 'tail'–formation occurred in the secondary flow field, as observed in the present study for the reference flow case. For all time intervals the maximum of axial velocity shifted towards the outer wall. The C–shaped curvatures in the axial velocity contours, however, were not or slightly present. In their second experiment fluid flow was investigated in a curved tube with a curvature ratio of 1/7 for a sinusoidally varying flow rate at $\alpha=12.5$ ($0<\kappa<744$; $0<Re<1970$). Especially at peak volume flow and halfway the deceleration phase, complicated secondary flow fields were observed at $\theta=60^{\circ}$ and 110° with two regions where secondary flow was directed towards the outer wall and two regions where secondary flow was directed towards the inner wall. These secondary flow fields are quite similar to the secondary flow field which occurs in the present study for the pulsating flow case at $\alpha=15$, $\theta=67.5^{\circ}$ and $t=1/4T$. In the second experiment of Talbot and Gong (1983) C–shaped axial velocity contours were observed downstream in the curved tube for all time intervals, except just before peak flow rate. The curvature of these C–shaped contours, however, was less pronounced as found in the present study. Finally, they observed large regions with reversed axial flow near the inner bend. These regions are clearly due to the zero minimal flow rate.

Munson (1975) visualized for a range of Womersley parameters ($0.7<\alpha<32$) fully developed unsteady flow in a 360–degree curved tube with a curvature ratio equal to 0.072. In these experiments the secondary velocity component parallel to the plane of symmetry in the center of the tube was measured as function of α. It was found that for values of α larger than 13 this secondary velocity component was directed towards the inner wall (Lyne type secondary flow field), whereas for values of α smaller than 13 this secondary velocity component was directed towards the outer wall (Dean type secondary flow field). The value of the outward directed component was large, as compared to the value of the inward directed component. Munson (1975) defined a time–averaged dimensionless quantity of this secondary velocity component, which was found to be 0.35×10^{-2} for α=7.8 and -0.15×10^{-3} for α=24.7. These values are 1.40×10^{-2} and -0.05×10^{-3}, respectively, at θ=45° for the oscillating flow cases, as investigated in the present study. It is observed that the value of this quantity is indeed much smaller for α=24.7 than for α=7.8 and that opposite velocity directions are found. The relatively large difference with the value found by Munson (1975) for α=7.8 is probably caused by the fact that fluid flow at θ=45° was not yet fully developed in our experiment.

A shift of the maximum of axial velocity towards the inner wall is many times reported in literature for steady entrance flow in a curved tube with a uniform inlet profile. Olson (1971) studied steady entrance flow in tubes with curvature ratios of 1/4.66 and 1/16. The Dean number varied between 45 and 800 and parabolic and uniform inlet profiles were employed. For the parabolic inlet profiles the maximum of axial velocity immediately shifted towards the outer wall, whereas for the uniform inlet profiles this maximum was situated near the inner wall in a region close to the inlet and shifted towards the outer wall downstream in the curved tube. Also Agrawal et al. (1978) observed an initial shift of the axial velocity maximum towards the inner wall when a uniform inlet profile was applied. In their laser Doppler experiments fluid flow in a curved tube (δ=1/7) was analyzed at a Dean number of 183. Singh et al. (1978) performed an analytical study on pulsatile entrance flow in a curved tube using uniform inlet profiles. The pulsatile wave form consisted of a sinusoidally varying unsteady flow component superimposed on a steady flow component. Higher axial velocities near the inner bend were observed, as compared to the axial velocities near the outer bend, for axial distances to the entrance of the tube smaller than two times the radius. This all supports our findings in the oscillating flow cases, where an axial velocity profile at the inlet is prescribed which is rather uniform.

Mullin and Greated (1980) used laser Doppler anemometry for their axial velocity measurements in the plane of symmetry of a 180–degree curved tube with a curvature ratio of 1/7. The Dean number varied sinusoidally between –65 and 65

($-172<Re<172$) at a Womersley parameter of 4.36. Halfway the acceleration phase they measured a strong upstream influence of the curved tube at the entrance of the bend, resulting in a shift of the maximum of axial velocity towards the inner wall. According to Mullin and Greated (1980), secondary flow did not play an important role at this stage and, therefore, the maximum of axial velocity remained at the inside of the bend at all axial positions in the curved tube. At the onset of the deceleration phase, however, the maximum of axial velocity shifted towards the outer wall at all axial positions. This differs from the findings observed in the present study at a higher Reynolds and Womersley number, where the maximum of axial velocity is situated near the inner bend at all axial positions at peak flow rate for both oscillating flow cases. However, for $\alpha=7.8$ just after the onset of the deceleration phase also a shift of the maximum of axial velocity is found towards the outer wall downstream in the curved tube.

6 Steady flow in a 3D–model of the carotid artery bifurcation

6.1 Introduction

From the results of steady and unsteady entrance flow in a 90–degree curved tube, presented in the previous chapter, it can be concluded that steady flow calculations may supply important information of the flow phenomena occurring in the deceleration phase of systole. Besides, it appeared that fluid flow in a 90–degree curved tube is almost steady at the end of diastole. In this chapter a finite element approximation of steady flow in a rigid three–dimensional model of the carotid artery bifurcation is presented at a Reynolds number of 640 and a flow division ratio of about 50/50, simulating peak systolic blood flow. The numerical results of axial and secondary flow are compared with those obtained from laser Doppler velocity measurements. Also the influence of the Reynolds number, the flow division ratio and the bifurcation angle on axial and secondary flow in the carotid sinus is studied.

Up to now only calculations of fluid flow in two–dimensional models of a bifurcation (Fernandez et al.; 1976, Rindt et al., 1987) or in a simplified three–dimensional model (Wille, 1984) have been presented, the latter dealing with an unphysiologically low Reynolds number of 10. The use of two–dimensional or simplified three–dimensional models of the more complicated in vivo situation can be explained by the rather complex geometry of a bifurcation, which is hard to divide into elements for the three–dimensional situation, and the relatively large computing times needed to solve the system of equations resulting from a three–dimensional analysis. Rindt et al. (1987) performed an experimental study on steady and unsteady flow in a two–dimensional model of the carotid artery bifurcation. A laser Doppler technique was used to investigate axial flow at various sites in the main branch and both daughter branches. Bharadvaj et al. (1982) employed laser Doppler anemometry to study steady flow in a three–dimensional model of the carotid artery bifurcation. For various Reynolds numbers and flow division ratios axial velocity measurements in the plane of symmetry were performed. To gain more insight into the total flow field occurring, also limited axial and secondary velocity measurements were performed out of the plane of symmetry. Finally, Ku and Giddens (1983) studied unsteady flow in a three–dimensional model of the carotid artery bifurcation under physiological flow conditions using laser Doppler anemometry.

In section 6.2 the numerical results are presented of a steady velocity calculation at a Reynolds number of 640 and a flow division ratio of about 50/50, simulating peak systolic blood flow. To validate the numerical model a qualitative and quantitative comparison is made between the numerically predicted velocities and those obtained from laser Doppler velocity measurements (Rindt et al., 1988).

In vivo flow rate measurements reveal that the Reynolds number and the flow division ratio over the daughter branches vary considerably during a flow cycle. Therefore, the influence of the Reynolds number and the flow division ratio on both axial and secondary flow in the carotid sinus is studied. The present study deals with steady flow and only one parameter will be varied at the same time. Nevertheless, it is believed that such a parameter study supplies important information how axial and secondary flow depend on the Reynolds number and the flow division ratio. Besides, the influence of a smaller bifurcation angle is investigated. The results of this parameter study are presented in section 6.3, where a qualitative and quantitative comparison is made with axial and secondary flow in the carotid sinus under systolic flow conditions, as shown in section 6.2.

Finally, in section 6.4 the results are discussed and compared with data available in literature.

6.2 Steady flow under systolic flow conditions

6.2.1 Introduction

In this section the results of a finite element calculation of steady flow at a Reynolds number of 640 and a flow division ratio of about 50/50 are discussed. The definition of the Reynolds number is based upon the diameter of and the mean axial velocity in the main branch of the carotid artery bifurcation. To equalize the flow division ratio for the numerical case to that for the experimental case (52% through the internal carotid artery), the length of the internal carotid artery was chosen to be 10 times the diameter of the main branch.

For division of the carotid artery bifurcation into elements, the mesh generator was used, as described in section 3.7. Figure 6.1 shows a hidden line plot of this element division, which consists of 1474 elements and 14019 nodes. Further refinement of this element division was not possible due to the limited capacity of the computer used. From a comparison of the numerical results with experimental data, however, it can be concluded that the element division as presented in figure

6.1, is suitable to accurately describe axial and secondary flow. The boundary conditions were the same as applied to the steady flow problem in a 90–degree curved tube, i.e. a parabolic axial flow field and zero tangential velocities at the entrance of the common carotid artery, zero velocity components at the side wall of the bifurcation, zero normal and tangential stresses at the end of both daughter branches and zero tangential stress components and a zero velocity component in the plane of symmetry.

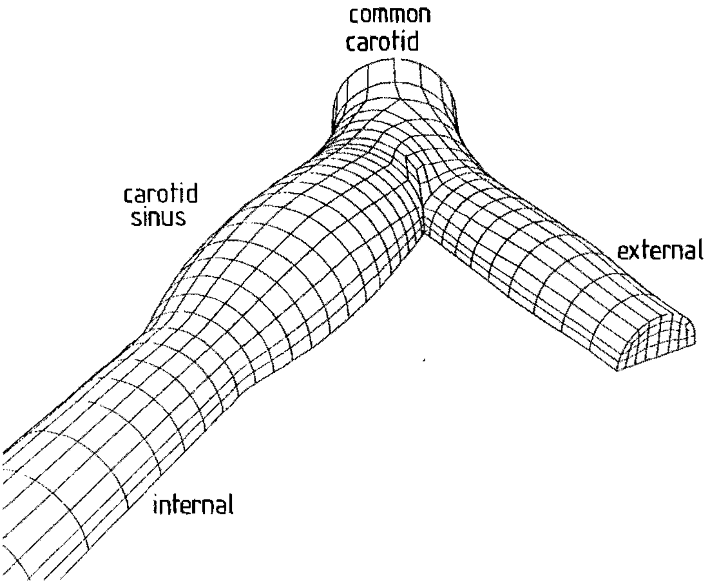

Figure 6.1: Element division for the carotid artery bifurcation.

In the first iteration the Stokes–solution was used as initial guess for the Navier–Stokes problem at a Reynolds number of 150. After convergence the Reynolds number was enlarged to 300, to 470 and, finally, to 640. For convergence at the latter Reynolds number the maximal difference between the velocity components of two successive iterations had to be of $O(10^{-4})$. To that end in total 18 iterations were needed.

For the mesh as shown in figure 6.1, one iteration on a Convex–c1xp took about one hour of computing time. The total computing time could be reduced by using interpolation of the solution from a coarse to a fine mesh. First, the problem was solved using a coarse element division for which one iteration took about one quarter of an hour computing time. At the Reynolds number of interest the solution was interpolated to the fine element division, and several more iterations were performed until convergence was reached. This method reduced the total computing time with a factor 2 to about 10 hours.

6.2.2 Description of the flow field

For presentation of the flow field the cross–sections are considered as given in figure 6.2. One cross–section is positioned in the main branch just before the bifurcation region, 2 cross–sections are located in the external carotid artery and 3 cross–sections in the carotid sinus.

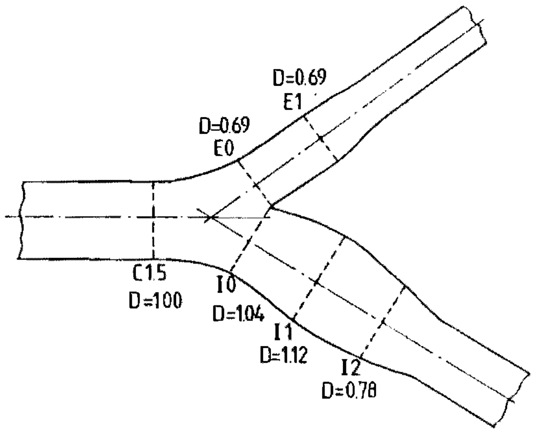

Figure 6.2: Cross–sections at which results are presented. The characters C, I and E refer to common, internal and external carotid artery and the numbers to axial distances to the flow divider, expressed in diameters of the main branch.

In the figures 6.3a and 6.3b axial flow is presented by means of axial isovelocity lines and secondary flow is visualized by means of velocity vectors. Contour level 0 corresponds with zero axial velocity and level 10 with maximal axial velocity at the entrance of the common carotid artery. The secondary velocities in the main branch are scaled up 10 times with respect to the other levels.

At the entrance of the common carotid artery (C1.5) the axial flow field hardly differs from a parabolic flow field. Secondary flow at this site is completely directed from the internal side, the side of the internal carotid artery, towards the external side, pointing at upstream influences due to flow branching. These

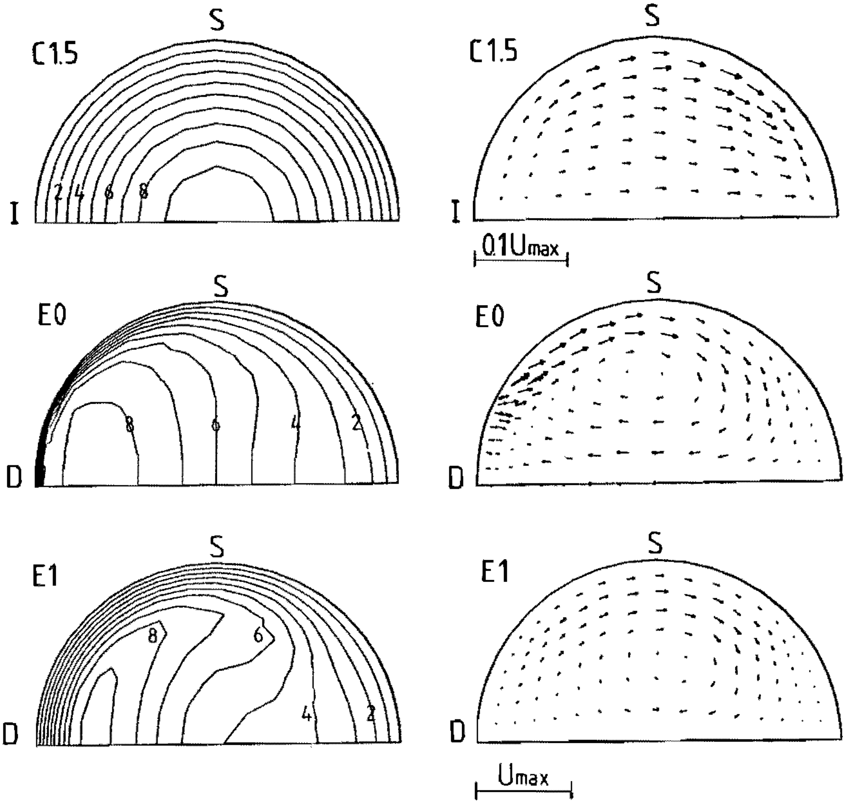

Figure 6.3a: Axial flow and secondary flow in the main branch and the external carotid artery (I: internal carotid artery side, D: divider wall, S: side wall).

secondary velocities result in a larger flow rate through the external carotid artery than expected on the basis of the geometry alone. The secondary velocities at the external side are somewhat higher than the secondary velocities at the internal side.

At the entrance of the internal carotid artery (I0) high axial velocities are found near the divider wall, which is primarily caused by flow branching. A region with negative axial velocities with a diameter of about 30% of the local diameter of the bulb is seen opposite to the flow divider. Secondary flow at this site is almost entirely directed towards the divider wall except in a small region near the side wall, where secondary flow is directed towards the non–divider wall. The highest secondary velocities are found near the flow divider. When axial flow is defined as

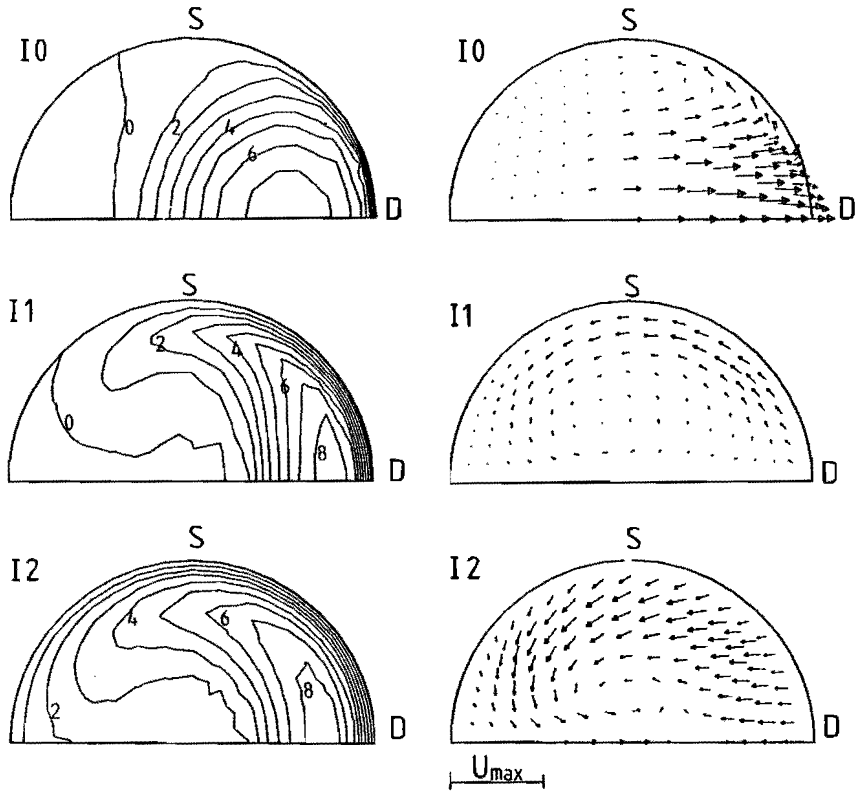

Figure 6.3b: Axial flow and secondary flow in the carotid sinus (D: divider wall, S: side wall).

the velocity component parallel to the axis of the common carotid artery and secondary flow as the velocities perpendicular to this axis, it is found that secondary flow at the entrance of the bulb is almost zero over the whole cross–sectional plane except for a small region along the side wall. In this region secondary flow is directed towards the non–divider wall. These findings indicate that the main flow direction at the entrance of the internal carotid artery is still parallel to the axis of the main branch.

Halfway the bulb (I1) the geometry of the region with negative axial velocities has enlarged to a diameter of about 60% of the local bulb diameter in the plane of symmetry. In the direction perpendicular to the plane of symmetry, however, this region has become smaller. The maximum of axial velocity is shifted towards the divider wall, as compared to the maximum of axial velocity at the entrance of the carotid sinus, and the low–numbered axial velocity contours show C–shaped curvatures. All these effects are strongly related to secondary flow at this site, which shows high resemblance with a Dean type vortex. Near the plane of symmetry the secondary velocities are directed towards the divider wall and near the side wall they point circumferentially back towards the non–divider wall. The highest secondary velocities are observed near the side wall of the branch, but they are considerably lower than the secondary velocities near the flow divider.

At the end of the bulb (I2) no reversed axial flow region is found. High axial velocities are observed near the divider wall and a region with almost equal axial velocities is found near the non–divider wall. The curvature of the axial velocity contours has shifted to the more high–numbered ones. Secondary flow at this site has grown in strength with regard to secondary flow halfway the bulb. Near the non–divider wall secondary flow still shows great resemblance with a Dean type vortex, but near the divider wall all secondary velocities are directed towards the opposite wall. The latter effect originates from the tapering of the bulb near its end, which causes high secondary velocities directed towards the center of the branch in regions with high axial velocities.

In the external carotid artery (fig. 6.3a) no reversed axial flow is found. The highest axial velocities are observed near the divider wall. Downstream in the branch the high–numbered axial isovelocity lines show C–shaped curvatures. At both positions in the external carotid artery the secondary velocities are directed towards the divider wall near the plane of symmetry and circumferentially back near the side wall. Near the flow divider the secondary velocities are directed towards the opposite wall probably due to boundary layer development.

6.2.3 Qualitative comparison with experiments

In figure 6.4a the axial velocity profiles in the plane of symmetry are presented for both the measurements and the calculations. The agreement between the experimental and numerical data is good. The shape of the region with reversed axial flow in the plane of symmetry as well as the axial velocity plateau is estimated well by the numerical model. Downstream in the external carotid artery the numerical velocities are consequently somewhat higher than the experimental ones.

These differences are probably caused by small errors in the adjustment of the flow rate in the experiments.

In the figures 6.4b and 6.4c for both the measurements and the calculations axial velocity contours are shown together with profiles of the secondary velocity components. Again, contour level 0 corresponds to zero axial velocity and level 10 to the maximal axial velocity at the entrance of the main branch. The secondary velocities in the main branch are scaled up 10 times with respect to the other levels. There is a good agreement between the numerically predicted and experimentally measured axial velocities. The largest differences occur at the entrance of the

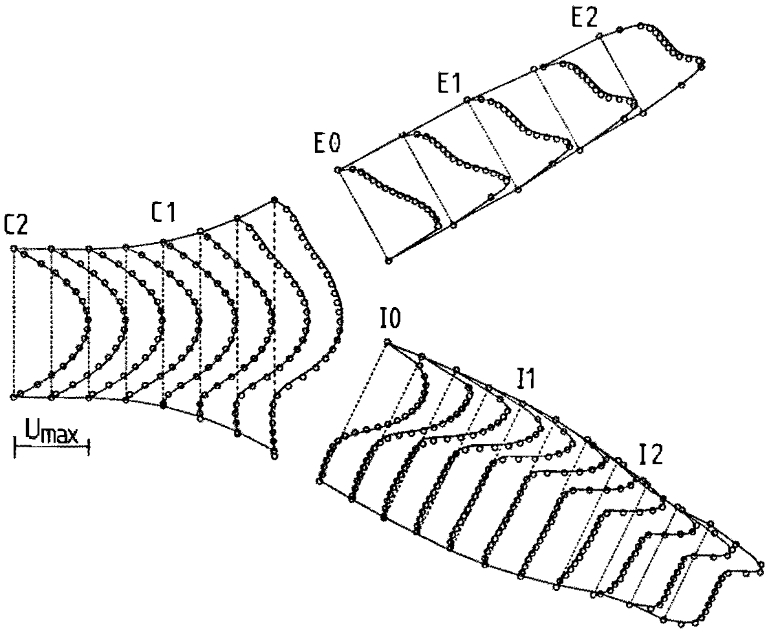

Figure 6.4a: Calculated (——) and measured (ooo) axial velocity profiles in the plane of symmetry.

internal carotid artery with regard to the region with reversed axial flow. Within this region the axial velocities are of the order of 0.05 times U_{max} near the plane of symmetry and 0.001 times U_{max} near the side wall, U_{max} being the maximal axial velocity in the main branch. Therefore, small errors in the axial velocity measurements may cause relatively large differences in the determination of the region with reversed axial flow, while the absolute values of the experimental and

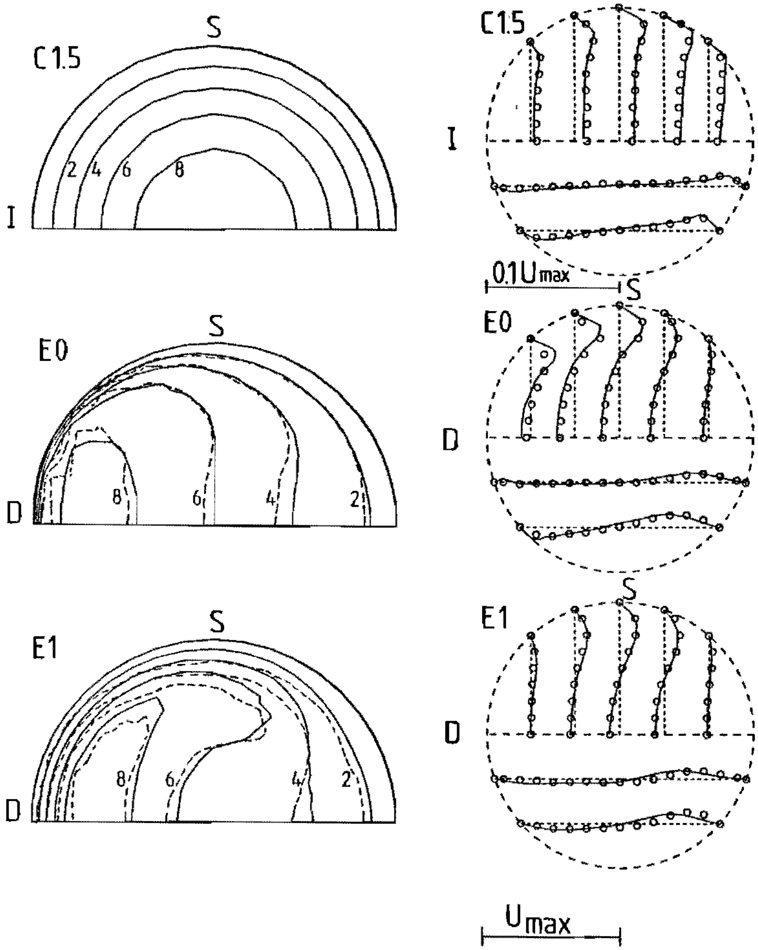

Figure 6.4b: Calculated (——) and measured (— —, ooo) results of axial and secondary flow in the main branch and the external carotid artery.

the numerical velocities are quite the same. Downstream in the external carotid artery the experimental values of axial flow are consequently somewhat lower than the numerical ones. This points at a smaller flow rate at this site for the experiments than for the computations. In table 6.5 the relative flow rates at all the cross–sectional planes are presented. The 95%–confidence intervals for the experiments are estimated to be ±2%. It may be concluded that a correct

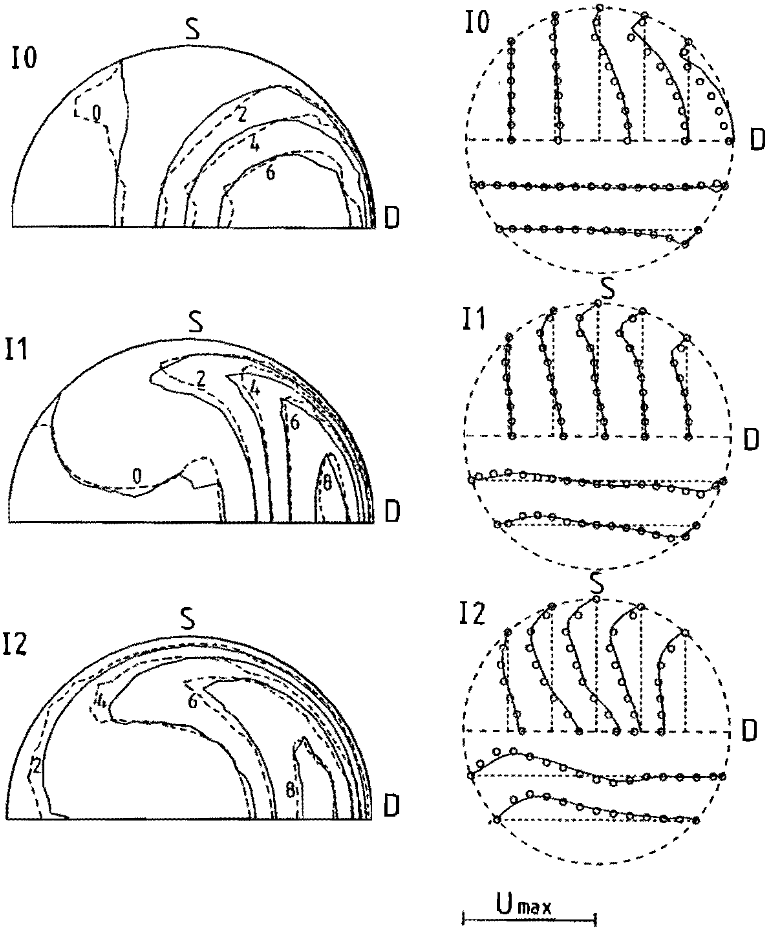

Figure 6.4c: Calculated (——) and measured (— —, ooo) results of Axial and secondary flow in the carotid sinus.

adjustment of the flow rates is achieved at all positions except downstream in the external carotid artery. Here, the experimental flow rate is essentially smaller than the numerical one. This may be caused by an error in the adjustment of the flow rate through the main branch or by an alteration of the flow division ratio during the experiments.

	C1.5	I0	I1	I2	E0	E1
exp	100%	52%	51%	51%	48%	43%
num	100%	52%	52%	52%	48%	48%

Table 6.5: Relative flow rates for the experiments (±2%) and the calculations.

Regarding secondary flow, there is a fair agreement between the numerical and experimental data. The largest differences are found near the flow divider in both daughter branches. This may be caused by numerical errors due to the ill–shaped elements near the flow divider, while also measuring errors due to the presence of the flow divider contribute to this discrepancy.

6.2.4 Quantitative comparison with experiments

A quantitative comparison of the numerical and experimental results of axial flow is performed by its first moment $<X/a>$, as defined in equation 5.1, with a the local radius of the cross–sectional plane. A positive value in the daughter branches means a shift of axial flow towards the divider wall and in the main branch towards the side of the external carotid artery. Table 6.6 gives the experimental and numerical values of $<X/a>$ for the 6 positions analyzed. The 95%–confidence intervals for the experiments are estimated to be ±0.02. The agreement between the experimental and numerical values is satisfactory. At all positions in the daughter branches the axial velocity profile is shifted towards the divider wall. At the entrance of the internal carotid artery and halfway the bulb the first moment of axial flow is large, as compared with its value at the end of the bulb and in the external carotid artery. This is due to the presence of a region with reversed axial flow opposite to the flow divider. In spite of the secondary velocities at C1.5, axial flow at this site seems to be unaffected.

	C1.5	I0	I1	I2	E0	E1
exp	0.01	0.44	0.50	0.15	0.18	0.14
num	0.00	0.42	0.48	0.17	0.18	0.13

Table 6.6: First moment of axial flow for measurements (±0.02) and calculations.

Secondary flow is quantified by the mean axial vorticities ξ_c and ξ_s, as defined by equation 5.2 with a the radius of and U_{mn} the mean axial velocity in the common carotid artery. A negative value of these vorticities means that the vortex is directed clockwise. In table 6.7 the values of ξ_c are presented for both the measurements and the calculations. The 95%–confidence intervals for the experiments are estimated to be ±0.02. The values of ξ_c are in relatively good agreement, except at the entrance of both daughter branches. Probably, these differences are caused by measuring problems due to the presence of the flow divider. The highest value of ξ_c is found at the entrance of the carotid sinus, whereas the lowest value of this quantity in the daughter branches is observed halfway the bulb.

	C1.5	I0	I1	I2	E0	E1
exp	0.02	0.38	0.08	0.10	−0.22	−0.13
num	0.02	0.42	0.07	0.13	−0.30	−0.12

Table 6.7: Axial vorticity of the central core for the experiments (±0.02) and the computations.

	C1.5	I0	I1	I2	E0	E1
exp	−0.03	0.56	0.53	1.17	−1.02	−0.66
num	−0.03	0.50	0.50	1.13	−1.05	−0.68

Table 6.8: Axial vorticity at r=4/5a for the measurements (±0.05) and the calculations.

In table 6.8 the values of ξ_s are shown. The 95%–confidence intervals for this quantity are estimated to be ±0.05. These relatively large confidence intervals are due to positioning errors of the measuring volume near the side wall, where the velocity gradients are often high. From the data presented it can be concluded that the resemblance between the experimental and numerical results is quite satisfactory, in contrast with the findings for steady and unsteady flow in a 90–degree curved tube where the numerical and experimental values of this quantity show relatively large differences (sect. 5.2.4 and 5.3.4). The reason for this is yet unknown. The value of ξ_s at the end of the bulb is large as compared to the other values, especially at the entrance of and halfway the bulb. The relatively high values in the external carotid artery are probably caused by its smaller diameter and the same flow rate, as compared to those in the internal carotid artery.

6.3 Influence of various parameters on axial and secondary flow

Because the Reynolds number and flow division ratio vary essentially during a heart cycle (Ku et al. 1985), one computation was performed at a Reynolds number of 300 and one at a flow division ratio of 63/37, keeping the other flow parameters constant as best as possible. From the data presented in chapter 2 it was concluded that the mean angle between the internal and common carotid artery is probably smaller than the angle proposed by Bharadvaj et al. (1982). Therefore, also a computation was carried out in a model of the bifurcation with an angle of 10^o instead of 25^o. Table 6.9 gives an overview of the calculations performed. The flow division ratio of the Reynolds flow case differs somewhat from that of the reference flow case due to the influence of the Reynolds number on the flow division ratio. The smaller Reynolds number was achieved by increasing the kinematic viscosity. The flow division ratio of 63/37 was achieved by a smaller length of the internal carotid artery (3 diameters), as compared to the length of this branch in the other flow cases (10 diameters). Due to the smaller bifurcation angle for the angle flow case, the geometry of the carotid sinus near its origin is slightly different.

flow case	Reynolds number	flow division ratio	angle
reference	640	52/48	25^o
Reynolds	300	48/52	25^o
flow ratio	640	63/37	25^o
angle	640	52/48	10^o

Table 6.9: Summary of the parameters for the steady flow cases.

In figure 6.10 the influence of the Reynolds number on the velocity profiles in the plane of symmetry and on axial and secondary flow in the carotid sinus is shown. In the plane of symmetry the region with reversed axial flow is somewhat smaller in axial and radial extent for a Reynolds number of 300 than for a Reynolds

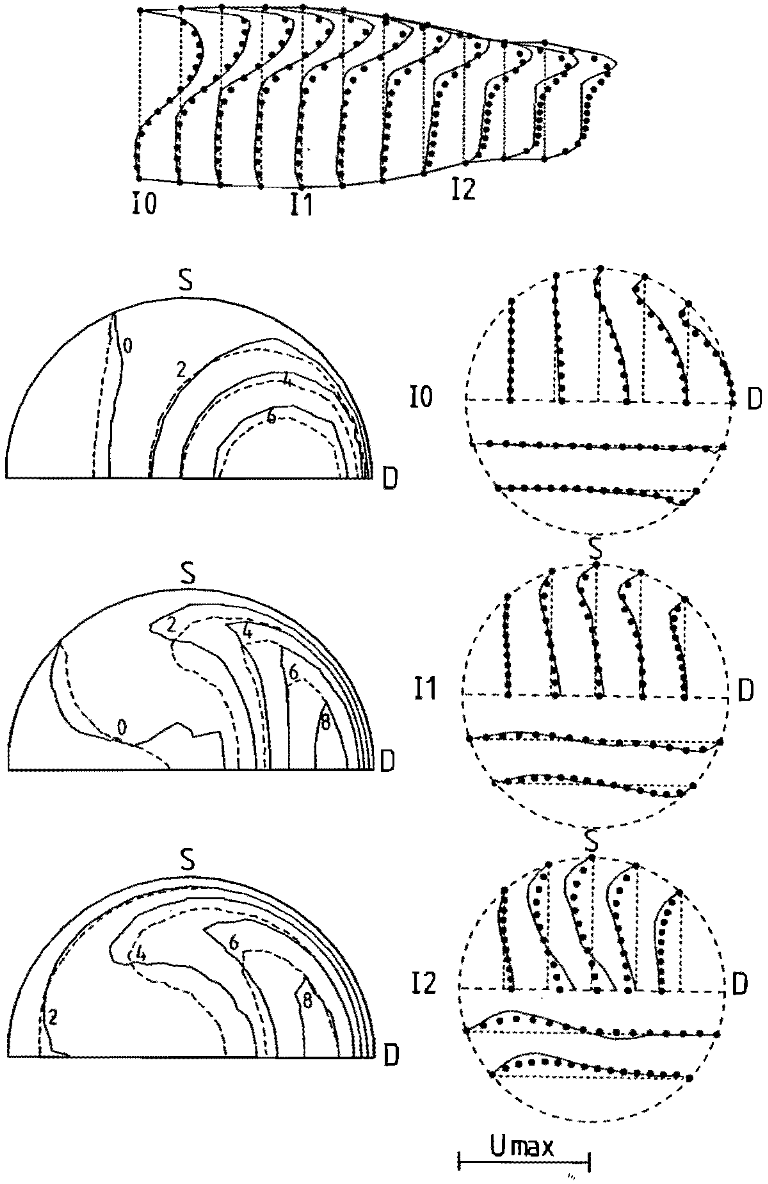

Figure 6.10: Influence of the Reynolds number on axial and secondary flow in the carotid sinus (——: reference case, – –, ●●●: Reynolds case).

number of 640. For the Reynolds flow case it has a maximal diameter of about 50% of the local bulb diameter. The shift of the maximum of axial velocity towards the divider wall and the occurrence of an axial velocity plateau is less pronounced than for the reference flow case. The influence of the Reynolds number on total axial flow is small at the entrance of the bulb and restricted to a smaller zone with reversed axial flow. Halfway and at the end of the carotid sinus the axial velocities are somewhat smaller for the Reynolds flow case than for the reference flow case, also due to the larger flow rate for the latter flow case. The region with reversed axial flow halfway the bulb is essentially smaller in the plane of symmetry and larger in the direction perpendicular to this plane. The C–shaped curvatures of the low–numbered axial velocity contours halfway and at the end of the bulb are less pronounced than for the reference flow case. The influence of the Reynolds number on secondary flow in the carotid sinus is mainly restricted to the end of the bulb, where the secondary velocities are lower for a Reynolds number of 300 than for a Reynolds number of 640, although also halfway the carotid sinus these secondary velocities are somewhat lower. It is likely that these lower secondary velocities result in the less pronounced C–shaped curvatures of the axial velocity contours downstream in the carotid sinus and the different shape of the region with reversed axial flow halfway the bulb.

The influence of the flow division ratio is pointed out in figure 6.11. Surprisingly, the effect of an increasing flow division ratio on the region with reversed axial flow in the plane of symmetry is almost the same as the influence of a decreasing Reynolds number: smaller in axial and radial extent. The shift of the maximal axial velocity towards the divider wall is about the same as for the reference flow case. As visible in the axial isovelocity lines, an increase of the flow division ratio results in higher axial velocities in the internal carotid artery, but the shape of the contours is hardly affected. This is primarily explained by the finding that an increase of the flow rate through the internal carotid artery with about 20% has only little effect on secondary flow in this branch.

A smaller bifurcation angle causes the region with reversed axial flow to grow at the entrance of the bulb (fig. 6.12). This, however, is probably mainly due to the difference in the geometry of the carotid sinus at this site, particularly the increased value of the inlet area. Halfway the bulb this region is somewhat smaller in the plane of symmetry but larger in the direction perpendicular to this plane. For the angle flow case, the C–shaped curvatures of the axial velocity contours are less pronounced than for the reference flow case. The secondary velocities at the

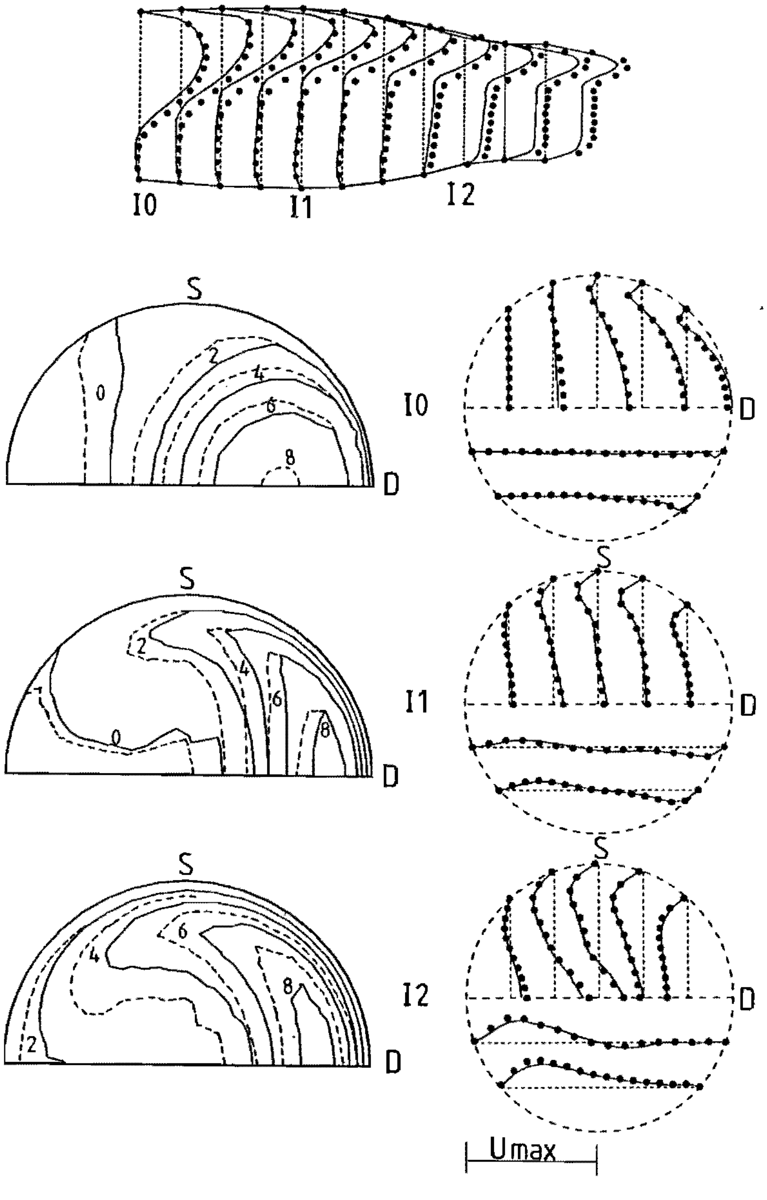

Figure 6.11: Influence of the flow division ratio on axial and secondary flow in the carotid sinus (——: reference case, — —, ●●●: flow ratio case).

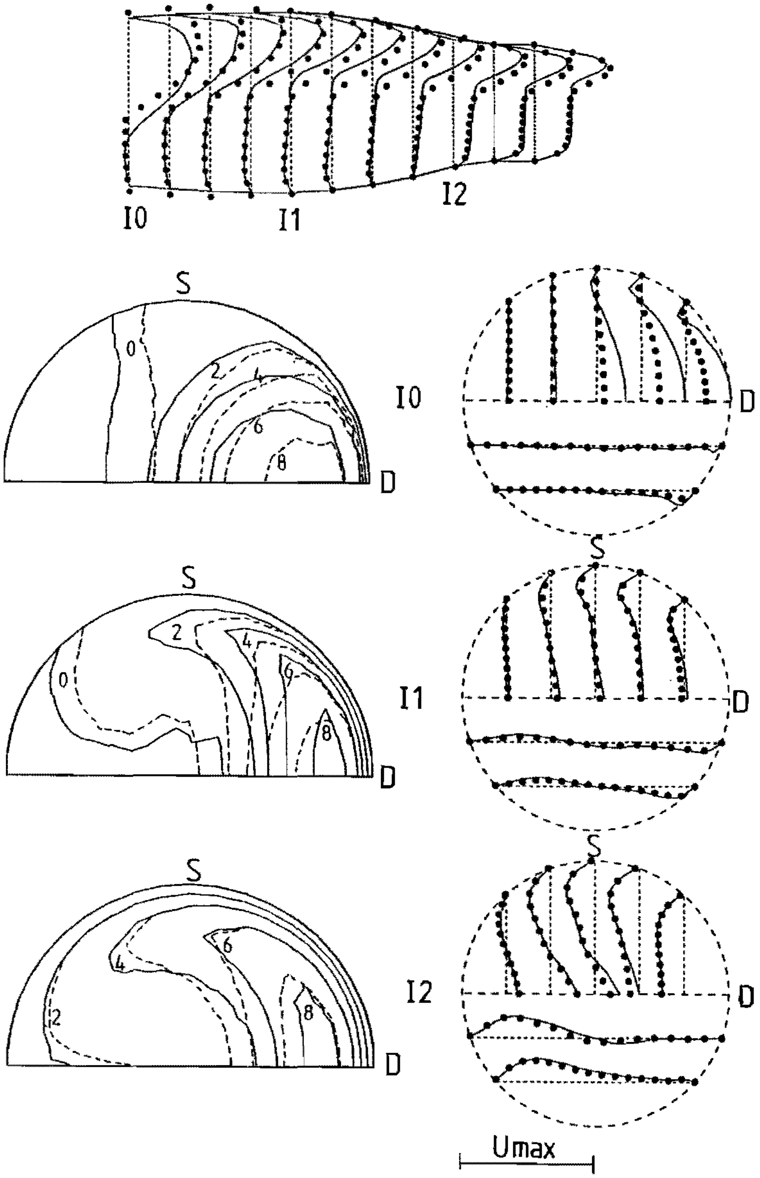

Figure 6.12: Influence of the bifurcation angle on axial and secondary flow in the carotid sinus (——: reference case, — —, ●●●: angle case).

entrance of the bulb decrease with decreasing bifurcation angle, mainly because the main stream velocities at this site are still directed parallel to the axis of the main branch. Halfway and at the end of the bulb the influence on secondary flow is small.

A quantitative comparison between the various flow cases is performed by the first moment of axial flow <X/a> and the axial vorticities ξ_c and ξ_s. These quantities are presented in the figures 6.13a, 6.13b and 6.13c, respectively, as function of the position in the carotid sinus. The values of ξ_c and ξ_s for the Reynolds flow case show differences with the values for the reference flow case at the end of the carotid sinus. These differences are probably due to the fact that the secondary flow field as induced by the centrifugal forces is less developed for lower Reynolds numbers, whereas the secondary flow field resulting from the taper of the carotid sinus, is quite the same. The influence of the flow division ratio on the quantities <X/a>, ξ_c and ξ_s is small, as compared to the values of these quantities

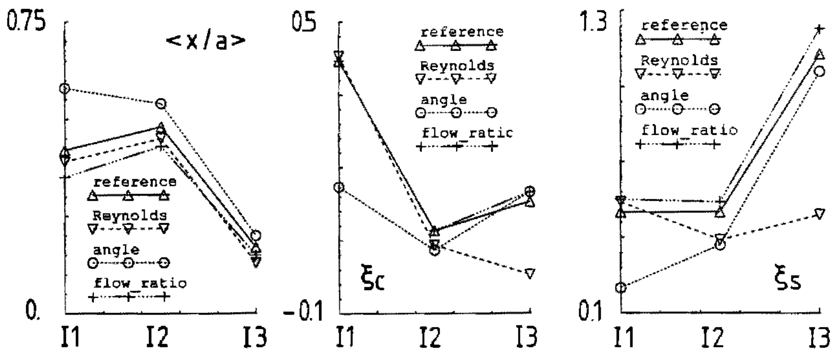

Figure 6.13: First moment of axial flow (a), the axial vorticity of the central core (b) and the axial vorticity at r=4/5a (c) as function of the position in the carotid sinus for the various flow cases.

for the reference flow case. Finally, the values of <X/a>, ξ_c and ξ_s for the angle flow case are quite similar to the values of these quantities for the reference flow case, except at the entrance of the carotid sinus. The larger value of <X/a> at this position for the angle flow case is due to the larger region with reversed axial flow, probably caused by the difference in geometry of the carotid sinus at this site, and the higher axial velocities near the flow divider. The smaller values of ξ_c and ξ_s are a consequence of the fact that at this site the main stream velocities are still directed parallel to the axis of the common carotid artery, resulting in lower secondary velocities, but higher axial velocities, for smaller bifurcation angles.

6.4 Discussion

In this chapter the results of a numerical study on steady flow in rigid 3D–models of the carotid artery bifurcation are presented and compared to laser Doppler velocity measurements performed under the same flow conditions. For a Reynolds number of 640 and a flow division ratio of about 50/50 the axial velocity profiles in both daughter branches of the common carotid artery are skewed towards the divider wall, whereas a region with reversed axial flow is observed in the carotid sinus opposite to the flow divider. The shape of this region in axial and radial direction is largely determined by secondary flow, which on its turn is induced by centrifugal forces. For example, due to secondary flow halfway the carotid sinus the region with negative axial velocities enlarges near the plane of symmetry, whereas this region becomes smaller in the direction perpendicular to the plane of symmetry. The C–shaped axial velocity contours and the axial velocity plateaus downstream in the daughter branches are also caused by secondary flow, which transports fluid particles with high axial velocities situated near the divider wall, towards the non–divider wall. At the entrance of the bulb opposite to the flow divider both axial and secondary velocities are low, whereas at the end of the bulb secondary flow is highly influenced by the tapering of the branch at this site. The influence of the Reynolds number, the flow division ratio and the bifurcation angle are restricted to a relatively small variation in the region with reversed axial flow, more or less pronounced C–shaped curvatures of the axial velocity contours and increasing or decreasing maximal values of axial velocity. The influence of these variations on secondary flow is mainly restricted to the end of the bulb in case of a smaller Reynolds number and to the entrance of the bulb in case of a smaller bifurcation angle.

A qualitative comparison of axial and secondary flow with the laser Doppler velocity measurements reveals that the flow phenomena occurring in the carotid artery bifurcation, are well predicted by the numerical model. Small discrepancies between the axial and secondary flow fields are observed near the flow divider, possibly because of the ill–shaped elements in this region, but also as a consequence of the measuring problems near the flow divider. The discrepancy found regarding the region with reversed axial flow is mainly caused by the relatively large measuring errors due to the low axial velocities in this region. A quantitative comparison between the numerical data and those obtained with the laser Doppler measuring technique is performed regarding the first moment of axial flow and the axial vorticities of secondary flow. Taking into account the 95%–confidence intervals for the experiments, a good agreement is observed between the numerical and experimental values of these quantities.

The flow patterns as observed are in good agreement with those observed by Bharadvaj et al. (1982). They performed laser Doppler measurements of axial and secondary flow at several sites in the bifurcation for various Reynolds numbers and flow division ratios. In the carotid sinus they found a region with reversed axial flow opposite to the flow divider. For a Reynolds number of 800 and a flow division ratio of 70/30 (70% through the carotid sinus) the maximal diameter of this region was about 45% of the local bulb diameter. In the present study the maximal diameter at a Reynolds number of 640 was about 50% of the local bulb diameter at a flow division ratio of 63/37 and about 60% at a flow division ratio of 52/48. They also observed high axial velocities near the divider wall of the carotid sinus and an axial velocity plateau opposite to this wall at the end of the bulb. At the entrance of the bulb they found that secondary flow was almost completely directed towards the flow divider. Halfway the bulb they observed high secondary velocities directed towards the non–divider wall near the side wall and low secondary velocities directed towards the divider wall near the plane of symmetry, resulting in helical patterns of the fluid flow. At the end of the bulb high secondary velocities were found directed towards the non–divider wall near the side wall and directed towards the divider wall near the plane of symmetry. These features are also observed in the present study.

The study of Bharadvaj et al. (1982) also revealed that at a flow division ratio of 70/30 a decrease of the Reynolds number resulted in a reduction of the radial as well as the axial extent of the region with reversed axial flow in the plane of symmetry. The present study reveals that this is also valid for a flow division ratio of about 50/50. One should bear in mind, however, that this does not necessarily hold for the direction perpendicular to the plane of symmetry. At a Reynolds number of 400 they found that in the carotid sinus the region with reversed axial flow became smaller as the flow rate through the internal carotid artery increased. In the present study the same phenomena are observed at a Reynolds number of 640.

Wille (1984) performed a finite element calculation of steady flow in a symmetrical bifurcation at a Reynolds number of 10. Instead of a direct solver, he used a conjugate gradient iteration method. A division of one quadrant of the symmetrical bifurcation into 300 brick elements was performed, which resulted in 5508 unknowns. Computation of the flow field at a Reynolds number of 10 took about two months CPU–time on an unknown computer system. In spite of the low Reynolds number, the results were believed to be representative of the overall flow patterns in human branching systems. He found skewed velocity profiles in the daughter branches. The shear forces were high near the flow divider and relatively low just upstream of the bifurcation. This qualitative finding is in agreement with our results. More important is the achieved speed–up in computing time needed to solve the system of equations.

A quantitative comparison of axial and secondary flow in the carotid sinus with steady flow in a 90–degree curved tube (Re=700, δ=1/6) is difficult to achieve. A qualitative comparison, however, reveals remarkable similarities. Halfway the carotid sinus a Dean type vortex has developed, supporting the statement of Olson (1971) that the flow phenomena in a bifurcation mainly originate from curvature effects. This vortex is still present at the end of the bulb but, due to the tapering geometry of the carotid sinus at this site, secondary velocities directed towards the center of the branch are added. The upstream influence of the carotid artery bifurcation for the reference flow case results in lower secondary velocities in the main branch, as compared to the secondary velocities at the entrance of a 90–degree curved tube. These secondary velocities, however, are highly dependent on the flow division ratio. Secondary flow in the carotid sinus causes, similar to secondary flow in a 90–degree curved tube, C–shaped curvatures of the axial velocity contours halfway and at the end of the carotid sinus. Also, as a consequence of centrifugal forces, a shift of the maximum of axial velocity is observed towards the divider wall. Finally, due to secondary flow axial velocity plateaus near the non–divider wall at the end of the bulb develop. On the contrary to steady flow in a 90–degree curved tube, large regions with reversed axial flow are observed opposite to the flow divider. These negative axial velocities are mainly due to the geometry of the carotid sinus, especially its divergence at the inlet side, and the larger cross–sectional areas of the daughter branches, as compared to the cross–sectional area of the main branch, which both cause a positive pressure gradient in downstream direction.

7 Conclusions

In the present study the finite element method was used to study blood flow in the carotid artery bifurcation. The results were validated with laser Doppler velocity measurements, performed in a transparent rigid–walled model of this bifurcation. Because it is assumed that curvature effects highly influence the flow phenomena occurring in the carotid artery bifurcation, first steady and unsteady entrance flow in a 90–degree curved tube with a curvature ratio of 1/6 was investigated.

The geometry of the bifurcation models used in the present study are based upon data of Balasubramanian (1979), who angiographically determined a mean geometry of the carotid artery bifurcation. From data available in literature and from the results of a cast study, as performed by us, however, it may be concluded that the use of a mean geometry is debatable because of the large interindividual variations. Besides, it appeared that the mean diameter of the main branch and the mean angle between the internal carotid artery, one of the daughter branches, and the main branch are probably smaller as those proposed by Balasubramanian (1979). Therefore, for a complete description of blood flow in the carotid artery bifurcation, the influence of geometry variations on the flow phenomena occurring, have to be taken into account. These influences were partly investigated in the present study.

For spatial discretization of the Navier–Stokes and continuity equations, a standard Galerkin finite element method was employed. The penalty function method was used for elimination of the pressure unknowns from the discretized Navier–Stokes equation and a Newton–Raphson iteration technique for linearization of the discretized convective term. Temporal discretization was achieved by applying the θ–method to the time derivative in the Navier–Stokes equation. It is concluded that the finite element method, as presented, can be used for detailed analysis of incompressible and Newtonian fluid flow in rigid–walled three–dimensional geometries. It was found that with the use of supercomputers and minisupercomputers and a suitable element division and renumbering procedure of the nodal points, the computing times needed can be restricted to reasonable values.

For validation of the numerical results, laser Doppler velocity measurements were performed in perspex models of a 90–degree curved tube and of the carotid artery bifurcation. This non–contact measuring technique has been successfully applied to velocity measurements in up–scaled 2D–models of human arteries (v.d.Vosse et al., 1985; Rindt et al., 1987). In the one–to–one models used in the present study, however, the dimension of the measuring volume is relative large, as compared to the dimensions of the models, introducing errors, especially in regions with high velocity gradients. Besides, due to the finite accuracy of the traversing system, positioning errors of the measuring volume contribute to errors in the measured velocities. Nevertheless, it is believed that the velocity data, as obtained with this measuring technique, can be used for validation of the numerical results.

For steady entrance flow in a 90–degree curved tube (Re=700, δ=1/6) a shift of the maximum of axial velocity towards the outer wall occurs due to centrifugal forces. The observed C–shaped axial isovelocity lines and the axial velocity plateaus near the inner bend, downstream in the curved tube, are caused by a Dean type secondary flow, directed outward near the plane of symmetry and directed inward near the side wall. Downstream in the curved tube 'tail'–formation occurs in the secondary flow field, possibly caused by the fact that fluid particles with relative low axial and secondary velocities near the center of the tube are not able to penetrate into the region with high axial velocities near the outer wall.

For a sinusoidally varying flow rate (200<Re<800, α=7.8) throughout the curved tube a shift of the maximum of axial velocity towards the outer wall was found. In the deceleration phase highly curved axial velocity contours and axial velocity plateaus were observed downstream in the bend. Regions with reversed axial flow were found halfway and at the end of the deceleration phase. The shift of the maximum of axial velocity and the formation of C–shaped axial isovelocity lines and of axial velocity plateaus were highly determined by the secondary flow field. At maximal flow rate this secondary flow field showed great resemblance with a Dean vortex but, especially halfway and at the end of the deceleration phase, a more complicated secondary flow field developed. The flow phenomena occurring halfway the deceleration phase are quite similar to those occurring for steady entrance flow. Qualitative and quantitative comparison of axial and secondary flow with laser Doppler velocity measurements shows a favorable agreement between the numerical and experimental data. The occurring differences can easily be explained by the larger minimal Reynolds number for the experiments and by the measuring errors near the side wall of the curved tube.

To investigate the influence of the Womersley parameter on unsteady flow in a bend, calculations were performed at α=15.0 and 24.7. For both flow cases a similar shift of the maximum of axial velocity towards the outer bend was found. Regarding the regions with axial flow reversal the largest differences occurred near the inner bend. The secondary flow field for α=15.0 showed Lyne type structures at peak flow rate downstream in the curved tube. Secondary flow at α=24.7 was almost constant in time and quite similar to secondary flow, as observed for the steady flow case. Apparently, at higher Womersley parameters the steady flow component is the dominant factor for the secondary flow field. Calculation of fluid flow for a physiologically varying flow rate revealed a good agreement between the flow phenomena occurring in the systolic phase and those for a sinusoidally varying flow rate at α=7.8. This suggests that the influence of the diastolic phase on the flow phenomena occurring in the systolic phase is small. To study the influence of the steady flow component on both axial and secondary flow, calculations were performed with purely oscillating flow rates at α=7.8 and 24.7 ($-300<Re<300$). In contrast with the findings for flow with a steady flow component, for both oscillating flow situations the maximum of axial velocity shifted towards the inner bend, presumably due to the more uniform axial entrance profiles. In accordance with literature, at all time levels secondary flow showed a Dean type vortex for α=7.8 and a Lyne type secondary flow field for α=24.7. For the latter case the secondary velocity values are a factor 50 smaller than for the former one.

The finite element calculations in a 3D–model of the carotid artery bifurcation were performed at a Reynolds number of 640 and a flow division ratio of about 50/50, simulating systolic fluid flow. High axial velocities were found near the divider wall of the carotid sinus, primarily due to flow branching but halfway the bulb also as a consequence of curvature effects. Due to the widening of the internal carotid artery and its large cross–sectional area, as compared to the main branch, a large region with negative axial velocities was found at the entrance of and halfway the carotid sinus. The shape of this region, the formation of an axial velocity plateau at the end of the bulb and the appearance of C–shaped curvatures of the axial isovelocity lines, are highly determined by secondary flow. At the entrance the secondary velocities were directed towards the flow divider, whereas halfway the carotid sinus a Dean type vortex was observed, as a consequence of curvature effects. At the end of the bulb inward directed secondary velocities occurred due to the tapering geometry. Qualitative and quantitative comparison of the velocity calculations with laser Doppler velocity measurements revealed good agreement. The minor differences are primarily due to measuring problems near the flow divider and the finite accuracy of the laser Doppler equipment.

From a parameter study it can be concluded that changes in the flow rate through the internal carotid artery by 20% hardly influence axial and secondary flow. The observed shifts of the axial isovelocity lines are caused by the larger flow rate through the internal carotid artery. A smaller bifurcation angle seems to affect only axial and secondary flow in the upstream region of the carotid sinus because the main stream velocities at the entrance of the bulb are still directed parallel to the axis of the main branch. For a smaller Reynolds number the largest differences occurred in the downstream region of the carotid sinus, where the secondary flow field, resulting from centrifugal forces, is probably less developed.

Qualitative comparison of the flow phenomena occurring in a 90–degree curved tube under steady flow conditions with those occurring in the carotid sinus revealed remarkable similarities. For both geometries a shift of the maximum of axial velocity towards the outer wall (divider wall), and the formation of C–shaped axial velocity contours and axial velocity plateaus in the downstream regions near the inner wall (non–divider wall) were observed. Secondary flow halfway the carotid sinus showed a Dean type vortex due to curvature effects. Secondary flow at the entrance of the carotid sinus, however, was mainly directed towards the flow divider, whereas secondary flow at the end of the bulb was highly influenced by the local geometry. The 'tail'–formation in the secondary flow field, as observed in the downstream regions of the curved tube, was absent in the carotid sinus, probably because the length over which curvature effects are important is small. Besides, large regions with axial flow reversal were observed opposite to the flow divider, as a consequence of the divergence of the carotid sinus at its inlet side and the larger cross–sectional area of both daughter branches, as compared to the cross–sectional area of the main branch. In the steady flow case regions with negative axial velocities were absent in the 90–degree curved tube.

With the axial and secondary flow fields, presented by axial isovelocity lines and secondary velocity vectors, a good impression can be obtained about the total flow field occurring in both geometries. Detailed analysis, however, may be difficult due to the large amount of data. Besides, in this way detailed comparison of axial and secondary flow for the various flow situations is hard to perform. Quantities, like the first moment of axial flow and the axial vorticities of secondary flow, seem to be more appropriate for this purpose. With these quantities, however, detailed information about axial and secondary flow, like the C–shaped curvatures of the axial velocity contours or the 'tail'–formation in the secondary flow field, is lost. Therefore, quantities are needed which are more appropriate to describe such features.

From the present study it is concluded that the finite element method can be used for detailed analysis of fluid flow in complex three–dimensional geometries.

With regard to blood flow in the carotid artery bifurcation, in the near future velocity calculations will be performed of unsteady flow in this bifurcation. A study of the influence of physiological and geometrical parameters on both axial and secondary flow in the carotid sinus, may then supply important information about methods used to diagnose atherosclerotic lesions at an early stage of the disease. Especially, when a detailed analysis of the flow field around small atherosclerotic lesions is performed. Incorporation of non–Newtonian behavior of blood and flexibility of the arterial wall in the numerical model will complete such an analysis. Besides, calculation of the shear stress as function of time and position in the carotid sinus, may supply valuable information with regard to the process of atherogenesis.

Appendices

Appendix A: Stability of the Adams–Bashforth integration scheme

Consider a linear set of ordinary differential equations resulting from the discretization of a parabolic differential equation, together with initial conditions:

$$\begin{aligned} \dot{\underset{\sim}{u}} &= \underline{A}\underset{\sim}{u} + \underset{\sim}{f} \\ \underset{\sim}{u}(t_0) &= \underset{\sim}{u}_0 \end{aligned} \tag{A.1}$$

If $\underline{A}$ has only real coefficients independent of time, resulting from a linear elliptic differential operator, and if $\underline{A}$ is non–defect, i.e. the number of independent eigenvectors is equal to the order of $\underline{A}$, then:

$$\underline{AB} = \underline{B\Lambda} \tag{A.2}$$

with $\underline{B}$ containing the eigenvectors of $\underline{A}$ and $\underline{\Lambda}$ a diagonal matrix containing the eigenvalues of $\underline{A}$. If $\underset{\sim}{u}$ is a solution of eq. A.1 with $\underset{\sim}{u}(t_0)=\underset{\sim}{u}_0$, if $\underset{\sim}{\xi}$ is also a solution of eq. A.1 with $\underset{\sim}{\xi}(t_0)=\underset{\sim}{u}_0+\underset{\sim}{\epsilon}_0$, $\underset{\sim}{\epsilon}_0$ being a small perturbation of $\underset{\sim}{u}_0$, and if $\underset{\sim}{\epsilon}$ is defined as $\underset{\sim}{\epsilon}=\underset{\sim}{\xi}-\underset{\sim}{u}$, then it is easily verified that $\dot{\underset{\sim}{\epsilon}}=\underline{A}\underset{\sim}{\epsilon}$ with $\underset{\sim}{\epsilon}(t_0)=\underset{\sim}{\epsilon}_0$. Defining $\underset{\sim}{\eta}=\underline{B}^{-1}\underset{\sim}{\epsilon}$ leads to:

$$\begin{aligned} \dot{\underset{\sim}{\eta}} &= \underline{\Lambda}\,\underset{\sim}{\eta} \\ \underset{\sim}{\eta}(t_0) &= \underline{B}^{-1}\underset{\sim}{\epsilon}_0 \equiv \underset{\sim}{\eta}_0 \end{aligned} \tag{A.3}$$

This is an uncoupled set of differential equations for $\underset{\sim}{\eta}$, which is directly related to the error column $\underset{\sim}{\epsilon}$. For a numerical stability analysis, error propagation defined by this equation and the numerical time integration scheme is considered. For the θ–method this leads to:

$$\begin{aligned} \dot{\eta}_i^{n+1} &= \lambda_i \eta_i^{n+1} \\ (\eta_i^{n+1} - \eta_i^n)/\Delta t &= \theta \dot{\eta}_i^{n+1} + (1-\theta)\dot{\eta}_i^n \end{aligned} \tag{A.4}$$

which can be presented in short form as:

$$\underset{\sim}{\chi}^{n+1} = \underline{C}^{-1}\underline{D}\,\underset{\sim}{\chi}^n \equiv G\,\underset{\sim}{\chi}^n \tag{A.5}$$

with:

$$\underset{\sim}{\chi}_n^T = [\dot{\eta}_i^n \quad \eta_i^n]; \quad \underline{C} = \begin{bmatrix} -\theta\Delta t & 1 \\ 1 & -\lambda_i \end{bmatrix}; \quad \underline{D} = \begin{bmatrix} (1-\theta)\Delta t & 1 \\ 0 & 0 \end{bmatrix}$$

$\underline{G}$ is the so–called amplification matrix which is suitable for a stability analysis as pointed out in the main text (sect. 3.5). The same analysis can be carried out for the Adams–Bashforth integration scheme. For this scheme $\underset{\sim}{\chi}_n$, $\underline{C}$ and $\underline{D}$ can be defined as:

$$\underset{\sim}{\chi}_n^T = [\dot{\eta}_i^n \quad \eta_i^n \quad \dot{\eta}_i^{n-1}]; \quad \underline{C} = \begin{bmatrix} 0 & 1 & -3\Delta t/2 \\ 1 & -\lambda_i & 0 \\ 0 & 0 & 1 \end{bmatrix}; \quad \underline{D} = \begin{bmatrix} 0 & -1 & \Delta t/2 \\ 0 & 0 & 0 \\ 1 & 0 & 0 \end{bmatrix}$$

Appendix B: Asymptotic and real speeds of supercomputers

The speed of super and minisupercomputers is achieved among others by parallel and vector processing techniques. With the parallel processing technique the maximum speed–up with regard to conventional computers is equal to the number of processors acting in parallel. The speed–up of a vector computer is achieved by segmentation of its functional units. In a functional unit one type of floating point operation (add, subtract, multiply, divide) is carried out, which can be divided into several basic operations. In figure B.1 a time diagram is presented of the processing of two vectors in the addition functional unit.

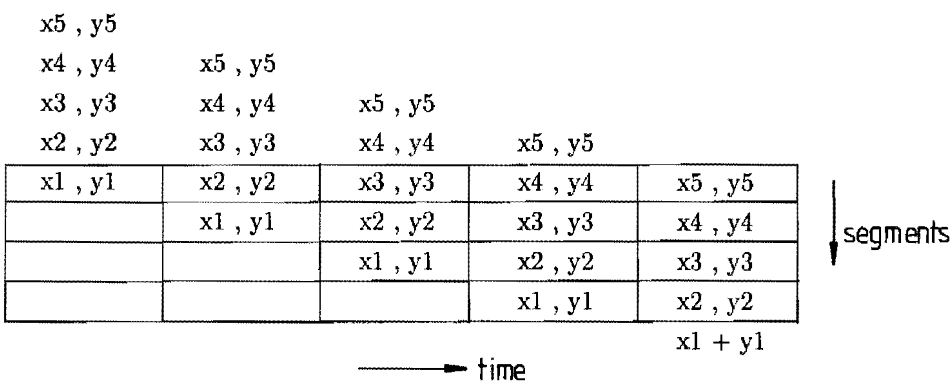

Figure B.1: Time diagram of vector processing on supercomputers in an addition functional unit consisting of 4 segments.

Every clock cycle a pair of operands is processed in each segment and pipelined to the next one. This results in one floating point operation per clock cycle. In scalar computers the processing of a pair of operands of two vectors is started if the processing of the previous pair is completely finished. The speed–up achieved with the vector processing technique ranges from 5 to 50 compared with scalar computers, depending on the number of basic operations of which a floating point operation consists. In many super and minisupercomputers high speeds are achieved by a combination of the above mentioned techniques and a smaller clocktime of the central processor. Table B.2 shows the asymptotic speeds of several computer systems used in this study. The minisupercomputer Alliant–fx/4 (TUE, 2 processors) and the supercomputer Cyber–205 (SARA, 2 vectorpipes) are used for the calculation of steady and unsteady entrance flow in a 90–degree curved tube, as described in chapter 5. For the calculation of steady flow in a 3D–model of the carotid artery bifurcation (chap. 6), the minisupercomputer Convex–c1xp (TUD) and the supercomputer Nec–sx2 (NLR) are used. Due to communication problems between the central memory and the disks, the results of the Nec–sx2 were not suitable for presentation. The Appolo–dsp90 (TUE) is a conventional minicomputer used in the study of v.d.Vosse et al. (1989), dealing with steady entrance flow in a 90–degree curved tube. Because the maximal number of floating point operations per second (Mxflops) is an asymptotic value, also the real number of floating point operations per second (Rlflops), as achieved for one of the problems solved in this study, is presented. The latter number is based on the LU–factorization of the matrix. If also the building of the system of equations is taken into account, this number must be multiplied by about 3/4 as for large problems the time needed to build the system of equations was about 1/3 of the time needed to solve the system of equations. The differences between the asymptotic and real number of floating point operations per second are caused by the start–up times of vector operations and because not all program statements can be vectorized. From Table 3C.2 it can be concluded that with regard to an Apollo–dsp90 the speed–up for (mini)supercomputers ranges from 100 to 1000.

	Apollo	Convex	Alliant	Cyber	Nec
Mxflops		20	23.5	200	1300
Rlflops	0.08	9	4.5	40	200

Table B.2: Maximal number (Mxflops) and real number (Rlflops) of floating point operations in millions per second, based on double precision floating point operations, for the systems used in the present study.

Appendix C: I/O–problems in combination with LU–factorization

Beside the CPU–time needed for a calculation, also the I/O–time needed can be an important aspect in the choice of a computer system. I/O–time is needed when not all data can be kept in the central memory and the virtual or backing storage devices are used. For virtual memory systems, which many systems are, the communication between the central memory and the virtual memory takes place by page faults. A page fault occurs when data, which are not present in the central memory, are needed for a calculation. Then, in general, a page, which is not used for the longest time, is stored on virtual memory and the page containing the data needed is stored in the central memory. Many page faults occur if the central memory is too small in relation to the system of equations to be solved, resulting in large I/O–times.

Within the package used to build and solve the system of equations, both the storage of the matrix elements and the LU–factorization are carried out row–column wise. In figure C.1 a square matrix $\underline{A}$ with bandwidth b is presented. The LU–factorization of the matrix is advanced up to row and column j. For L–factorization of row j, the elements of row j itself are needed as well as the elements indicated by the vertical solid lines. For U–factorization of column j, the elements indicated by the horizontal solid lines are needed as well as the elements of column j itself. Therefore, for LU–factorization of row and column j the elements indicated by the vertical and horizontal solid lines are strictly needed but, due to the way the matrix is stored, $N_b=0.5b^2$ elements will be stored in the central memory. The extra elements are indicated in figure C.1 by broken lines. If the total capacity of the central memory is equal to N_c, many page faults will occur if $N_c<N_b$. Then, for LU–factorization of each row and column at least (N_b-N_c) elements but in general N_b elements will be page faulted. For the system of equations solved in this study N_b is of $O(10^6)$ and the number of rows of $O(10^4)$. If for such a system of equations the inequality $N_c<N_b$ holds, enormous I/O–times will occur.

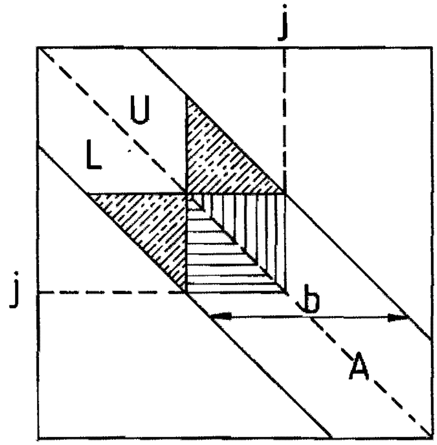

Figure C.1: LU–factorization of matrix $\underline{A}$.

References

– Altura B.T. and Altura B.M. (1975) Pentobarbital and contraction of vascular smooth muscle, American J. Physiology **229**, 1635–1640.

– Angell–James J.E. and Lumley J.S.P. (1974) The effects of carotid endarterectomy on the mechanical properties of the carotid sinus and carotid sinus nerve activity in atherosclerotic patients, British J. Surgery **61**, 805.

– Arndt J.O., Klauske J. and Mersch F. (1968) The diameter of the intact carotid artery in man and its change with pulse pressure, Pflugers Archiv **301**, 230–240.

– Balasubramanian K. (1979) An experimental investigation of steady flow at an arterial bifurcation, PhD–thesis, Georgia Institute of Technology, Atlanta.

– Berger S.A., Talbot L. and Yao L.S. (1983) Flow in curved pipes, Ann. Rev. Fluid Mech. 15, 461–512.

– Bertelsen A.F. (1975) An experimental investigation of low Reynolds number secondary streaming effects associated with an oscillating viscous flow in a curved pipe, J. Fluid Mech. **70**, 519–527.

– Bharadvaj B.K., Mabon R.F. and Giddens D.P. (1982) Steady flow in a model of the human carotid bifurcation, Part 1–Flow visualization, Part 2–Laser–Doppler anemometer measurements, J. Biomechanics **15**, 349–378.

– Bovendeerd P.H.M., Steenhoven A.A. van, Vosse F.N. van de and Vossers G. (1987) Steady entry flow in a curved pipe, J. Fluid Mech. **177**, 233–246.

– Brezzi F. (1974) On the existence, uniqueness and approximation of saddle point problems arising from Lagrangian multipliers, RAIRO Anal. Num. **R2**, 129–151.

– Brown P.M. and Johnston K.W. (1982) The difficulty of quantifying the severity of carotid stenosis, Surgery 92, 468–473.

- Canuto C., Hussaini M.Y., Quarteroni A. and Zang T.A. (1988) Spectral methods in fluid dynamics, Springer Verlag, New York.

- Caro C.G., Fitz–Gerald J.M. and Schroter R.C. (1971) Atheroma and arterial wall shear, Proc. Roy. Soc. London B. **177**, 109–159.

- Chandran K.B. and Yearwood T.L. (1981) Experimental study of physiological pulsatile flow in a curved tube, J. Fluid Mech. **111**, 59–85.

- Chandran K.B., Yearwood T.L. and Wieting D.W. (1979) An experimental study of pulsatile flow in a curved tube, J. Biomechanics **12**, 793–805.

- Chang L.J. and Tarbell J.M. (1988) A numerical study of flow in curved tubes simulating coronary arteries, J. Biomechanics 21, 927–937.

Corver J.A.W.M., Vosse F.N. van de, Steenhoven A.A. van and Reneman R.S. (1985) The influence of a small stenosis in the carotid bulb on adjacent axial velocity profiles: Biomechanics current interdisciplanary research, 239–244, Martinus Nijhoff Publ., Dordrecht.

- Crouzeix M. and Raviart P.A. (1973) Conforming and nonconforming finite element methods for solving the stationary Stokes equations, RAIRO Anal. Num. **R3**, 33–76.

- Cuthill E. and McKee J. (1969) Reducing the band width of sparse symmetric matrices, Proc. ACM Nat. Conf. Association of Computing Machinery, New York.

- Cuvelier C., Segal A. and Steenhoven A.A. van (1986) Finite element methods and Navier–Stokes equations, D. Reidel Publishing Comp., Dordrecht.

- Drain L.E. (1981) The laser Doppler technique, John Wiley & Sons, New York.

- Fernandez R.C., de Witt K.J. and Botwin M.R. (1976) Pulsatile flow through a bifurcation with applications to arterial disease, J. Biomechanics **9**, 575–580.

- Fortin M. (1981) Old and new finite elements for incompressible flows, Int. J. Num. Meth. Fluids **1**, 347–364.

- Fortin M. and Fortin A. (1985) Newer and newer elements for incompressible flow, Finite elements in fluids **6**, 171–187, John Wiley & Sons, New York.

- Fortin M. and Glowinski R. (1983) Resolution numerique de problemes aux limites par des methodes de Lagrangian augmente, Dunod, Paris.

- Fry D.L. (1969) Certain histological and chemical responses of the vascular interface to acutely induced mechanical stress in the aorta of the dog, Circulation Res. **24**, 93–108.

- Girault V. and Raviart P.A. (1979) Finite element approximation of the Navier Stokes equations, Springer Verlag, New York.

- Gow B.S. and Hadfield C.D. (1979) The elasticity of canine and human coronary arteries with reference to postmortem changes, Circulation Research **45**, 588–594.

- Greenfield J.C., Tindall G.T., Dillon M.L. and Mahaley M.S. (1964) Mechanics of the human common carotid artery in vivo, Circulation Research **15**, 240–246.

- Hamakiotes C.C. and Berger S.A. (1988) Fully developed pulsatile flow in a curved pipe, J. Fluid Mech. **195**, 23–55.

- Harrison M.J.G. and Marshall J. (1983) Does the geometry of the carotid bifurcation affect its predisposition to atheroma: letter to the editor, Stroke **14**, 117.

- Hendriks F. and Aviram A. (1981) Use of zinc–iodide solutions in flow research, Rev. Sc. Instrum. **53**, 75–78.

- Keller H.M., Meier W.E., Anliker M. and Kumpe D.A. (1976) Noninvasive measurement of velocity profiles and blood flow in the common carotid artery by pulsed Doppler ultrasound, Stroke **7**, 370–377.

- Ku D.N. and Giddens D.P. (1983) Pulsatile flow in a model carotid bifurcation, Arteriosclerosis **3**, 31–39.

- Ku D.N., Giddens D.P., Phillips D.J. and Strandness D.E. (1985) Hemodynamics of the normal human carotid bifurcation: in vitro and in vivo studies, Ultrasound in Med. & Biol. **11**, 13–26.

- Ku D.N., Giddens D.P., Zarins C.K. and Glagov S. (1985) Pulsatile flow and atherosclerosis in the human carotid bifurcation, Atherosclerosis **5**, 293–302.

- Ladyzhenskaya O.A. (1969) The mathematical theory of viscous incompressible flow, Gordon and Breach, New York.

- Lawson C.L., Hanson R.J., Kincaid D.R. and Krogh F.T. (1979) Basic linear algebra subprograms for Fortran usage, ACM Transactions on mathematical software **5**, 308–323.

- Liepsch D. and Moravec S. (1984) Pulsatile flow of non–Newtonian fluid in distensible models of human arteries, Biorheology **21**, 571–586.

- Lin J.Y. and Tarbell J.M. (1980) An experimental and numerical study of periodic flow in a curved tube, J. Fluid Mech. **100**, 623–638.

- Lutz R.J., Cannon J.N., Bischoff K.B., Dedrick R.L., Stiles R.K. and Fry D.L. (1977) Wall shear stress distribution in a model canine artery during steady flow, Circulation Res. **41**, 391–399.

- Lyne W.H. (1970) Unsteady viscous flow in a curved pipe, J. Fluid Mech. **45**, 13–31.

- Mani R.L. and Eisenberg R.L. (1978) Complications of catheter cerebral arteriography, Am. J. Roentgenol. **131**, 867–869.

– Merode T. van, Hick P.J.J., Hoeks A.P.G. and Reneman R.S. (1988) The diagnosis of minor to moderate atherosclerotic lesions in the carotid artery bifurcation by means of spectral broadening combined with the direct detection of flow disturbances using a multi–gate pulsed Doppler system, Ultrasound in Med. & Biol. **14**, 459–464.

– Mitchell A.R. and Griffiths D.F. (1980) The finite difference method in partial differential equations, John Wiley & Sons, New York.

– Motomiya M. and Karino T. (1984) Flow patterns in the human carotid artery bifurcation, Stroke **15**, 50–56.

– Mullin T. and Greated C.A. (1980) Oscillatory flow in curved pipes, Part 1–The developing–flow case, Part 2–The fully developed case, J. Fluid Mech. **98**, 383–416.

– Munson B.R. (1975) Experimental results for oscillating flow in a curved pipe, The Physics of Fluids **18**, 1607–1609.

– Olson D.E. (1971) Fluid mechanics relevant to respiration: flow within curved or elliptical tubes and bifurcating systems, PhD–thesis, University of London.

– Olson R.M. (1974) Human carotid artery wall thickness, diameter, and blood flow by a noninvasive technique, J. Applied Physiology **37**, 955–960.

– Olson D.E. and Snyder B. (1985) The upstream scale of flow development in curved circular pipes, J. Fluid Mech. **150**, 139–158.

– Pelissier M. (1975) Resolution numérique de quelques problèmes raides en mecanique des milieux faiblement compressibles, Estratto da Calcolo **12**, 275–314.

– Perktold K., Florian H. and Hilbert D. (1987) Analysis of pulsatile blood flow: a carotid siphon model, J. Biomed. Eng. **9**, 46–53.

– Peterson R.E., Livingston K.E. and Escobar A. (1960) Development and distribution of gross atherosclerotic lesions at cervical carotid bifurcation, Neurology **10**, 955–959.

– Peyret R. and Taylor T.D. (1982) Computational methods for fluid flow, Springer Verlag, New York.

– Reneman R.S., Merode T. van, Hick P. and Hoeks A.P.G. (1985) Flow velocity patterns in and distensibility of the carotid artery bulb in subjects of various ages, Circulation **71**, 500–509.

– Reneman R.S., Merode T. van, Hick P. and Hoeks A.P.G. (1986) Cardiovascular applications of multi–gate pulsed Doppler systems, Ultrasound in Med. & Biol. **12**, 357–370.

– Rindt C.C.M., Vosse F.N. van de, Steenhoven A.A. van, Janssen J.D. and Reneman R.S. (1987) A numerical and experimental analysis of the flow field in a two–dimensional model of the human carotid artery bifurcation, J. Biomechanics **20**, 499–509.

– Rindt C.C.M., Steenhoven A.A.v. and Reneman R.S. (1988) An experimental analysis of the flow field in a three–dimensional model of the human carotid artery bifurcation, J. Biomechanics **21**, 985–991.

– Roache P.J. (1972) Computational fluid dynamics, Hermosa publishers, Albuquerque.

– Schlichting H. (1979) Boundary layer theory, 7th ed, McGraw–Hill, New York

– Segal A. (1984) Sepran user manual and programmers guide, Ingenieurs buro Sepra, Leidschendam.

– Segal A. (1986) Test problem for the ($Q_2^{(27)}$–P_1) element, Personal communication.

- Singh M.P., Sinha P.C. and Aggarwal M. (1978) Flow in the entrance of the aorta, J. Fluid Mech. **87**, 97–120.

- Sloan S.W. (1986) An algorithm for profile and wavefront reduction of sparse matrices, Int. J. Num. Meth. Engng. **23**, 239–251.

- Smith F.T. (1975) Pulsatile flow in curved pipes, J. Fluid Mech. **71**, 15–42.

- Spencer M.P. and Reid J.M. (1979) Quantitation of carotid stenosis with continuous–wave (C–W) Doppler ultrasound, Stroke **10**, 326–330.

- Talbot L. and Gong K.O. (1983) Pulsatile entrance flow in a curved pipe, J. Fluid Mech. **127**, 1–25.

- Taylor C. and Hood P. (1973) A numerical solution of the Navier–Stokes equations using the finite element technique, Comput. Fluids 1, 73–100.

- Temam R. (1977) Navier–Stokes equations, Theory and numerical analysis, 2nd ed, North Holland, Amsterdam.

- Vosse F.N. van de, Vial F.H., Steenhoven A.A. van, Segal A. and Janssen J.D. (1985) A finite element and experimental analysis of steady and pulsating flow over a two–dimensional step: Numerical methods in laminar and turbulent flow, 515–526, Pineridge Press, Swansea.

- Vosse F.N. van de, Segal A., Steenhoven A.A. van and Janssen J.D. (1986) A finite element approximation of the unsteady 2D–Navier–Stokes equations, Int. J. Num. Meth. Fluids **6**, 427–443.

  Vosse F.N. van de (1987) Numerical analysis of carotid artery flow, PhD–thesis, Eindhoven University of Technology, The Netherlands.

- Vosse F.N. van de, Steenhoven A.A. van, Segal A. and Janssen J.D. (1989) A finite element analysis of the steady laminar entrance flow in a 90^{o} curved tube, Int. J. Num. Meth. Fluids **9**, 275–287.

- Wille S.O. (1984) Numerical simulations of steady flow inside a three dimensional aortic bifurcation model, J. Biomed. Engng. **6**, 49–55.

- Zalosh R.G. and Nelson W.G. (1973) Pulsating flow in a curved tube, J. Fluid Mech. **59**, 693–705.

- Zarins C.K., Giddens D.P., Bharadvaj B.K., Sottiurai V.S., Mabon R.F. and Glagov S. (1983) Carotid bifurcation atherosclerosis: Quantitative correlation of plaque localization with flow velocity profiles and wall shear stress, Circulation Res. **53**, 502–514.

- Zbornikova V. and Lassvik C. (1986) Duplex scanning in presumably normal persons of different ages, Ultrasound in Med. & Biol. **12**, 371–378.

Samenvatting

Voor vroegtijdige detectie van atherosclerose in de halsslagadervertakking aan de hand van stromingsverstoringen rondom kleine vernauwingen, is inzicht in het totale stromingsveld onontbeerlijk. Naast experimenteel onderzoek, kunnen numerieke simulaties van de stroming een belangrijke bijdrage leveren aan dit inzicht.

In deze studie wordt gebruik gemaakt van geometriegegevens over de halsslagadervertakking zoals beschreven in de literatuur. Daarnaast heeft ook een beknopt onderzoek plaatsgevonden naar de geometrie van deze vertakking aan de hand van 7 opgespoten modellen. Hieruit blijkt dat grote interindividuele verschillen in deze geometrie optreden, die onderzoek naar de invloed van deze geometrievariaties op de optredende stromingsfenomenen noodzakelijk maken. Voor een numerieke simulatie van de bloedstroming in de halsslagadervertakking is gebruik gemaakt van Galerkin's eindige elementen methode formulering, waarbij bloed als Newtons en incompressibel en de vaatwand als star wordt verondersteld. Vanwege het grote aantal vergelijkingen dat behoort bij een drie–dimensionale analyse, is gebruik gemaakt van super– en minisupercomputers, die een factor 10 tot 1000 sneller kunnen zijn als de conventionele systemen. Om de benodigde rekentijden nog verder te reduceren is een meshgenerator ontwikkeld, waarmee verdeling van de halsslagadervertakking in een relatief klein aantal elementen mogelijk is, en is gebruik gemaakt van speciale hernummeringsprocedures. Voor experimentele validatie van de numerieke resultaten zijn laser–Doppler metingen uitgevoerd waarmee contactloos vloeistofsnelheden gemeten kunnen worden.

Vanwege zijn relatief eenvoudige geometrie en omdat gebleken is dat krommingseffecten een grote invloed hebben op de stromingsfenomenen in de halsslagadervertakking, is eerst de stationaire en instationaire stroming in een 90–graden bocht geanalyseerd. Hieruit blijkt dat het axiale snelheidsveld zeer sterk wordt bepaald door het secundaire snelheidsveld, dat op zijn beurt weer wordt geinduceerd door centrifugaal krachten werkend op de vloeistof deeltjes. Naast deze gedetailleerde analyse is ook de invloed bestudeerd van de frequentie parameter, de golf vorm en de stationaire component op het axiale en secundaire snelheidsveld.

Uit een gedetailleerde analyse van de stationaire stroming in de halsslagadervertakking volgt dat krommingseffecten inderdaad van groot belang zijn. Daarnaast is echter ook de specifieke geometrie van de bulbus, met name de proximale verwijding en de distale vernauwing, van grote invloed op het totale stromingsveld. Een parameter studie naar de invloed van het Reynolds getal, de

flow verhouding en de bifurcatie hoek op de stroming, laat zien dat voor een stationaire stroming deze invloed relatief klein is.

Uit deze studie volgt dat de eindige elementen methode in combinatie met supercomputers gebruikt kan worden om analyses te verrichten van de stroming in complexe drie–dimensionale configuraties. Voor een completere modelvorming van de bloedstroming in de halsslagadervertakking zal het in rekening brengen van flexibele wanden en niet–Newtonse vloeistoffen in het numerieke model noodzakelijk zijn.

Levensbericht

8–4–1960	Geboren te Zevenbergschen–Hoek
1972–1978	Atheneum–B aan het Thomas More College te Oudenbosch
1978–1985	Studie Werktuigbouwkunde aan de Technische Universiteit Eindhoven
1985–1989	Wetenschappelijk assistent aan de Technische Universiteit te Eindhoven, afdeling Werktuigbouwkunde

Stellingen

behorende bij het proefschrift

Analysis
of the three–dimensional flow field
in the carotid artery bifurcation

1. Bij de ontwikkeling van non–invasieve detectiemethoden van aderverkalking in de menselijke halsslagadervertakking, moet terdege rekening worden gehouden met de grote interindividuele variabiliteit in de geometrie van deze vertakking.
   – Dit proefschrift, hoofdstuk 2.

2. De eindige–elementenmethode is zeer goed bruikbaar voor het simuleren van bloedstromingen in complexe drie–dimensionale geometrieën onder fysiologische stromingscondities, mits gebruik wordt gemaakt van efficiënte oplosstrategieën of (mini)supercomputers.
   – **Perktold et al.** (1987) *Analysis of pulsatile blood flow: a carotid siphon model*, J. Biomed. Eng. **9**, 46–53.
   – Dit proefschrift.

3. De huidige commerciële meshgeneratoren zijn niet geschikt een complexe geometrie, zoals de halsslagadervertakking, in een relatief klein aantal kubische elementen op te delen.

4. Beter één minisupercomputer in de hand dan tien supercomputers in de lucht.

5. Het secundaire snelheidsveld in een 90^o–bocht wordt, voor stromingen met een stationaire component van dezelfde orde van grootte als de instationaire component en voor hoge waarden van de Womersley parameter, in hoge mate bepaald door de stationaire component.
   – **Smith** (1975) *Pulsatile flow in curved pipes*, J. Fluid Mech. **71**, 15–42.
   – Dit proefschrift, hoofdstuk 5.

6. Voor vloeistofstromingen in een 90^{0}–bocht onder fysiologische stromingscondities is de invloed van de diastolische fase op de stromingsfenomenen in de systolische fase gering.
   –Dit proefschrift, hoofdstuk 5.

7. Het definieren van geschikte parameters, die op een adequate wijze het axiale en secundaire snelheidsveld in de halsslagadervertakking kunnen beschrijven, is noodzakelijk bij verder onderzoek naar de invloed van vaatvernauwingen op het totale stromingsveld.

8. Naast het bochteffect heeft ook de specifieke vorm van de bulbus een grote invloed op het axiale en secundaire snelheidsveld in de halsslagadervertakking.
   - **Olson** (1971) *Fluid mechanics relevant to respiration: flow within curved or elliptical tubes and bifurcating systems*, PhD–thesis, University of London.
   - Dit proefschrift, hoofdstuk 6.

9. De vloeistof–structuur interactiemodellen zoals die ontwikkeld zijn door ondermeer Belytschko, zijn niet geschikt voor het beschrijven van interactieproblemen waarin de structuur een verwaarloosbare massa heeft ten opzichte van de vloeistof.
   - **Belytschko** (1980) *Fluid–structure interaction*, Comput. & Struct. **12**, 459–469.

10. De mogelijkheid om (top)atleten ook tijdens trainingen te kunnen onderwerpen aan een controle op het gebruik van stimulerende middelen, zal de geloofwaardigheid in (top)prestaties ten goede komen.

11. Gebonden hulp aan de derde wereld landen is strijdig met de gedachte deze landen onafhankelijker te maken van de eerste wereld.

12. Zeehonden, maar ook walvissen, leiden een hondeleven.

Eindhoven, april 1989 Camilo Rindt